# Inclusive semi–leptonic $B$-meson decay in the $QCD$–improved parton model

**Dissertation**
**zur Erlangung des Doktorgrades**
**des Fachbereichs Physik**
**der Universität Hamburg**

**vorgelegt von**
**Hyejung Kim**
**aus Kangrung**

**Hamburg**
**2002**

| | |
|---|---|
| Gutachter der Dissertation: | Prof. Dr. B. A. Kniehl<br>Prof. Dr. G. Kramer |
| Gutachter der Disputation: | Prof. Dr. B. A. Kniehl<br>Prof. Dr. J. Bartels |
| Datum der Disputation: | 9. Dezember 2002 |
| Vorsitzender des Prüfungsausschusses: | Prof. Dr. G. Mack |
| Vorsitzender des Promotionsausschusses: | Prof. Dr. G. Huber |
| Dekan des Fachbereichs Physik: | Prof. Dr. F.-W. Büßer |

# Abstract

Semi–leptonic $B$-decay plays an important role in determining the $CKM$ matrix element $|V_{ub}|$. Whereas the leptonic tensor is completely known, the hadronic tensor of semi–leptonic $B$-decay is not completely calculable due to non–perturbative $QCD$ effects.

In the Light–Cone limit, the hadronic tensor can be expressed with a single distribution function $f(x)$. The interpretation of the distribution function is to parameterize the probability of finding a $b$-quark with momentum fraction $x$ inside the $B$-meson, which is similar to the parton model. We apply the parton model to $B$-meson decay and analyze various subsequent decay spectra.

Apart from the naive parton model, we consider further $QCD$ interactions of the $b$-quark, before it decays into a light–quark and leptons. The distribution function is modified by perturbative $QCD$ corrections. After factorization, the distribution function obtains the dependence of the leptonic invariant mass $W^2$. We apply Altarelli–Parisi type evolution of the distribution function.

$QCD$ corrections to $b \to u\ell\nu_\ell$ at order $\alpha_s$ are calculated using the dimensional regularization scheme. The electron energy spectrum, the leptonic invariant mass spectrum, the hadronic energy spectrum, and the hadronic invariant mass spectrum from $B$-meson decay and $b$-quark decay are studied and compared. We investigate $B$-meson decay using the naive parton model and the parton model with an evolved distribution function.

# Zusammenfassung

Der semi–leptonische $B$-Meson Zerfall spielt eine wichtige Rolle, um das *CKM* Matrixelement $|V_{ub}|$ zubestimmen. Während der leptonische Tensor vollständig bekannt ist, ist eine Berechnung des hadronischen Tensor des semi–leptonischen $B$-Meson Zerfalls wegen der nicht–perturbativen *QCD* Effekte nicht möglich.

Im Light–Cone Nährung kann der hadronische Tensor mit einer einzelnen Verteilungsfunktion $f(x)$ ausgedrückt werden. Die Bedeutung der Verteilungsfunktion ist die Wahrscheinlichkeit, dass das $b$-Quark den Implusanteil $x$ innerhalb des $B$-Mesons besitzt. Wir wenden das Parton–Modell auf den $B$-Meson Zerfall an und analysieren verschiedene Spektren vom $B$-Meson Zerfall.

Über das naive Parton–Modell hinaus betrachten wir weitere *QCD*–Wechselwirkung des $b$-Quark innerhalb des $B$-Mesons, die vor dem Zerfall des $b$-Quarks in eine leichtes Quark und Leptonen stattfinden. Die Verteilungsfunktion wird durch perturbativen *QCD* Korrekturen geändert. Nach Faktorisierung erreicht die Verteilungsfunktion die Abhängigkeit der leptonische invariante Masse $W^2$. Wir wenden die Altarelli–Parisi Gleichung für die Verteilungsfunktion an.

Die *QCD* Korrekturen für $b \to u\ell\nu_\ell$ der Ordnung $\alpha_s$ werden mit dem Dimensionalen Regularisierung berechnet. Das Elektronenergiespektrum, das leptonische invariante Massenspektrum, das hadronische Energiespektrum und das hadronische invariant Massenspektrum für den $b$-Quark Zerfall und den $B$-Meson Zerfall werden studiert und verglichen. Wir studieren den $B$-Meson Zerfall mit dem naiven Parton–Modell und dem Parton–Modell mit der entwickelten Verteilungsfunktion.

# Contents

**Abstract** **i**

**Zusammenfassung** **iii**

**1 Introduction** **1**

**2 Theoretical background and ···** **9**
2.1 Standard model and *CKM* matrix . . . . . 9
2.2 Semi–leptonic $B$-meson decays . . . . . 11
2.3 Light–Cone Expansion . . . . . 13
2.4 Experimental Research on $B$-meson decays . . . . . 17

**3 *QCD* Corrections using the Dimensional···** **21**
3.1 Kinematic Variables . . . . . 21
3.2 Born Approximation . . . . . 22
3.3 *QCD* Radiative Corrections . . . . . 23
3.3.1 Virtual Gluon Corrections . . . . . 25
3.3.2 Real Gluon Corrections . . . . . 30
3.3.3 Differential Decay Rate with $\alpha_s$ Corrections . . . . . 39

**4 Radiatively Corrected Spectra ···** **43**
4.1 Electron Energy Spectrum . . . . . 44
4.2 Leptonic Invariant Mass Spectrum . . . . . 46
4.3 Hadronic Energy Spectrum . . . . . 49
4.4 Hadronic Invariant Mass Spectrum . . . . . 54

**5 $B$-meson decay in the Parton model** **59**
5.1 Parton model and $B$-meson decay . . . . . 59
5.1.1 Parton model . . . . . 60
5.1.2 $B$-meson decay in view of the Parton model . . . . . 62
5.1.3 Distribution Function . . . . . 63
5.2 Spectra from $B$-meson decay . . . . . 69
5.2.1 Electron Energy Spectrum . . . . . 70
5.2.2 Leptonic Invariant Mass Spectrum . . . . . 74

5.2.3 Hadronic Energy Spectrum . . . . . 77
5.2.4 Hadronic Invariant Mass Spectrum . . . . . 81

**6 Evolution of the distribution function $f(x, W^2)$ 87**
6.1 Altarelli–Parisi Evolution Equation . . . . . 88
6.2 Factorization . . . . . 89
6.3 Spectra with Evolved Distribution Function . . . . . 92

**7 Conclusions 105**

**Appendix A Calculation of $\mathcal{I}_i$ 107**

**Appendix B Hyper Geometric Function 113**

**Appendix C Phase Space 115**

**Appendix D $\gamma_5$ in $n$–dimension: Breitenlohner–Maison rules 117**

**Appendix E Hadronic Tensor $h^j{}_i{}^{\mu\nu}$ 121**

**Appendix F +-description $[f(x)]_+$ 123**

**Bibliography 127**

**Acknowledgment 133**

# List of Figures


1.1 The Dalitz plot for $q^2$ and $M_X^2$. The cut on $M_X$ keeps a larger fraction of the events than the cut on $q^2$. . . . . 3

1.2 (a) The hadronic mass $m_{had}$ distribution for 1000 $fb^{-1}$ data found with CLEO III fast MC. (b) The $q^2$ distribution for 1000 $fb^{-1}$ data found with CLEO III fast MC. In both (a) and (b) the solid histograms are the $q^2$ or $m_{had}$ distribution of $b \to u\ell\bar{\nu}_\ell$ and the dashed histograms the $q^2$ or $m_{had}$ distribution of $b \to c\ell\bar{\nu}_\ell$. . . . . 4

2.1 Inclusive semi–leptonic $B$-meson decay. . . . . 12

2.2 $QCD$ interactions inside $B$-mesons. . . . . 17

2.3 End view of the *BABAR* detector. . . . . 19

2.4 Side view of the Belle detector. . . . . 20

3.1 Feynman diagram for the Born approximation. . . . . 23

3.2 The solid line shows the Born approximation of the electron energy spectrum, and the dotted line is the spectrum with radiative corrections at $\alpha_s = 0.22$. . . . . 24

3.3 Feynman diagrams for the virtual corrections. The first diagram is the vertex correction, and the last two are quark self–energies. . 26

3.4 Feynman diagram for the self–energy $\Sigma_M$ of a particle with mass $M$. 26

3.5 Feynman diagram for the one–loop vertex correction. $G_W \equiv -ig_w\frac{V_{ub}}{2\sqrt{2}}$ with the weak coupling constant $g_w$ and the $CKM$ matrix element $V_{ub}$ for the $b \to u$ transition. . . . . 28

3.6 Feynman diagrams for the real corrections. . . . . 30

4.1 (a) The radiatively corrected electron energy spectrum normalized with $\Gamma$. The dotted line shows the Born approximation of the spectrum normalized with $\Gamma_0$. The solid line displays the radiatively corrected spectrum at $\alpha_s = 0.22$, and the dashed line at $\alpha_s = 0.25$. (b) The electron energy spectrum normalized by $\Gamma_0$. The dotted line shows the Born approximation of the spectrum. The solid line displays the radiatively corrected spectrum at $\alpha_s = 0.22$. . . . . 45

4.2 The leptonic invariant mass spectrum with radiative corrections. The dotted line shows the Born approximation of the leptonic invariant mass spectrum. The solid line displays the radiatively corrected spectrum at $\alpha_s = 0.22$, and the dashed line at $\alpha_s = 0.25$. . 47

4.3 The radiatively corrected leptonic invariant mass spectrum at various $\alpha_s$ is compared with the Born approximation of the spectrum. (a) The dotted line shows the Born approximation of the leptonic invariant mass spectrum. The solid line displays the radiatively corrected spectrum at $\alpha_s = 0.51$, and the dashed line at $\alpha_s = 0.36$. (b) The dotted line shows the Born approximation of the leptonic invariant mass spectrum. The solid line displays the radiatively corrected spectrum at $\alpha_s = 0.32$, and the dashed line at $\alpha_s = 0.26$. 48

4.4 (a) The hadronic energy spectrum $d\Gamma/dE_H$ in units of $\Gamma$. The dotted line shows the Born approximation of the spectrum normalized with $\Gamma_0$. The solid line displays the radiatively corrected spectrum at $\alpha_s = 0.22$, and the dashed line at $\alpha_s = 0.25$. (b) The hadronic energy spectrum $d\Gamma/dE_H$ normalized with $\Gamma_0$. The dotted line shows the Born approximation of the spectrum. The solid line displays the radiatively corrected spectrum at $\alpha_s = 0.22$, and the dashed line at $\alpha_s = 0.25$. . . . . 51

4.5 (a) The hadronic energy spectra at $\bar{\Lambda} = 0$. The dotted line shows the Born approximation of the spectrum. The solid line displays the spectrum with the radiative corrections at $\alpha_s = 0.22$, and the dashed line at $\alpha_s = 0.25$. (b) The comparison between the spectra with $\bar{\Lambda} = 0.48\ GeV$ and those with $\bar{\Lambda} = 0$ is displayed. The dashed line is the Born approximation of the hadronic energy spectrum, and the dot–dashed line is the spectrum with the radiative corrections at $\alpha_s = 0.22$. For both of the dashed line and the dot–dashed line, $\bar{\Lambda} = 0$. The dotted line shows the Born approximation of the spectrum with $\bar{\Lambda} = 0.48\ GeV$, and the solid line is the spectrum with the radiative corrections at $\alpha_s = 0.22$ with $\bar{\Lambda} = 0.48\ GeV$. . . 53

4.6 (a) The squared hadronic invariant mass $S_H$ spectrum in units of $\Gamma$. The dotted line shows the Born approximation of the squared hadronic invariant mass spectrum. The solid line displays the spectrum with radiative corrections at $\alpha_s = 0.22$, and the dashed line at $\alpha_s = 0.25$. (b) The squared hadronic invariant mass $S_H$ spectrum normalized with $\Gamma_0$. The dotted line shows the Born approximation of the spectrum. The solid line displays the spectrum with the radiative corrections at $\alpha_s = 0.22$, and the dashed line at $\alpha_s = 0.25$. 57

4.7 (a) The hadronic invariant mass $M_H$ spectrum in units of $\Gamma$. The dotted line shows the spectrum in the Born approximation. The solid line displays the spectrum with the radiative corrections at $\alpha_s = 0.22$, and the dashed line at $\alpha_s = 0.25$. (b) The hadronic invariant mass $M_H$ spectrum normalized with $\Gamma_0$. The dotted line shows the spectrum in the Born approximation. The solid line displays the spectrum with radiative corrections at $\alpha_s = 0.22$, and the dashed line at $\alpha_s = 0.25$. . . . . 58

5.1 Lepton–nucleon scattering: Deep Inelastic Scatterings. . . . . 61

5.2 $B$-meson decay in the parton model. . . . . 63

5.3 The electron energy spectrum from $B$-meson decay is compared with that from $b$-quark decay. The $b$-quark mass is assumed to be $m_b = 4.80\ GeV$. . . . . 71

5.4 (a) The dotted line is the Born approximation of the spectrum with $a = 0.00417$ and $b = 0.917$, and the solid line the spectrum with radiative corrections at $\alpha_s = 0.22$ with $a = 0.00417$ and $b = 0.917$. The dashed line is the Born approximation of the spectrum with $a = 0.00566$ and $b = 0.889$, and the dot–dashed line the spectrum with radiative corrections at $\alpha_s = 0.22$ with $a = 0.00566$ and $b = 0.889$. (b) The dotted line is the Born approximation of the spectrum with $a = 0.00417$ and $b = 0.917$, and the solid line the spectrum with radiative corrections at $\alpha_s = 0.25$ with $a = 0.00417$ and $b = 0.917$. The dashed line is the Born approximation of the spectrum with $a = 0.00566$ and $b = 0.889$, and the dot–dashed line the spectrum with radiative corrections at $\alpha_s = 0.25$ with $a = 0.00566$ and $b = 0.889$. . . . . 72

5.5 (a) The Born approximation of the electron energy spectrum from $B$-meson decay with various $a$ and $b$. (b) The electron energy spectra from $B$-meson decay with the radiative corrections at $\alpha_s = 0.22$. For both (a) and (b), the solid line is with $a = 0.00417$ and $b = 0.917$, the dotted line with $a = 0.00566$ and $b = 0.889$, and the dashed line with $a = 0.00298$ and $b = 0.946$. . . . . 73

5.6 The $W^2$ spectrum from $B$-meson decay is compared with that from $b$-quark decay. In both (a) and (b), the dotted line is the $W^2$ spectrum from $b$-quark decay, and the solid line the spectrum from $B$-meson decay. The $b$-quark mass is assumed to be $m_b = 4.80\ GeV$. (a) The Born approximation of the $W^2$ spectrum from $b$-quark decay and from $B$-meson decay. (b) The $W^2$ spectrum with the radiative corrections at $\alpha_s = 0.22$ from $b$-quark decay and $B$-meson decay. . . . . 75

5.7 The dotted line: $m_b = 4.65\ GeV$; the solid line: $m_b = 4.80\ GeV$; the dashed line: $m_b = 4.95\ GeV$. (a) The Born approximation of the $W^2$ spectrum at various $a$ and $b$. (b) The $W^2$ spectrum with radiative corrections at $\alpha_s = 0.22$. . . . . 76

5.8 The hadronic energy spectrum from $B$-meson decay compared with that from $b$-quark decay at $m_b = 4.80\ GeV$. The solid line shows the spectrum from $B$-meson decay, and the dotted line from $b$-quark decay. (a) The Born approximation of the hadronic energy spectrum. (b) The hadronic energy spectrum with radiative corrections at $\alpha_s = 0.22$. . . . . 79

5.9 The hadronic energy spectrum from $B$-meson decay with various $a$ and $b$; the dotted line: $a = 0.00566$, $b = 0.889$; the solid line: $a = 0.00417$, $b = 0.917$; the dashed line: $a = 0.00298$, $b = 0.946$. (a) The Born approximation of the hadronic energy spectrum from $B$-meson decay. (b) The hadronic energy spectrum from $B$-meson decay with radiative corrections at $\alpha_s = 0.22$. . . . . 80

5.10 (a) The Born approximation of the squared hadronic invariant mass spectrum of $B$-meson decay is compared with that of $b$-quark decay. The solid line shows the spectrum of $B$-meson decay, and the dotted line of $b$-quark decay. (b) The spectrum with radiative corrections at $\alpha_s = 0.22$ are displayed. The solid line is the spectrum from $B$-meson decay, and the dotted line from $b$-quark decay. . . . . 82

5.11 For both (a) and (b); the dotted line: $m_b = 4.65\ GeV$; the solid line: $m_b = 4.80\ GeV$; the dashed line: $m_b = 4.95\ GeV$. (a) The Born approximation of the squared hadronic invariant mass spectrum from $B$-meson decay. (b) The squared hadronic invariant mass spectrum with radiative corrections at $\alpha_s = 0.22$ from $B$-meson decay. . . . . 83

5.12 (a) The Born approximation of the hadronic invariant mass spectrum from $B$-meson decay is compared with that from $b$-quark decay. The solid line shows the spectrum from $B$-meson decay, and the dotted line from $b$-quark decay. (b) The solid line is the hadronic invariant mass spectrum with radiative corrections at $\alpha_s = 0.22$ from $B$-meson decay, and the dotted line that from $b$-quark decay. . . . . 85

5.13 (a) The Born approximation of the hadronic invariant mass spectrum from $B$-meson decay with various $a$ and $b$ is displayed. (b) The hadronic invariant mass spectrum with radiative corrections at $\alpha_s = 0.22$. For both (a) and (b), the solid line is for $m_b = 4.80\ GeV$, the dashed line for $m_b = 4.65\ GeV$, and the dotted line for $m_b = 4.95\ GeV$. . . . . 86

6.1 (a) The change of $f_{jp}(x,\mu^2)$ with fixed $m_b^2 = 4.80^2\ GeV^2$. $f_{jp}(x,\mu^2)$ at $\mu^2 = 3.04\ GeV^2$, $13.04\ GeV^2$, $22.04\ GeV^2$. (b) The change of $f_{jp}(x,\mu^2)$ with $\mu^2 = x^2M_B^2 - W^2$. $f_{jp}(x,\mu^2)$ at $\mu^2 = x^2M_B^2 - 20\ GeV^2$, $x^2M_B^2 - 10\ GeV^2$, $x^2M_B^2 - 1\ GeV^2$. . . . . 97

6.2 (a) The change of $f_{ptr}(x,\mu^2)$ with fixed $m_b^2 = 4.80^2\ GeV^2$. $f_{ptr}(x,\mu^2)$ at $\mu^2 = 3.04\ GeV^2$, $13.04\ GeV^2$, $22.04\ GeV^2$. (b) The change of $f_{ptr}(x,\mu^2)$ with $\mu^2 = x^2M_B^2 - W^2$. $f_{ptr}(x,\mu^2)$ at $\mu^2 = x^2M_B^2 - 20\ GeV^2$, $x^2M_B^2 - 10\ GeV^2$, $x^2M_B^2 - 1\ GeV^2$. . . . . 98

6.3 (a) The change of $f_{jp}(x,\mu^2)$ at $x = 0.01, 0.3, 0.6, 0.9$. (b) The change of $f_{jp}(x,\mu^2)$ at $x = 0.1, 0.7, 0.9, 0.95$. For both (a) and (b), $m_b^2 = 4.80^2\ GeV^2$. . . . . 99

6.4 (a) $f_{ptr}(x,\mu^2)$ at $x = 0.01, 0.3, 0.6, 0.9$. (b) $f_{ptr}(x,\mu^2)$ at $x = 0.1, 0.7, 0.9, 0.95$. For both (a) and (b), $m_b^2 = 4.80^2\ GeV^2$. . . . . 100

6.5 (a) The solid line is the electron energy spectrum from $B$-meson decay using $f_{jp}(x,\mu^2)$. The dotted line is the Born approximation of the spectrum. The dashed line is the spectrum with radiative corrections at $\alpha_s = 0.22$ using the naive parton model with the distribution function $f_{jp}(x)$. (b) The electron energy spectrum with different distribution function models. The solid line is the spectrum using $f_{jp}(x,\mu^2)$, and the dotted line the spectrum using $f_{ptr}(x,\mu^2)$. . . . . 101

6.6 The electron energy spectrum with various evolution ranges. (a) The solid line is the electron energy spectrum, where evolution starts from $\mu^2 = x^2M_B^2 - 1\ GeV^2$, which corresponds to $W^2 = 1\ GeV^2$. The dashed line has evolution range from $\mu^2 = x^2M_B^2 - 5\ GeV^2$, the dotted line from $\mu^2 = x^2M_B^2 - 15\ GeV^2$, and the dot–dashed line from $\mu^2 = x^2M_B^2 - 20\ GeV^2$. $f_{jp}(x,\mu^2)$ is used for the distribution function. (b) The solid line is the electron energy spectrum, where evolution starts from $\mu^2 = x^2M_B^2 - 1\ GeV^2$. The dashed line has evolution range from $\mu^2 = x^2M_B^2 - 5\ GeV^2$, the dotted line from $\mu^2 = x^2M_B^2 - 15\ GeV^2$, and the dot–dashed line from $\mu^2 = x^2M_B^2 - 20\ GeV^2$. $f_{ptr}(x,\mu^2)$ is used for the distribution function. . . . . 102

6.7 (a) The solid line is the leptonic invariant mass spectrum $W^2$ from $B$-meson decay using $f_{jp}(x,\mu^2)$. The dotted line is the Born approximation of the spectrum. The dashed line is the spectrum with radiative corrections at $\alpha_s = 0.22$ using the naive parton model with the distribution function $f_{jp}(x)$. (b) The leptonic invariant mass spectrum with different distribution function models. The solid line is the spectrum using $f_{jp}(x,\mu^2)$, and the dotted line the spectrum using $f_{ptr}(x,\mu^2)$. . . . . 103

6.8 The leptonic invariant mass spectrum with various evolution ranges. (a) The solid line is the leptonic invariant mass spectrum, where evolution starts from $\mu^2 = x^2 M_B^2 - 1\ GeV^2$. The dashed line has evolution range from $\mu^2 = x^2 M_B^2 - 5\ GeV^2$, the dotted line from $\mu^2 = x^2 M_B^2 - 15\ GeV^2$, and the dot–dashed line from $\mu^2 = x^2 M_B^2 - 20\ GeV^2$. $f_{jp}(x, \mu^2)$ is used for the distribution function. (b) The solid line is the leptonic invariant mass spectrum, where evolution starts from $\mu^2 = x^2 M_B^2 - 1\ GeV^2$. The dashed line has evolution range from $\mu^2 = x^2 M_B^2 - 5\ GeV^2$, the dotted line from $\mu^2 = x^2 M_B^2 - 15\ GeV^2$, and the dot–dashed line from $\mu^2 = x^2 M_B^2 - 20\ GeV^2$. $f_{ptr}(x, \mu^2)$ is used for the distribution function. . . . . 104

# Chapter 1

# Introduction

The Cabibbo–Kobayashi–Maskawa matrix (*CKM*) is one of the fundamental parameters in the Standard Model. It explains quark mixing through the weak interaction and plays an important role in the investigation of *CP* violation in the Standard Model. Precise determination of the *CKM* matrix elements is therefore very important. Among the 9 *CKM* matrix elements, $V_{ub}$, which determines the length of one side of the unitarity triangle,presently has the largest uncertainty, so it is highly desirable to make a precise measurement of $V_{ub}$.

Inclusive semi–leptonic $B$-meson decays

$$B \longrightarrow X_{u,c} + \ell + \bar{\nu}_\ell \tag{1.1}$$

are the most important processes to determine the parameters $V_{ub}$ and $V_{cb}$. Semi–leptonic $B$-meson decay is expressed with a leptonic tensor and a hadronic tensor. The leptonic tensor is completely calculable, whereas there has not been a complete solution of the hadronic tensor, which incorporates non–perturbative *QCD* effects.

The ratio of $V_{ub}$ and $V_{cb}$ is known to be

$$\left|\frac{V_{ub}}{V_{cb}}\right| = 0.090 \pm 0.025\,. \tag{1.2}$$

As seen in Eq.(1.2) $b$-quark decays with $b \to u$ transition are suppressed compared to those with $b \to c$ transition, which makes it difficult to get enough events to measure $V_{ub}$ with high precision. Especially when one attempts to measure totally inclusive semi–leptonic $B$-decay rates, it is not easy to remove the $b \to c$ background, which is $\sim$ 100 times larger. Recently it has been argued that

the totally inclusive rate can be measured by using totally reconstructed $B$-decays [11].

The value of $|V_{ub}|$ is obtained from the branching fraction of inclusive $b \to X_u \ell \bar{\nu}_\ell$ decays, $Br(b \to X_u \ell \bar{\nu}_\ell)$ [25, 37]. Using the Heavy Quark Expansion (HQE) [38, 39] and inputs from the LEP Heavy Flavor Working Group [41], $|V_{ub}|$ is obtained as [42]

$$\begin{aligned} |V_{ub}| &= 0.00445 \times \left( \frac{Br(b \to X_u \ell \bar{\nu}_\ell)}{0.002} \frac{1.55\,\mathrm{ps}}{\tau_b} \right)^{\frac{1}{2}} \times \\ &\quad \left(1 \pm 0.010_{pert} \pm 0.030_{1/m_b^3} \pm 0.035_{m_b}\right), \end{aligned} \tag{1.3}$$

and the average lifetime $\tau_b$ of the $b$–hadron is $(1.564 \pm 0.014)$ ps from LEP experiments [40]. From this analysis we obtain $|V_{ub}|$ as

$$|V_{ub}| = \left(4.00 \pm 0.65\,(\mathrm{stat})\, ^{+0.67}_{-0.76}\,(\mathrm{sys}) \pm 0.19\,(\mathrm{HQE})\right) \times 10^{-3}. \tag{1.4}$$

The systematic error is from decay modeling, and the HQE error is the pure theoretical error from the Heavy Quark Expansion. The result in Eq.(1.4) shows good agreement with $|V_{ub}|$ from the CLEO exclusive measurement [44],

$$|V_{ub}|(\mathrm{CLEO}) = \left(3.3 \pm 0.8\,(\mathrm{total})\right) \times 10^{-3}. \tag{1.5}$$

Traditionally, one used the electron energy spectrum of $B$-meson decays to determine the branching ratio $Br(b \to X_u \ell \bar{\nu}_\ell)$ and $V_{ub}$. To remove the $b \to c$ background a cut $E_{e,\,cut} > (M_B^2 - m_D^2)/2M_B$ is imposed on the electron energy, but the cut on the electron energy does not allow enough events for analysis, leaving only fewer than 10 % of events. Moreover, non–perturbative $QCD$ effects are dominant in this end point region [35, 36, 70, 71, 72, 73, 74] and the Operator Product Expansion (OPE) is not valid. Instead of OPE one performs a twist expansion [12, 73, 74, 75, 76, 77]. In this case the Light–Cone distribution function determines the decay rate at leading order, and the sub–leading twist corrections are suppressed by higher orders of $1/m_b$ [14]. The distribution function, which incorporates non–peturbative $QCD$ is not calculable and should be determined experimentally. For example, the photon energy spectrum in $B \to X_s\,\gamma$ is used to determine the distribution function [15, 16, 17].

Apart from the electron energy spectrum, the lepton invariant mass spectrum [19, 20], the hadronic energy spectrum [21], and the hadronic invariant mass spectrum [22, 23, 26] can be used to determine $V_{ub}$. The hadronic invariant mass spectrum has the advantage that it keeps most of the $b \to u$ events. A study of the hadronic invariant mass spectrum with cuts on the lepton energy is presented in [26].

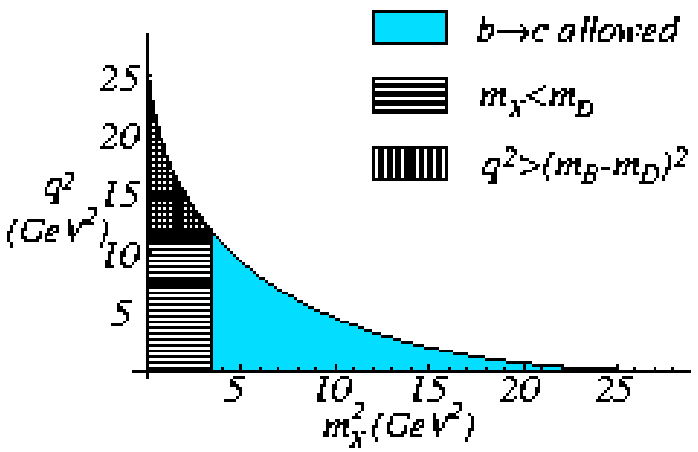


Figure 1.1: The Dalitz plot for $q^2$ and $M_X^2$. The cut on $M_X$ keeps a larger fraction of the events than the cut on $q^2$.

To remove the $b \to c$ background one needs to put cuts on the phase spaces of $q^2$ and $m_X^2$ [4, 23, 24, 25], and the number of events that can be used for analysis depends on the cuts. According to the calculation of the number of events after a cut on $q^2$ [19], the fraction of events selected by a cut $q^2_{cut}$ is between 10 % and 20 % and the uncertainties on $V_{ub}$ range from 15% for $q^2_{cut} = (M_B - M_D)^2 = 11.6\ GeV^2$ to 25 % for $q^2_{cut} = 14\ GeV^2$. Using the Dalitz plot in Figure 1.1 [20] one can determine cuts both on $q^2$ and $m_X^2$ that are related to each other. The advantage to use the Dalitz plot and cuts on both $q^2$ and $m_X^2$ is that it keeps a larger fraction of events than the cut on $q^2$ alone.

The distributions of $q^2$ and $m_{had} = \sqrt{m_X^2}$ are presented in Figure 1.2, which was produced using the Monte Carlo simulation with 1000 $fb^{-1}$ data found with CLEO III fast MC [11]. The cut on $q^2$ used for the analysis is $q^2_{cut} = 11.6\ GeV^2$ and events with $q^2 > 11.6\ GeV^2$ are selected for $b \to u$. For the analysis of the hadronic mass distribution $m_{had\,cut} = m_D$ was used as the cut on $m_{had}$. The $q^2$ distribution of $b \to u$ is dominant when $q^2 > 15\ GeV^2$ as is seen in Figure1.2(a). On the contrary, the hadronic mass $m_{had}$ distribution of $b \to u$ becomes dominant at small $m_{had}$, i.e. $m_{had} < \sim 1\ GeV$.

Another difficulty in determining $V_{ub}$ lies on the theoretical side. More specifically, the complication stems from the hadronic tensor, which is not totally calculable within perturbative *QCD*, since hadronization appears in the region where perturbative *QCD* is not valid.

In early times it was supposed that the $b$-quark inside a $B$-meson possessed most of the $B$-meson momentum, and $b$-quark decays were identified with $B$-meson decays. Under this condition the $b$-quark decay rate is

$$\Gamma \sim \frac{G_F^2 |V_{ub}|^2}{16\,\pi^3} m_b^5 \tag{1.6}$$

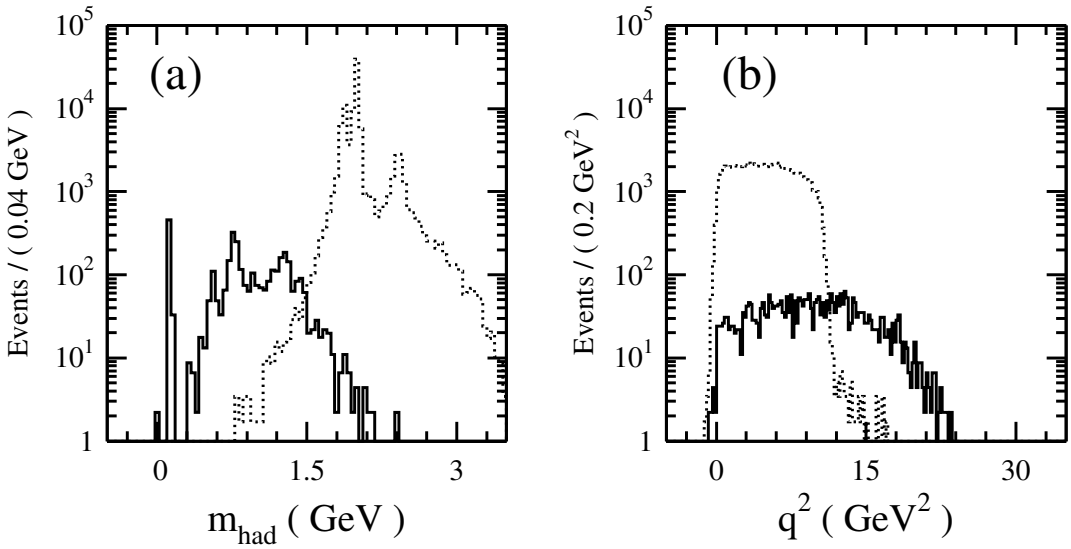


Figure 1.2: (a) The hadronic mass $m_{had}$ distribution for 1000 $fb^{-1}$ data found with CLEO III fast MC. (b) The $q^2$ distribution for 1000 $fb^{-1}$ data found with CLEO III fast MC. In both (a) and (b) the solid histograms are the $q^2$ or $m_{had}$ distribution of $b \to u\ell\bar{\nu}_\ell$ and the dashed histograms the $q^2$ or $m_{had}$ distribution of $b \to c\ell\bar{\nu}_\ell$.

which is found to be proportional to the $b$-quark mass to the fifth power. Unfortunately the $b$-quark mass $m_b$ is not measurable from experiments directly and has a great uncertainty. The masses of quarks are extracted from measurements using theory input [27] and displayed in Table 1.1. All physical states that are measurable experimentally are hadronic states such as mesons. The mass of $B$-meson is well measured and known to be $M_B = 5.28\ GeV$.

Two main approaches to calculation of the hadronic tensor are the Operator Product Expansion (OPE) and Lattice QCD ($LQCD$). The error in the inclusive $b \to u\ell\bar{\nu}_\ell$ rate predicted by OPE is within $5 - 10$ %. The phase space regions available experimentally are $m_X < m_D$ or the endpoint of the $q^2$ spectrum.

$LQCD$ yields useful results on exclusive semi–leptonic decays such as $D \to \pi\,\ell\,\bar{\nu}_\ell$ and $B \to \pi\,\ell\,\bar{\nu}_\ell$. $V_{cb}$ is determined directly by the $LQCD$ result of $f_D$ and measurements of $D^+ \to \mu^+\nu$ at a charm factory , for example CLEO–C [28]. The $LQCD$ result for $V_{ub}$ is tested by investigating the $q^2$ spectrum. If the spectrum shape from $LQCD$ agrees with the experimental results, the rate $\Gamma(B \to \pi\,\ell\,\bar{\nu}_\ell)$ is measured to extract $V_{ub}$, after the $q^2$ spectra of $B \to \pi\,\ell\,\bar{\nu}_\ell$ from $LQCD$ and $B$ factories are compared. The error in the $LQCD$ calculations leads to an uncertainty of $\delta\,V_{ub}^{stat.} \sim 1 - 2$ % [29].

The present work is composed of two main parts. One is the calculation of perturbative $QCD$ corrections to semi–leptonic $b$-quark decay, and the other is

| *Quark* | *Mass* ($MeV/c^2$) | *Quark* | *Mass* ($GeV/c^2$) |
|---|---|---|---|
| $u$ | $2.3 \pm 0.4$ | $c$ | $1.304 \pm 0.027$ |
| $d$ | $6.4 \pm 1.1$ | $b$ | $4.21 \pm 0.05$ |
| $s$ | $130 \pm 15$ | $t$ | 175 |

Table 1.1: The theoretically predicted quark masses.

the investigation of the non–perturbative *QCD* aspect of inclusive semi–leptonic $B$-meson decay.

We consider semi–leptonic $b$-quark decays with $b \to u$ transition

$$b \longrightarrow u + e + \bar{\nu}_e \,, \tag{1.7}$$

and determine the *QCD* corrections of $\mathcal{O}(\alpha_s)$. These corrections consist of real corrections, i.e. the process with an additional gluon $g$ in the final state

$$b \longrightarrow u + g + e + \bar{\nu}_e \,, \tag{1.8}$$

and the virtual corrections at one–loop level. *QCD* corrections in this work are done in the dimensional regularization scheme, the advantage of which is gauge invariance. Perturbative *QCD* corrections at next–to–leading order of $\alpha_s$ in the finite gluon mass regularization scheme are known and can be found in [4, 5, 6, 7, 8, 9]. In Section 3.3.3 we see that the results from the different regularization schemes are the same. *QCD* corrections at $\alpha_s^2$ order are found in [10].

Calculation of the non–perturbative *QCD* region is not as concrete as the case of the perturbative *QCD* corrections and is still controversial. We employ the parton model approach [30, 31, 33] in the Light–Cone limit.

Until now there have been many attempts to solve non–perturbative *QCD*, but no complete solution has yet been found. In the cases of mesons with heavy quarks, such as $B$-mesons, one can exploit the fact that the mass difference between the light quarks ($u$, $d$ and $s$), and the heavy quarks ($c$, $b$ and $t$) is large. Heavy Quark Effective Theory (HQET) [13, 35, 36] is one standard approach to solve non–perturbative *QCD* and has been built on this fact. It exploits the large mass difference to make a $\frac{1}{m_Q}$ expansion approximation, where $m_Q$ is the heavy quark mass.

In the present work we employ the parton model for the non–perturbative *QCD* region. The parton model has been successful to explain lepton–nucleon scatterings. The physical region of lepton invariant mass $W^2$ in the $B$-meson decay is $0 \leq W^2 \leq (M_B - M_X)^2$, where $M_B$ is the mass of the $B$-meson, and

$M_X$ the mass of the hadrons in the final states. Considering that 1 $GeV^2$ << $(M_B - M_X)^2$, one can use the Light–Cone expansion in the relevant region of $W^2$, which is 1 $GeV^2$ << $W^2$ < $(M_B - M_X)^2$. The current commutator between the $B$-meson state $\langle B|[\, J_\mu(y),\, J_\nu^\dagger(0)\,]|B\rangle$, where $y$ is the separation of the two currents, incorporates the non–perturbative $QCD$ part of $B$-meson decays and can be expressed in terms of a single distribution function $f(x)$ in the Light–Cone limit, where $y^2 \sim 0$. The interpretation of this distribution function $f(x)$ is the probability to find a $b$-quark with the momentum fraction $x$ inside the $B$-meson. The specific theoretical explanation on the Light–Cone expansion is found in Chapter 2. We especially investigate the model by Jin and Paschos [32, 33]

$$f_{jp}(x) = N_{jp}\,\frac{x(1-x)}{(x-b)^2 + a^2}\,. \tag{1.9}$$

Parameters in HQET are used to determine the parameters $a$ and $b$ in Eq.(1.9).

Apart from the parton model there is the ACCMM model [7]. Its supposition is that the $B$-meson consists of a $b$-quark and a spectator quark. The spectator quark is supposed to have definite mass $m_{spec}$ and momentum $P_{spec}$, and considered quasi–free, whereas the $b$-quark is treated as a virtual particle with an invariant mass $m_{b,inv}$

$$m_{b,inv}^2(P_{spec}^2) \equiv M_B^2 \;+\; m_{spec}^2 \;-\; 2M_B\sqrt{P_{spec}^2 + m_{spec}^2}\,, \tag{1.10}$$

where $M_B$ denotes the $B$-meson mass. A comparison of the parton model and the ACCMM model is found in [34].

Theoretical background on semi–leptonic $B$-meson decay and the Light–Cone expansion is explained in Chapter 2. The Standard Model and the $CKM$ matrix elements are described in Section 2.1, and a general overview of semi–leptonic $B$-meson decay is in Section 2.2. In Section 2.3 we present the Light–Cone expansion and its connection with the parton model. The experimental status of $B$-meson decay is described in Section 2.4.

The specific calculation procedure is presented in Chapter 3. It contains the kinematic variables in Section 3.1, a short note on the leading order approximation in Section 3.2, the virtual gluon corrections at next–to–leading order in Section 3.3.1, and the real gluon corrections in Section 3.3.2. The final result, which is the sum of the real and virtual gluon corrections, is given in Section 3.3.3.

All spectra from $b$-quark decays that are relevant to the determination of $V_{ub}$ are displayed in Chapter 4. Traditionally, $V_{ub}$ is determined from the energy spectrum of the charged lepton in the final state, which is presented in Section 4.1. Due to the large background of $b \to c$ decay the energy band $\Delta E_e$ which can be used for the analysis for $V_{ub}$ is very narrow and prevents precise analysis. The leptonic invariant mass $W^2$ spectrum is found in Section 4.2. The hadronic

energy $E_H$ spectrum and the hadronic invariant mass $M_H$ spectrum are presented in Sections 4.3 and 4.4, respectively.

In Chapter 5, the naive parton model is used to obtain the spectra from $B$-meson decay. Eq.(1.9) is used for the distribution function, which is the model suggested by Jin and Paschos [32, 33]. Spectra from the $B$-meson decay are presented and compared to the ones from $b$-quark decays in Section 5.2.

Apart from the naive parton model, we consider $QCD$ interactions between quarks inside the $B$-meson. The $b$-quark in the $B$-meson can undergo $QCD$ interactions before it decays into a light quark through the weak interaction. The distribution function $f(x)$, which depends only on the scaling variable $x$, is modified and obtains the lepton invariant mass dependence from the $QCD$ corrections.

We employ the Leading Logarithmic Approximation (LLA) and consider only the logarithmically divergent terms. We factorize the $QCD$ correction terms, which are proportional to $\ln(\mu^2/m_b^2)$, where $\mu^2 \equiv m_b^2 - W^2$, and contain collinear divergences in the limit of $m_b \to 0$, at the factorization scale $\mu_f^2$. The collinearly divergent part $\ln(\mu_f^2/m_b^2)$ is absorbed into the distribution function and the distribution function, therefore, obtains the $\mu^2$ dependence. Finally, we recover the Altarelli–Parisi evolution equation from the change of the distribution function and obtain the evolution equation of the $\mu^2$ dependent distribution function $f(x, \mu^2)$. Altarelli–Parisi evolution of the distribution function $f(x, \mu^2)$ includes further $QCD$ interactions of the $b$-quark before it decays into a light quark through the weak interaction. In Chapter 6 the LLA and factorization procedures are described in Section 6.2, and the resulting spectra from $B$-meson decay with the evolved distribution function $f(x, \mu^2)$ are presented in Section 6.3.

# Chapter 2

# Theoretical background and Experimental status

## 2.1 Standard model and *CKM* matrix

In the low energy limit the electro–weak interaction is expressed in an effective form as

$$\mathcal{L}_{weak} = \frac{G_F}{\sqrt{2}} \mathcal{J}^{\mu}(x)\, \mathcal{J}^{\dagger}_{\mu}(x)\,, \tag{2.1}$$

where the Fermi constant $G_F$ is given by

$$\frac{G_F}{\sqrt{2}} = \frac{g_w^2}{8M_W^2}\,, \tag{2.2}$$

and $g_w$ is the weak coupling constant, $M_W$ the mass of $W$-boson.
The weak current $\mathcal{J}^{\mu}(x)$ is composed of the leptonic $l^{\mu}(x)$ and the hadronic $h^{\mu}(x)$ currents

$$\mathcal{J}^{\mu}(x) = l^{\mu}(x) + h^{\mu}(x)\,, \tag{2.3}$$

$$l^{\mu}(x) = \sum_{\ell=e,\nu,\tau} \bar{\ell}(x)\gamma^{\mu}(1-\gamma_5)\nu_{\ell}(x)\,, \tag{2.4}$$

$$h^{\mu}(x) = \sum_{i=u,c,t} \sum_{j=d,s,b} V_{ij}\, \bar{q}_i(x)\gamma^{\mu}(1-\gamma_5) q_j(x)\,. \tag{2.5}$$

The *CKM* matrix, which is based on the fact that the gauge eigenstates are not the mass eigenstates, is given by

$$\mathbf{V} = \begin{pmatrix} V_{ud} & V_{us} & V_{ub} \\ V_{cd} & V_{cs} & V_{cb} \\ V_{td} & V_{ts} & V_{tb} \end{pmatrix} .$$

In a customary way, the *CKM* matrix is described in terms of four Wolfenstein parameters $(\lambda, A, \rho, \eta)$

$$\mathbf{V} = \begin{pmatrix} 1 - \frac{\lambda^2}{2} & \lambda & A\lambda^3(\rho - i\eta) \\ -\lambda & 1 - \frac{\lambda^2}{2} & A\lambda^2 \\ A\lambda^3(1 - \rho - i\eta) & -A\lambda^2 & 1 \end{pmatrix} + \mathcal{O}(\lambda^4) .$$

In this expression each element of the *CKM* matrix is expanded in terms of powers of $\lambda = |V_{us}| \sim 0.22$. $\eta$ represents the *CP* violating factor and *CP*–violation is observed when $\eta \neq 0$.

All *CKM* matrix elements are mostly determined from weak decays of the relevant quarks or from deep inelastic neutrino scatterings. Semi–leptonic kaon and hyperon decays give $|V_{us}|$, semi–leptonic $D$ decays $|V_{cs}|$, semi–leptonic exclusive and inclusive $B$ decays $|V_{cb}|$, and the endpoint spectrum in semi–leptonic $B$ decays $|V_{ub}|/|V_{cb}|$. From nuclear beta decays $|V_{ud}|$ is obtained, and the element $|V_{cd}|$ is determined from neutrino and anti–neutrino production of charm off valence $d$-quark. The latest information on the absolute values of the *CKM* elements from both direct measurements and three generation unitarity is summarized by [27]

$$|\mathbf{V}| = \begin{pmatrix} 0.9741 - 0.9756 & 0.219 - 0.226 & 0.0025 - 0.0048 \\ 0.219 - 0.226 & 0.9732 - 0.9748 & 0.038 - 0.044 \\ 0.004 - 0.014 & 0.037 - 0.044 & 0.9990 - 0.9993 \end{pmatrix} .$$

As is seen in the table above, large uncertainties exist for $|V_{ub}|$ and $|V_{td}|$. The uncertainties stem from both the experimental and theoretical side. The uncertainties from theory are mostly from the non–perturbative aspects of *QCD*, which explain hadronization.

The $B$-meson is a bound state of a $b$-quark and a surrounding anti-quark, together forming a color neutral state. The fact that the $b$-quark is heavy compared to other quarks expect the $t$-quark, enables us to think that the main component of $B$-meson decay is the decay of $b$-quarks inside the $B$-meson, but one cannot detect a $b$-quark separately. That is, its kinematic properties are not physically detectable, and this fact results in uncertainties in the theoretical expectation.

At first, people supposed that the $b$-quark should take all of the momentum of the physical $B$-meson state and ignored the non–perturbative aspect of *QCD*, which arises when the coupling constant $\alpha_s$ is not small enough to be handled perturbatively as the momentum scale approaches $\mu \sim \Lambda_{QCD}$.

There have been several models to explain this non–perturbative *QCD* part. One is Heavy Quark Effective Theory (HQET), which expands the Lagrangian in terms of powers of the mass of heavy quarks $m_Q$. There are also *QCD* sum rules or Lattice *QCD* models. However, all these models have strong and weak points at the same time and need to be improved. The main purpose of this work is to improve the determination of $|V_{ub}|$ by investigating various spectra from the semi–leptonic $B$-meson decay. In the next section the general knowledge on semi–leptonic $B$ decays is explained.

## 2.2 Semi–leptonic $B$-meson decays

In general, $B$-mesons have three main decay modes. One is leptonic decay, another semi–leptonic decay, and the third non–leptonic decay. In semi–leptonic decays a lepton–pair is produced in the final states in addition to a hadronic state $X$

$$B \longrightarrow \ell + \bar{\nu}_\ell + X\,, \tag{2.6}$$

whereas only quark pairs, or mesons, are produced in the non–leptonic decay. Semi–leptonic $B$ decays are described with the interaction of leptonic and hadronic currents. The differential decay rate of inclusive semi–leptonic $B$-meson decays is expressed as

$$\begin{aligned} d\Gamma &= \frac{1}{2E_B}\sum_n \frac{d^3p_\ell}{(2\pi)^3 2E_\ell}\frac{d^3p_\nu}{(2\pi)^3 2E_\nu}\left[\prod_{i=1}^{n}\frac{d^3P_i}{(2\pi)^3 2E_i}\right]\times \\ &\quad (2\pi)^4\delta^{(4)}(P_B - q - \sum_{i=1}^{n} P_i)\overline{|\mathcal{M}|^2}\,, \end{aligned} \tag{2.7}$$

where $q$ is the four–momentum of the lepton system $q = p_\ell + p_\nu$ and at the same time, the four–momentum of the virtual $W$–boson which is exchanged during the flavor change. $p_\ell$ is the four–momentum of the lepton and $p_\nu$ the four–momentum of the anti–neutrino in the final states. $n$ denotes all possible hadronic final states. In the case of inclusive decays, all possible hadronic final states are summed. In the decay of the virtual $W$–boson, one lepton pair, i.e. $\ell + \bar{\nu}_\ell$, is produced. Figure 2.1 shows the semi–leptonic decay process, where one lepton pair and corresponding possible hadronic states denoted by $X$ are in the final state.

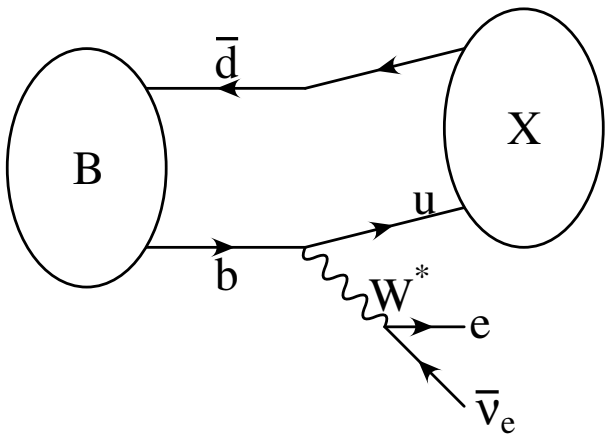


Figure 2.1: Inclusive semi–leptonic $B$-meson decay.

The amplitude of semi–leptonic $B$ decays is described as

$$\mathcal{M} = V_{fb} \frac{G_F}{\sqrt{2}} \bar{u}(p_\ell)\gamma^\mu(1-\gamma_5)v(p_\nu)\,\langle n|J_\mu(0)|B\rangle\,, \tag{2.8}$$

where $f$ denotes the flavor of the quark in the final state, which can be $u$ or $c$. The corresponding current in Eq.(2.8) is

$$J_\mu(x) \;=: \bar{q}_f(x)\gamma_\mu(1-\gamma_5)b(x) : \,. \tag{2.9}$$

The $B$-meson state $|B\rangle$ with momentum $P_B^\mu$ is normalized as

$$\langle B|B\rangle = 2E_B\,(2\pi)^3\,\delta^{(3)}(\vec{0})\,. \tag{2.10}$$

Semi–leptonic decay is generally expressed with a leptonic and a hadronic tensor. Whereas the leptonic tensor is completely well known, the hadronic tensor needs more understanding and theoretical considerations. For unpolarized leptons the decay rate is written as

$$d\Gamma = \frac{G_F^2}{(2\pi)^5}\,\frac{|V_{fb}|^2}{E_B}\,\frac{d^3p_\ell}{2E_\ell}\,\frac{d^3p_\nu}{2E_\nu}\,L^{\mu\nu}\,W_{\mu\nu}\,, \tag{2.11}$$

where the leptonic tensor $L^{\mu\nu}$ is defined as

$$L^{\mu\nu} = 2\,(p_\ell^\mu p_\nu^\nu \,+\, p_\nu^\mu p_\ell^\nu \,-\, g^{\mu\nu}(p_\ell\cdot p_\nu) \,+\, i\varepsilon^{\mu\nu}_{\alpha\beta}p_\ell^\alpha p_\nu^\beta)\,, \tag{2.12}$$

and the hadronic tensor $W_{\mu\nu}$

$$W_{\mu\nu} = \sum_n \int \left[ \prod_{i=1}^{n} \frac{d^3 P_i}{(2\pi)^3 2E_i} \right] \times (2\pi)^3 \, \delta^{(4)}(P_B - q - \sum_{i=1}^{n} P_i) \, \langle B|J_\nu^\dagger(0)|n\rangle\langle n|J_\mu(0)|B\rangle \, . \quad (2.13)$$

Summing up all possible hadronic final states in Eq.(2.13), the hadronic tensor can be expressed in terms of the commutator of two currents,

$$W_{\mu\nu} = -\frac{1}{2\pi} \int d^4 y \, e^{iq\cdot y} \, \langle B|[\, J_\mu(y), \, J_\nu^\dagger(0)\,]|B\rangle \, , \quad (2.14)$$

where $q$ is the four–momentum of the lepton pair in the final state. Introducing the hadronic structure functions $W_i(q^2, (q \cdot P_B))$, we write the hadronic tensor as

$$\begin{aligned} W_{\mu\nu} &= -g_{\mu\nu} W_1(q^2, (q\cdot P_B)) + \frac{P_{B\mu} P_{B\nu}}{M_B^2} W_2(q^2, (q\cdot P_B)) \\ &\quad - i\varepsilon_{\mu\nu\alpha\beta} \frac{P_B^\alpha q^\beta}{M_B^2} W_3(q^2, (q\cdot P_B)) + \frac{q_\mu q_\nu}{M_B^2} W_4(q^2, (q\cdot P_B)) \\ &\quad + \frac{(P_{B\mu} q_\nu + P_{B\nu} q_\mu)}{M_B^2} W_5(q^2, (q\cdot P_B)) \, , \end{aligned} \quad (2.15)$$

where $M_B$ is the $B$-meson mass. The hadronic structure functions $W_i(q^2, (q\cdot P_B))$ include all the effects from non–perturbative $QCD$ for the inclusive process.

## 2.3 Light–Cone Expansion

In the previous section the hadronic tensor is found to be expressed by the current commutator $[\, J_\mu(y), \, J_\nu^\dagger(0)\,]$ as

$$W_{\mu\nu} = -\frac{1}{2\pi} \int d^4 y \, e^{iq\cdot y} \, \langle B|[\, J_\mu(y), \, J_\nu^\dagger(0)\,]|B\rangle \, . \quad (2.16)$$

One main goal of the calculation of $B$-meson decay is how to resolve the hadronic tensor. The largest contribution of this integration is from the region where $(q \cdot y) \sim 1$, where the exponential oscillates less rapidly. It is necessary to investigate

the relation between $q$ and $y$ which fulfills the condition $(q \cdot y) \sim 1$. When the Lorentz frame where $q = (q_0, 0, 0, q_3)$ is chosen, the scalar product of $(q \cdot y)$ is written as

$$\begin{aligned} q \cdot y &= q_0 y_0 - q_3 y_3 \\ &= \frac{1}{2}(q_0 + q_3)(y_0 - y_3) + \frac{1}{2}(q_0 - q_3)(y_0 + y_3)\,. \end{aligned} \tag{2.17}$$

We approximate

$$\begin{aligned} (q_0 + q_3)(y_0 - y_3) &\sim 1\,, \\ (q_0 - q_3)(y_0 + y_3) &\sim 1\,, \end{aligned} \tag{2.18}$$

and consequently, obtain

$$\begin{aligned} y_0 - y_3 &\sim \frac{1}{(q_0 + q_3)}\,, \\ y_0 + y_3 &\sim \frac{1}{(q_0 - q_3)}\,, \end{aligned} \tag{2.19}$$

and

$$y^2 = y_0^2 - |\vec{y}|^2 \leq y_0^2 - y_3^2 \sim \frac{1}{q_0^2 - q_3^2} = \frac{1}{q^2}\,. \tag{2.20}$$

Therefore, the hadronic tensor $W_{\mu\nu}$ in Eq.(2.16) obtains the dominant contribution from the region

$$0 \leq y^2 \leq \frac{1}{q^2}\,. \tag{2.21}$$

As $q^2$ becomes larger, $y^2$ stays inside a domain near 0, i.e. near the Light–Cone where $y^2 = 0$, and this makes it possible to expand the hadronic tensor $W_{\mu\nu}$ in terms of polynomials of $y^2$.

In the case of inclusive semi–leptonic $B$–meson decays, $q^2$ has the physical range of

$$M_e^2 \leq q^2 \leq (M_B - M_{Xmin})^2\,. \tag{2.22}$$

$M_{Xmin}$ is the minimum value of the hadronic invariant mass in final states and $M_e$ denotes the mass of the charged lepton in the final states. In the region of $q^2 \geq$

1 $GeV$ the hadronic tensor can be said to have Light–Cone dominance. Using the fact that the hadronic tensor has Light–Cone dominance, we now proceed with a Light–Cone expansion of the current commutator $[\, J_\mu(y),\, J_\nu^\dagger(x)\,]$.

The current commutator is resolved with the application of Wick's theorem as

$$\begin{aligned}[\, J_\mu(y),\, J_\nu^\dagger(x)\,] \;=\;& \bar{q}_f(y)\gamma_\mu(1-\gamma_5)\{\, b(y),\, \bar{b}(x)\,\}\gamma_\nu(1-\gamma_5)q_f(x) - \\ & \bar{b}(x)\gamma_\nu(1-\gamma_5)\{\, q_f(x),\, \bar{q}_f(y)\,\}\gamma_\mu(1-\gamma_5)b(y)\,, \qquad (2.23)\end{aligned}$$

and $\{\, b(y),\, \bar{b}(x)\,\}$ is the anti–commutator. The first term on the R.H.S in Eq.(2.23) is ignored, for this corresponds to the production of $\bar{b}-\bar{u}$ pairs, which is not included in our consideration. Consequently, we can simplify the current commutator in Eq.(2.23) as

$$[\, J_\mu(y),\, J_\nu^\dagger(x)\,] = -\bar{b}(x)\gamma_\nu(1-\gamma_5)\{\, q_f(x),\, \bar{q}_f(y)\,\}\gamma_\mu(1-\gamma_5)b(y)\,. \qquad (2.24)$$

The anti–commutator in Eq.(2.24) is solved as

$$\begin{aligned}\{\, q_f(x),\, \bar{q}_f(y)\,\} \;&=\; i\mathcal{S}_{\alpha\beta}(x-y)\,, && (2.25)\\ \mathcal{S}_{\alpha\beta}(x-y) \;&=\; (i\,\partial\!\!\!/ + m_f)_{\alpha\beta}\,\Delta_f(x-y)\,, && (2.26)\end{aligned}$$

with the Pauli–Jordan representation

$$i\Delta_f(x) = \frac{1}{(2\pi)^3}\int d^4k\, e^{-ik\cdot x}\,\varepsilon(k_0)\,\delta(k^2-m_f^2)\,. \qquad (2.27)$$

Finally, the matrix element in Eq.(2.16) is expressed as

$$\begin{aligned}&\langle B|[\, J_\mu(y),\, J_\nu^\dagger(0)\,]|B\rangle = \\ &2(\mathcal{S}_{\mu\alpha\nu\beta} - i\varepsilon_{\mu\alpha\nu\beta})\,[\partial^\alpha\Delta_q(y)]\,\langle B|\bar{b}(0)\gamma^\beta(1-\gamma_5)b(y)|B\rangle\,, \qquad (2.28)\end{aligned}$$

where $\mathcal{S}_{\mu\alpha\nu\beta} = g_{\mu\alpha}g_{\nu\beta} + g_{\mu\beta}g_{\nu\alpha} - g_{\mu\nu}g_{\alpha\beta}$.

The reduced matrix element $\langle B|\bar{b}(0)\gamma^\beta(1-\gamma_5)b(y)|B\rangle$ now has the general tensor structure

$$\langle B|\bar{b}(0)\gamma^\beta(1-\gamma_5)b(y)|B\rangle = 4\pi\, P_B^\beta\,\mathcal{F}(y^2, y\cdot P_B)\,, \qquad (2.29)$$

and the function $\mathcal{F}(y^2, y\cdot P_B)$ can be Light–Cone–like expanded:

$$\mathcal{F}(y^2, y\cdot P_B) = \sum_{n=0}^{\infty} \frac{(y^2)^n}{n!} \left[\frac{d^n \mathcal{F}(y^2, y\cdot P_B)}{d(y^2)^n}\right]_{y^2=0} . \tag{2.30}$$

In this way, the hadronic tensor can be expanded with polynomials of $y^2$ with an appropriate function $\mathcal{F}(y^2, (q\cdot y))$. In the region of $y^2 \leq 1$, we are allowed to take the limit of $y^2 \sim 0$ and it leaves us the first term of the series in Eq.(2.30). We define the first term in Eq.(2.30) as

$$\mathcal{F}_0(y\cdot P_B) \equiv \mathcal{F}(y^2 = 0, y\cdot P_B) . \tag{2.31}$$

We define the distribution function $f(x)$ as the Fourier transform of $\mathcal{F}_0(y\cdot P_B)$

$$\begin{aligned} f(x) &\equiv \int d(y\cdot P_B)\, e^{i\,x(y\cdot P_B)} \mathcal{F}_0(y\cdot P_B) \\ &= \frac{1}{4\pi M_B^2} \int d(y\cdot P_B)\, e^{i\,x(y\cdot P_B)} \langle B|\bar{b}(0) \not{P}_B (1-\gamma_5) b(y)|B\rangle|_{y^2=0} . \end{aligned} \tag{2.32}$$

The distribution function $f(x)$ describes the distribution of momentum of the $b$-quark inside of the $B$-meson. The inverse Fourier transform reads

$$\mathcal{F}_0(y\cdot P_B) = \frac{1}{2\pi} \int dx\, e^{-i\,x(y\cdot P_B)} f(x) . \tag{2.33}$$

After combining Eqs.(2.16), (2.28), and (2.33) and integrating over $y$, we obtain

$$\begin{aligned} W_{\mu\nu} &= 4(\mathcal{S}_{\mu\alpha\nu\beta} - i\varepsilon_{\mu\alpha\nu\beta}) \int dx\, f(x) \times \\ &\quad \varepsilon(xP_B^0 - q^0)\, \delta[\,(xP_B - q)^2 - m_f^2\,](xP_B - q)^\alpha P_B^\beta . \end{aligned} \tag{2.34}$$

From the argument of the $\delta$-function in Eq.(2.34), we obtain two scaling variables $\chi_\pm$ and they read

$$\chi_\pm = \frac{q\cdot P_B \pm \sqrt{(q\cdot P_B)^2 - M_B^2(q^2 - m_f^2)}}{M_B^2} . \tag{2.35}$$

The structure functions $W_i$'s are expressed with these scaling variables $\chi_\pm$ and the distribution function $f(x)$, and the specific expression of $W_i$'s are

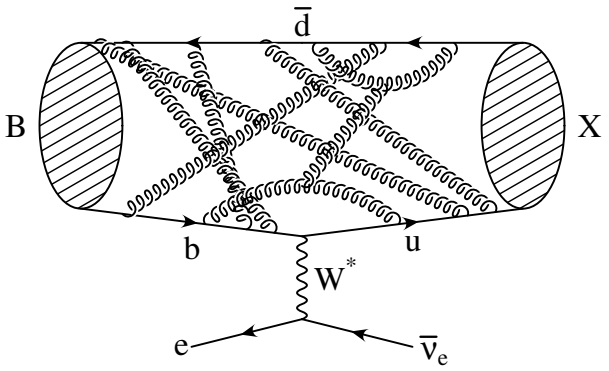


Figure 2.2: *QCD* interactions inside $B$-mesons.

$$W_1 = 2[\, f(\chi_+) + f(\chi_-)\,], \tag{2.36}$$

$$W_2 = \frac{8}{\chi_+ - \chi_-}[\, \chi_+ f(\chi_+) - \chi_- f(\chi_-)\,], \tag{2.37}$$

$$W_3 = -\frac{4}{\chi_+ - \chi_-}[\, f(\chi_+) - f(\chi_-)\,], \tag{2.38}$$

$$W_4 = 0\,, \tag{2.39}$$

$$W_5 = W_3\,. \tag{2.40}$$

We can adopt several types of distribution functions. In Chapter 6, we present more discussion about the distribution function.

The $b$-quark extracted from the $B$-meson undergoes *QCD* interactions with other quarks and gluons inside the $B$-meson. For example, $b$-quark may emit gluons which are absorbed by other quarks or gluons. This complication of $B$-meson decay is depicted in Figure 2.2. For momentum scale $\mu \geq \Lambda_{QCD}$, we can consider parton–type evolution of the $b$-quark inside the $B$-meson. In Section 6 we explain $b$-quark evolution.

## 2.4 Experimental Research on $B$-meson decays

There are two main purposes of experiments on $B$-mesons. One purpose is to test the relation of matter and anti–matter and consequently to investigate *CP*–

violation. The other purpose is to test the Standard Model and especially to determine the *CKM* matrix elements. The experimental groups are CLEO at CESR at Cornell University, *BABAR* at the PEP-II at SLAC, and Belle at KEKB at KEK, and CDF at Fermi–lab. CDF uses the proton–anti proton collider Tevatron, whereas all other experimental groups use electron–positron colliders. A short overview of these experimental groups is presented in this Section.

• **Experiments at CLEO**

CLEO is a detector at the Cornell Electron–Positron Storage Ring (CESR). CESR is an $e^+ - e^-$ collider which provides symmetric beam energy, whereas collisions at *BABAR* and Belle are done with asymmetric beam energies. Collisions of electron–positron at CESR take place at the center–of–mass energies between 9 $GeV$ and 12 $GeV$.

The CLEO collaboration measures the *CKM* matrix elements, *CP*–violation, and the HQET parameters $\bar{\Lambda}$, $\lambda_1$, and $\lambda_2$ as well. The ratio $|V_{ub}|/|V_{cb}|$ was measured for the first time at CLEO by detection of inclusive leptons from the semi–leptonic $B$-meson decay that are beyond the kinematic end point for the final states with charm mesons [43]. Recently it became possible to reconstruct exclusive transitions at CLEO . The hermiticity of the CLEO detector makes several analysis techniques usable to reconstruct the neutrino four vectors [44, 45]. CLEO has turned itself into a charm factory since 2001. It is expected to make considerable measurements on charmed mesons.

• **Experiments at *BABAR***

The *BABAR* experiment primarily studies *CP*–asymmetries in neutral $B$-meson decays. Besides, the *BABAR* experiment measures the *CKM* matrix element $V_{ub}$ and a number of rare $B$-meson decays as well, which also provide useful constraints on the fundamental parameters of the Standard Model [46]. The *BABAR* collaboration has achieved the highest integrated luminosity, $\sim$ 94 $f\mathrm{b}^{-1}$ [54]. Belle, in contrast, obtained 89.6 $f\mathrm{b}^{-1}$ [55]. The high luminosity at *BABAR* makes it possible to make more precise analysis and to study various processes. The *BABAR* detector is sited at PEP-II at SLAC, which is especially designed for $B$ physics.

PEP-II is an electron–positron collider where the electron and positron have asymmetric energies. The electrons produced at PEP-II have 9 $GeV$ and the positrons 3.1 $GeV$. The design luminosity is $3 \times 10^{33}$ $cm^{-2}s^{-1}$. The end view of the *BABAR* detector is displayed in Figure 2.3. The important parts of the *BABAR* detector are a Silicon Vertex Tracker (SVT), a Drift Chamber (DCH), a Detector of Internally Reflected Cherenkov light (DIRC), a Caesium Iodide Electro-magnetic Calorimeter (EMC), an Insulated Flux Return (IFR), and a super–conducting coil, which supplies 1.5 $Tesla$ solenoidal magnetic fields [46].

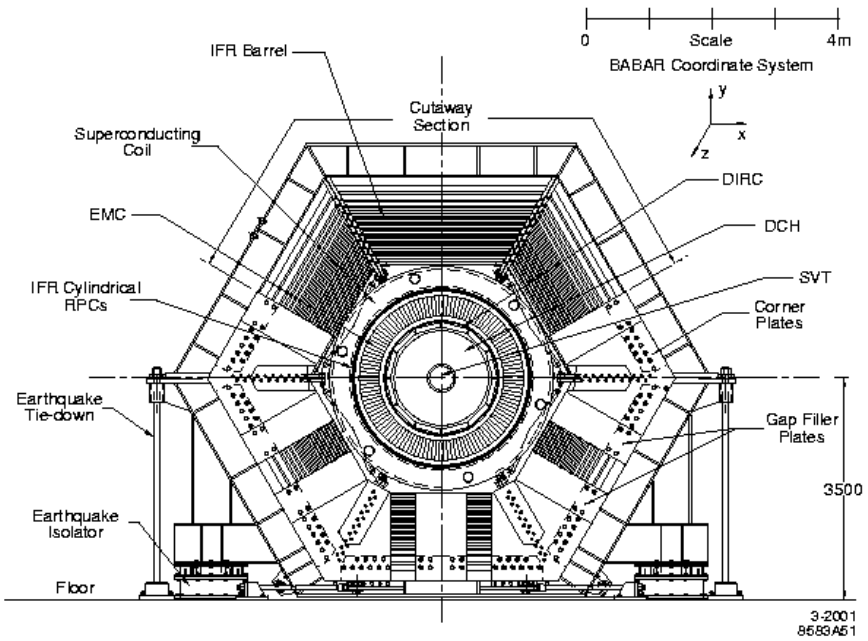


Figure 2.3: End view of the *BABAR* detector.

The STV provides position information on charged tracks and very low-energy charged particles. The DCH is filled with helium-based gas and provides the main momentum measurement for charged particles. The DIRC is used for identifying charged hadron particles and the EMC for identifying neutral hadron particles, which is studied particularly for *CP*-violation. The IFR is for detecting muon and neutral hadron particles.

- **Experiments at Belle**

Another important $B$–Factory is KEKB [48] used by the Belle detector. KEKB is an electron–positron collider and also uses asymmetric beam lines like PEP-II. The electron beam is 3.5 $GeV$ and the positron beam at higher energy, 8 $GeV$. The design luminosity of KEKB is $1.0 \times 10^{34}\ cm^{-2}s^{-1}$.

The Belle detector is described in [51]. Figure 2.4 shows the side view of the Belle detector. The detector is surrounded by 1.5 $Tesla$ magnetic field produced by super–conducting solenoidal coils. The Silicon Vertex Detector (SVD) measures $B$-meson decay vertices. To observe time–dependent $CP$ asymmetries in $B$–meson decays, which is the primary goal of the Belle, the difference in $z$–vertex positions for $B$-meson pairs should be measured with a precision of $\sim 100\,\mu m$. A wire drift chamber (CDC) tracks charged particles and provides $dE/dx$ measurements for particle identification.

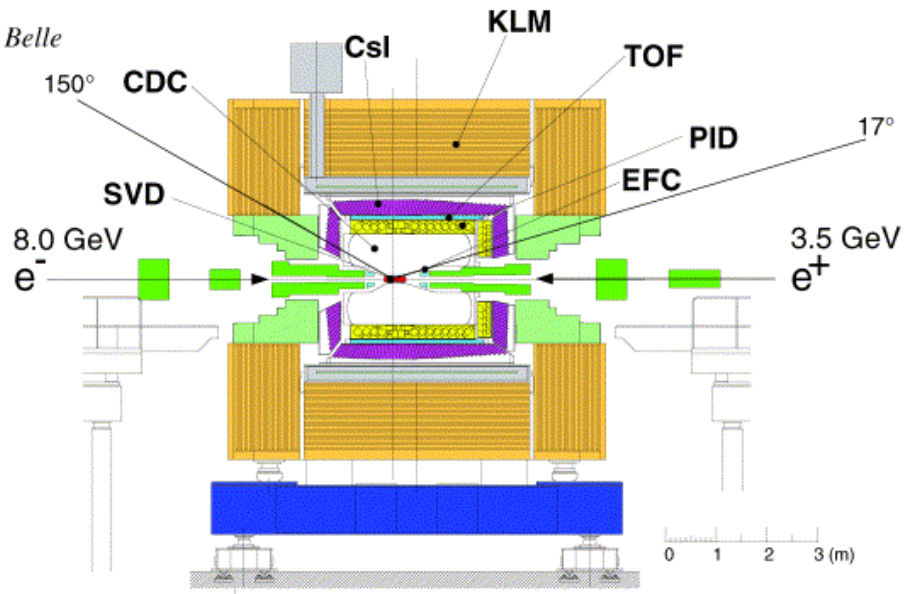


Figure 2.4: Side view of the Belle detector.

• **Experiments at CDF**

The $b$-quark was first observed by the Collider Detector at Fermilab (CDF) collaboration in 1977. The experiment was a collision of protons with energy 400 $GeV$ on fixed target nuclei, and an enhancement of the $\mu\bar{\mu}$ pair production rate was observed. The $\mu\bar{\mu}$ production enhancement at the invariant mass $\sim$ 9.5 $GeV/c^2$ was interpreted as the $b\bar{b}$ bound state called $\Upsilon$ [52].

Unlike CLEO , *BABAR* , and Belle which use electron–positron colliders, CDF uses the Tevatron collider at center of mass energy 1.8 $TeV$, which brings protons with energy 900 $GeV$ into collisions with anti–protons with energy 900 $GeV$. CDF [53] has four main tracking devices: the silicon vertex detector (SVX), the vertex time projection chamber (VTX), the central tracking chamber (CTC), and the central drift tube array (CDT). Among these devices, the SVX identifies the decay points of the long lived $b$-quarks traveling away from the $p\bar{p}$ collision and provides information about the transverse path of charged particles. The VTX is for reconstructing the tracks of charged particles and essential for calculating the kinematics of reconstructed $B$-meson decays.

# Chapter 3

# *QCD* Corrections using the Dimensional Regularization Scheme

We present the *QCD* corrections at order $\alpha_s$ to semi–leptonic $b$-quark decay with the $b \to u$ transition: $b \longrightarrow u + e + \bar{\nu}_e$. The *QCD* corrections receive contributions from both virtual and real gluon corrections. We renormalize all fields and vertices using dimensional regularization, and both infrared and ultraviolet singularities appear in forms of $\frac{1}{\varepsilon}$ and $\frac{1}{\varepsilon^2}$, where $\varepsilon$ denotes the deviation of the number of space–time dimensions from 4. The specific procedure of the calculation using dimensional regularizaiton is presented in this Chapter.

## 3.1 Kinematic Variables

Noting that the particles appearing in the processes $b \longrightarrow u + e + \bar{\nu}_e$ and $b \longrightarrow u + g + e + \bar{\nu}_e$ are a $b$-quark, $u$-quark, electron, anti–electron–neutrino and a gluon, it is convenient to define scaled momenta as kinematic variables. First of all, we denote the four–momentum of the $b$-quark as $p_b$ and the four–momentum of the $u$-quark as $p_u$, the four–momentum of the electron as $p_e$, the four–momentum of the anti–electron–neutrino as $p_\nu$ and the four–momentum of the gluon as $p_g$. We define $P$ as the momentum of the quark–gluon system $P = p_u + p_g$, $W$ as the

momentum of the lepton system $W = p_e + p_\nu$. Energy–momentum conservation reads $p_b = p_u + p_g + p_e + p_\nu = P + W$. The $b$-quark mass is denoted as $m_b$ and all other light particles and the gluon are massless, i.e. $p_u^2 = p_e^2 = p_\nu^2 = p_g^2 = 0$. The scaled Lorentz invariant variables are defined as the following:

$$z \equiv \frac{P^2}{p_b^2}\,, \qquad y \equiv \frac{W^2}{p_b^2}\,, \qquad x_e \equiv \frac{2E_e}{m_b}\,, \qquad x_\nu \equiv \frac{2E_\nu}{m_b}\,.$$

These variables take values in the regions

$$\begin{aligned} 0 &\leq x_e \leq 1\,, \\ 0 &\leq y \leq x_e\,, \\ 0 &\leq z \leq (1-x_e)(1-y/x_e)\,. \end{aligned} \tag{3.1}$$

Instead of the full propagator of the virtual $W$–boson, we employ the effective low–energy Lagrangian, where the $W$–boson propagator contributes as $1/M_W^2$, where $M_W$ is the $W$–boson mass. The effective coupling constant of the weak interaction is expressed by the Fermi constant

$$\frac{G_F}{\sqrt{2}} = \frac{g_w^2}{8\,M_W^2}\,. \tag{3.2}$$

The effective Lagrangian for semi–leptonic $b$-quark decay into a $u$-quark reads

$$\mathcal{L}_{eff} = \frac{G_F}{\sqrt{2}}\,V_{ub}\,\bar{e}(x)\gamma^\mu(1-\gamma_5)\nu_e(x)\;\bar{u}(x)\gamma_\mu(1-\gamma_5)b(x)\,, \tag{3.3}$$

where $V_{ub}$ is the $CKM$ matrix element for $b \to u$ flavor transition, and $e(x)$, $\nu_e(x)$, $u(x)$ and $b(x)$ denote the electron field, neutrino field, $u$-quark field and $b$-quark field, respectively.

## 3.2 Born Approximation

The Feynman diagram of the tree level $b$-quark decay is depicted in Figure 3.1. The amplitude of the Born approximation is given by

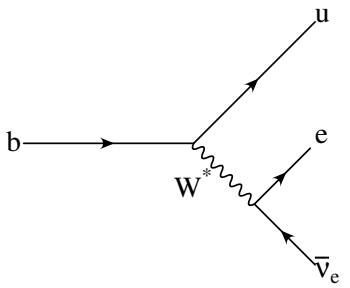


Figure 3.1: Feynman diagram for the Born approximation.

$$\mathcal{M}^{Born} = \frac{G_F}{\sqrt{2}} V_{ub}\, \bar{u}(p_u)\gamma^\mu(1-\gamma_5)u(p_b)\ \bar{u}(p_e)\gamma_\mu(1-\gamma_5)v(p_\nu)\,, \tag{3.4}$$

and the Born approximation of the differential decay rate is obtained as

$$\frac{d\Gamma^{Born}}{dx_e\, dy} = \frac{G_F^2\, m_b^5}{16\,\pi^3}\,|V_{ub}|^2\,(x_e - y)(1 - x_e + y)\,. \tag{3.5}$$

The electron energy spectrum from the Born Approximation is shown in Figure 3.2 together with the radiatively corrected spectrum, and we can observe visible change by the *QCD* corrections at the end point region of the electron energy. In Section 3.3 we present the explicit calculation of *QCD* corrections to the semi–leptonic $b$-quark decay.

## 3.3 *QCD* Radiative Corrections

The Born approximation of the decay rate receives radiative corrections from perturbative *QCD* that are expanded in powers of the strong coupling constant $\alpha_s$:

$$d\Gamma = d\Gamma^{Born} + d\Gamma^{\alpha_s} + d\Gamma^{\alpha_s^2} + \ldots\,. \tag{3.6}$$

We present the calculation of the first order of $\alpha_s$ corrections in this section. The virtual gluon contributions are denoted by $d\Gamma^V$ and the real gluon contributions by $d\Gamma^R$, so the total radiative corrections of order of $\alpha_s$ read

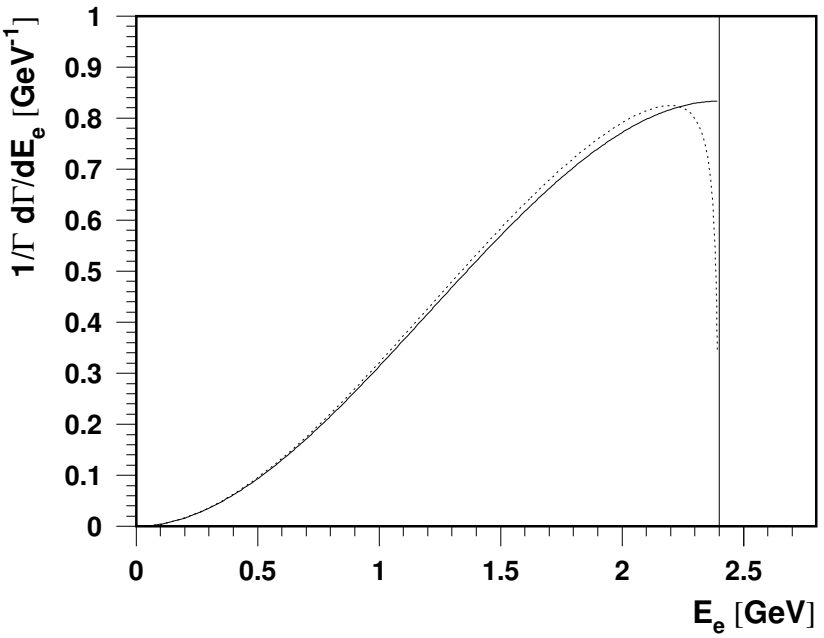


Figure 3.2: The solid line shows the Born approximation of the electron energy spectrum, and the dotted line is the spectrum with radiative corrections at $\alpha_s = 0.22$.

$$d\Gamma^{\alpha_s} = d\Gamma^V + d\Gamma^R . \tag{3.7}$$

The virtual corrections $d\Gamma^V$ consist of the vertex correction, wave-function corrections and self–energy corrections. All these types of corrections contain ultraviolet divergences that have to be regulated and canceled out after renormalization of the fields, vertices and coupling constants. Likewise, the real gluon corrections $d\Gamma^R$ have infrared and collinear divergences, which should be regulated as in the case of virtual corrections.

The ultraviolet divergences in virtual gluon corrections appear because the integration region of the internal momentum of the virtual particle goes to infinity. There have been many regularization and renormalization schemes. In this work, we employ the dimensional regularization and $\overline{MS}$ renormalization scheme. Dimensional regularization is better suited to regularize gauge theories because it is compatible with gauge invariance, as long as no chiral fermions are present. The main idea of the scheme is to change the number of space–time dimensions in the loop phase space integrals formally from 4 to $n = 4 + 2\varepsilon$. The singularities are extracted in terms of $\frac{1}{\varepsilon}$ and $\frac{1}{\varepsilon^2}$. In Section 3.3.1 and Section 3.3.2 we provide the explicit procedure to calculate the virtual and real corrections using dimensional regularization.

### 3.3.1 Virtual Gluon Corrections

First we calculate the renormalized one–loop corrections to the decay width, which are called virtual corrections. Expressed in terms of phase space variables and the amplitude $\mathcal{M}^V$, the contribution to the decay width of the virtual corrections reads

$$\begin{aligned} d\Gamma^V &= \frac{1}{2m_b}\frac{d^{(n-1)}\vec{p_e}}{(2\pi)^{n-1}2\,E_e}\frac{d^{(n-1)}\vec{p_\nu}}{(2\pi)^{n-1}2\,E_\nu}\frac{d^{(n-1)}\vec{P}}{(2\pi)^{n-1}2\,P^0}\times \\ &\quad (2\pi)^n\,\delta^{(n)}(p_b-P-p_e-p_\nu)\;<2\mathrm{Re}(\mathcal{M}^{Born^*}\mathcal{M}^V)> \\ &= \frac{1}{2\,m_b}\frac{1}{(2\pi)^5}\,d\mathcal{R}_3^{(4)}(\,p_b\,;\,P,\,p_e,\,p_\nu\,)\;<2\mathrm{Re}(\mathcal{M}^{Born^*}\mathcal{M}^V)>, \end{aligned} \tag{3.8}$$

where

$$d\mathcal{R}_i^{(n)}(\,Q\,;\,q_1,\,q_2,\,\cdots,\,q_i\,)\equiv\delta^{(n)}(Q-\sum_{j=1}^{i}q_j)\prod_{j=1}^{i}\frac{d^{(n-1)}q_j}{2\,q_j^0}\,. \tag{3.9}$$

The analysis of phase space is described in Appendix C.
The amplitude $\mathcal{M}^V$ which includes virtual corrections is

$$\mathcal{M}^V=\frac{G_F}{\sqrt{2}}\,V_{ub}\,\bar{u}(p_u)\Gamma^\mu_{REN}(y)u(p_b)\;\bar{u}(p_e)\gamma_\mu(1-\gamma_5)v(p_\nu)\,, \tag{3.10}$$

with $y\equiv\frac{W^2}{m_b^2}=\frac{(p_b-p_u)^2}{m_b^2}$ when $p_g=0$. The renormalized vertex $\Gamma^\mu_{REN}$ receives contributions from the self–energy correction, wave–function renormalization, and the vertex correction.

Both of the self–energy and wave–function renormalization contributions yield a factor of $\delta Z_M$, $-\frac{1}{2}\delta Z_M$ respectively, where $Z_M$ is the field renormalization constant for the field of the particle with mass $M$. Hence, the full renormalized vertex is expressed as

$$\Gamma^\mu_{REN}(y)=\frac{1}{2}(\delta Z_{m_b}+\delta Z_{m_u})\gamma^\mu(1-\gamma_5)+\Gamma^\mu_{vertex}(y)\,. \tag{3.11}$$

The self–energy correction and wave–function renormalization of a particle with mass $M$ and momentum $p$ is obtained from calculating $\Sigma_M$, which is depicted in Figure 3.4. In an arbitrary covariant gauge with gauge parameter $\xi$, the self–energy $\Sigma_M$ in $n$–dimension reads

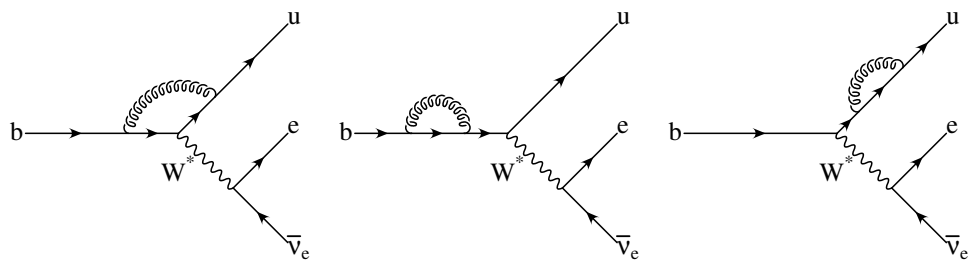


Figure 3.3: Feynman diagrams for the virtual corrections. The first diagram is the vertex correction, and the last two are quark self–energies.

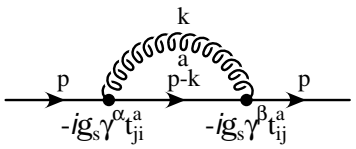


Figure 3.4: Feynman diagram for the self–energy $\Sigma_M$ of a particle with mass $M$.

$$\Sigma_M = -ig_s^2 \int \frac{d^n k}{(2\pi)^n} \left[ g_{\alpha\beta} - \xi \frac{k_\alpha k_\beta}{k^2} \right] t^a_{ji} \frac{1}{k^2} \frac{\gamma^\alpha (\not{p} - \not{k} + M) \gamma^\beta}{(p-k)^2 - M^2} t^a_{ij} \,, \qquad (3.12)$$

where $t^a_{ij} = \frac{\lambda^a_{ij}}{2}$ and $\sum_{a,i} t^a_{ji} t^a_{ij} = \frac{4}{3}$.
After Feynman parameterization, we obtain

$$\begin{aligned} \Sigma_M(p) = & \\ & \frac{4}{3} g_s^2 \frac{\Gamma[2 - n/2]}{(4\pi)^{n/2}} \int_0^1 dx \left\{ \frac{\xi(4-n) x^2 (1-x) p^2 \not{p}}{\Delta^{3-n/2}} \right. \\ & \left. + \frac{(2 - n + \xi)\not{p} - (2 - n - \xi) x \not{p} + (n - \xi) M - \xi(1-x)\not{p}}{\Delta^{2-n/2}} \right\}, \end{aligned} \qquad (3.13)$$

where $\Delta \equiv xM^2 - x(1-x)p^2$. We integrate Eq.(3.13) over $x$ and replacing $n = 4 + 2\varepsilon$, and obtain

$$
\begin{aligned}
&\Sigma_M(p) = \\
&\quad \frac{4}{3}\, g_s^2\, \frac{\Gamma[-\varepsilon]}{(4\pi)^{2+\varepsilon}} \left\{ \big(2\xi + 2 + 2\varepsilon\big)\, \not{p}\, \frac{M^{2\varepsilon}}{2+\varepsilon}\, {}_2F_1[-\varepsilon,\, 1;\, 3+\varepsilon;\, \frac{p^2}{M^2}] \right. \\
&\quad + \big((\xi - 2 - 2\varepsilon)\not{p} + (4 + 2\varepsilon - \xi) M - \xi \not{p}\big)\, \frac{M^{2\varepsilon}}{1+\varepsilon}\, {}_2F_1[-\varepsilon,\, 1;\, 2+\varepsilon;\, \frac{p^2}{M^2}] \\
&\quad - 2\xi\varepsilon\, \not{p}^3\, \frac{M^{2\varepsilon-2}}{2+\varepsilon}\, {}_2F_1[1-\varepsilon,\, 1;\, 3+\varepsilon;\, \frac{p^2}{M^2}] \\
&\quad \left. + 2\xi\varepsilon\, \not{p}^3\, \frac{M^{2\varepsilon-2}}{3+\varepsilon}\, {}_2F_1[1-\varepsilon,\, 1;\, 4+\varepsilon;\, \frac{p^2}{M^2} \right\}. \qquad (3.14)
\end{aligned}
$$

The field renormalization constant $\delta Z_M$ of the particle with mass $M$ is obtained as

$$
\begin{aligned}
\delta Z_M &\equiv \left. \frac{\partial \Sigma_M(p)}{\partial \not{p}} \right|_{\not{p}=M} \\
&= \frac{4}{3} g_s^2 M^{2\varepsilon} \frac{\Gamma[-\varepsilon]}{(4\pi)^{2+\varepsilon}} \left(-3 + 4\varepsilon - 8\varepsilon^2 + \mathcal{O}(\varepsilon^3)\right). \qquad (3.15)
\end{aligned}
$$

The result turns out to be independent of the gauge parameter $\xi$ as mentioned in [2]. The first term on R.H.S. in Eq.(3.11) reads

$$
\begin{aligned}
&\frac{1}{2}\big(\delta Z_{m_b} + \delta Z_{m_u}\big)\, \gamma^\mu (1 - \gamma_5) = \\
&\quad g_s^2\, \frac{m_b^{2\varepsilon}}{3}\, \frac{\Gamma[1-\varepsilon]}{2^{2\varepsilon}\pi^{2+\varepsilon}} \left\{ \frac{3}{8\varepsilon} - \frac{1}{2} + \varepsilon + \mathcal{O}(\varepsilon^2) \right\} \gamma^\mu (1 - \gamma_5)\,. \qquad (3.16)
\end{aligned}
$$

The one–loop vertex correction is depicted in Figure 3.5, and the formula $\Gamma^\mu_{vertex}[p_b, p_u]$ reads

$$
\begin{aligned}
&\Gamma^\mu_{vertex}[p_b, p_u] = \\
&\quad -i g_s^2 \int \frac{d^n k}{(2\pi)^n} \left[ g_{\alpha\beta} - \xi \frac{k_\alpha k_\beta}{k^2} \right] \times \\
&\quad \left[ t^a_{ij}\, \frac{\gamma^\alpha (\not{p}_u - \not{k}) \gamma^\mu (1 - \gamma_5) (\not{p}_b - \not{k} + m_b)\, \gamma^\beta}{k^2 \left((p_b - k)^2 - m_b^2\right) \big(p_u - k\big)^2}\, t^a_{jl} \right]. \qquad (3.17)
\end{aligned}
$$

Since $\Gamma^\mu_{REN}$ is directly connected to the measurable quantity $d\Gamma$, it is gauge–independent, and we choose the Feynman gauge. The $\gamma_5$ matrix is not well defined

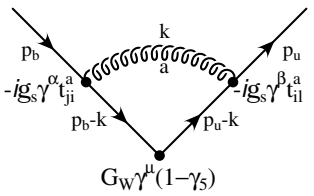


Figure 3.5: Feynman diagram for the one–loop vertex correction. $G_W \equiv -ig_w\frac{V_{ub}}{2\sqrt{2}}$ with the weak coupling constant $g_w$ and the *CKM* matrix element $V_{ub}$ for the $b \to u$ transition.

in $n$ dimensions. The anti–commutation relation $\{\gamma^\mu, \gamma_5\} = 0$ produces the ambiguity, and one cannot simply apply the anti–commutation relation in general $n$ dimensions. There have been several prescriptions to prevent the ambiguity of $\gamma_5$ [57, 58, 59]. We employ the Breitenlohner–Maison (BM) scheme, and a more detailed explanation is found in Appendix D.

After applying the on–shell evaluations $p_b^2 = m_b^2$ and $p_u^2 = 0$ in Eq.(3.17), and summing and averaging it over the color, we obtain

$$\Gamma^\mu_{vertex}[p_b, p_u] = -ig_s^2\frac{4}{3}\int\frac{d^nk}{(2\pi)^n}\,\frac{\gamma^\alpha(\not{p}_u - \not{k})\gamma^\mu(1-\gamma_5)(\not{p}_b - \not{k} + m_b)\gamma_\alpha}{k^2\big((p_b-k)^2 - m_b^2\big)(p_u-k)^2}\,. \tag{3.18}$$

We introduce two Feynman parameters $v$ and $w$ and set $y = \frac{(p_b-p_u)^2}{m_b^2}$. We write $\Gamma^\mu_{vertex}[p_b, p_u]$ as $\Gamma^\mu_{vertex}[y]$ making use of the kinematic variable $y$. After Feynman parameterization of Eq.(3.18), the $\Gamma^\mu_{vertex}[y]$ reads

$$\begin{aligned}\Gamma^\mu_{vertex}[y] = {} & g_s^2\frac{8}{3}\,m_b^{n-4}\,\frac{\Gamma[3-n/2]}{(4\pi)^{n/2}}\int_0^1 dw\,w\int_0^1 dv\,\frac{1}{\big(w^2(1-v)(1-yv)\big)^{2-n/2}}\;\times \\ & \Bigg[\Big\{\frac{1}{w(1-yv)} - \frac{(1-y)(1-w)}{w^2(1-v)(1-yv)} - \frac{(n-2)(n-3)}{n-4}\Big\}\gamma^\mu(1-\gamma_5) \\ & + (n-2)\frac{1-v}{1-yv}\,\frac{p_b^\mu}{m_b}\,(1+\gamma_5) + \frac{(n-2)wv-2}{w(1-yv)}\,\frac{p_u^\mu}{m_b}\,(1+\gamma_5)\Bigg],\end{aligned} \tag{3.19}$$

and after integrating Eq.(3.19) over $w$ and $v$ and applying $n = 4 + 2\varepsilon$, we obtain

$$\Gamma^{\mu}_{vertex}[y] = g_s^2 \frac{16}{3} m_b^{2\varepsilon} \frac{\Gamma[1-\varepsilon]}{(4\pi)^{2+\varepsilon}} \Bigg\{ \mathcal{A}_{vertex}(y)\gamma^{\mu}(1-\gamma_5) + \mathcal{B}_{vertex}(y)\frac{p_b^{\mu}}{m_b}(1+\gamma_5) + \mathcal{C}_{vertex}(y)\frac{p_u^{\mu}}{m_b}(1+\gamma_5) \Bigg\}, \quad (3.20)$$

$$\mathcal{A}_{vertex}(y) = \frac{1}{(1+2\varepsilon)(2+2\varepsilon)}\, {}_2F_1[1-\varepsilon,\, 1;\, 2+\varepsilon;\, y] - \frac{1+2\varepsilon}{2\varepsilon(2+2\varepsilon)}\, {}_2F_1[-\varepsilon,\, 1;\, 2+\varepsilon;\, y] - \frac{1-\varepsilon}{(1+2\varepsilon)(2\varepsilon)^2}\, {}_2F_1[1-\varepsilon,\, 1;\, 1+\varepsilon;\, y]\,, \quad (3.21)$$

$$\mathcal{B}_{vertex}(y) = \frac{1}{4+2\varepsilon}\, {}_2F_1[1-\varepsilon,\, 1;\, 3+\varepsilon;\, y]\,, \quad (3.22)$$

$$\mathcal{C}_{vertex}(y) = \frac{2}{(4+2\varepsilon)(2+2\varepsilon)}\, {}_2F_1[1-\varepsilon,\, 2;\, 3+\varepsilon;\, y] - \frac{2}{(2+2\varepsilon)(1+2\varepsilon)}\, {}_2F_1[1-\varepsilon,\, 1;\, 2+\varepsilon;\, y]\,. \quad (3.23)$$

We now take the $\varepsilon \to 0$ limits of the hyper geometric functions in Eqs.(3.21)—(3.23) and where the hyper geometric function has no finite limit, we need to expand it in powers of $\varepsilon$. Some useful identities for the hyper geometric functions are described in Appendix B. After taking the limit $\varepsilon \to 0$ of the hyper geometric functions and expanding the coefficients in powers of $\varepsilon$, $\mathcal{A}_{vertex}(y)$, $\mathcal{B}_{vertex}(y)$ and $\mathcal{C}_{vertex}(y)$ read

$$\mathcal{A}_{vertex}(y) = -\frac{1}{4\varepsilon^2} + \frac{1}{4\varepsilon} - \frac{\ln(1-y)}{2\varepsilon} - 1 + \frac{3}{4}\ln(1-y) - \frac{1}{2}\ln^2(1-y) - \frac{\ln(1-y)}{4y} - \frac{\mathrm{Li}_2(y)}{2}\,, \quad (3.24)$$

$$\mathcal{B}_{vertex}(y) = \frac{1}{2}\left\{ \frac{1}{y} - \frac{\ln(1-y)}{y} + \frac{\ln(1-y)}{y^2} \right\}, \quad (3.25)$$

$$\mathcal{C}_{vertex}(y) = \frac{\ln(1-y)}{y} - \frac{1}{2y} - \frac{\ln(1-y)}{2y^2}\,. \quad (3.26)$$

The self–energy, wave–function and vertex corrections are added together, and the resulting renormalized vertex reads

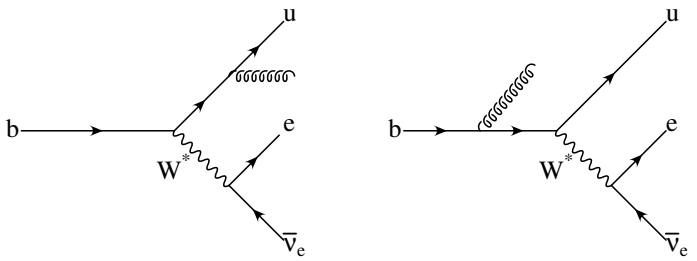


Figure 3.6: Feynman diagrams for the real corrections.

$$\Gamma^{\mu}_{REN}(y) = \alpha_s\, m_b^{2\varepsilon}\, \frac{4}{3}\, \frac{\Gamma(1-\varepsilon)}{2^{2\varepsilon}\,\pi^{(1+\varepsilon)}} \times \left( \mathcal{A}(y)\,\gamma^{\mu}(1-\gamma_5) + \mathcal{B}(y)\,\frac{p_b^{\mu}}{m_b}(1+\gamma_5) + \mathcal{C}(y)\,\frac{p_u^{\mu}}{m_b}(1+\gamma_5) \right), \quad (3.27)$$

$$\mathcal{A}(y) = -\frac{1}{4\varepsilon^2} + \frac{1}{4\varepsilon} - \frac{\ln(1-y)}{2\varepsilon} - 1 + \frac{3}{4}\,\ln(1-y) - \frac{1}{2}\,\ln^2(1-y) - \frac{1}{4}\,\frac{\ln(1-y)}{y} - \frac{1}{2}\,\mathrm{Li}_2(y) + \mathcal{O}(\varepsilon)\,, \quad (3.28)$$

$$\mathcal{B}(y) = \frac{1}{2}\left( \frac{1}{y} - \frac{\ln(1-y)}{y} + \frac{\ln(1-y)}{y^2} \right), \quad (3.29)$$

$$\mathcal{C}(y) = \frac{\ln(1-y)}{y} - \frac{1}{2y} - \frac{1}{2}\,\frac{\ln(1-y)}{y^2}\,, \quad (3.30)$$

which coincide with the results in [1, 2].

### 3.3.2 Real Gluon Corrections

Feynman diagrams of the real gluon corrections are displayed in Figure 3.6. The amplitude of the real gluon corrections $\mathcal{M}^R$ is

$$\mathcal{M}^R = \frac{G_F}{\sqrt{2}}\, V_{ub} \left[\, \bar{u}(\,p_u)\,\mathrm{S}^{real}_{(1)}\,u(\,p_b) \,+ \bar{u}(\,p_u)\,\mathrm{S}^{real}_{(2)}\,u(\,p_b)\,\right] \times \left[\, \bar{u}(\,p_e)\gamma_{\mu}(1-\gamma_5)\,v(\,p_{\nu})\,\right], \quad (3.31)$$

$$\mathrm{S}^{real}_{(1)} = \gamma^{\mu}(1-\gamma_5)\,\frac{i}{(\not{p}_b \,-\, \not{p}_g \,-m_b)}\, i g_s \frac{\lambda_a}{2}\, \not{\epsilon}^{*}(\lambda)\,, \quad (3.32)$$

$$\mathrm{S}^{real}_{(2)} \;=\; i g_s \frac{\lambda_a}{2}\, \not{\epsilon}^{*}(\lambda)\, \frac{i}{(\not{p}_u \;+ \not{p}_g \;- m_u)}\, \gamma^{\mu}(1-\gamma_5)\,. \tag{3.33}$$

We use the dimensional regularization scheme and define $p_g^2 = 0$ and $n = 4 + 2\varepsilon$. Singularities appear in the form of $\frac{1}{\varepsilon}$ and $\frac{1}{\varepsilon^2}$, when $z$ and $\varepsilon$ approach 0. The singularities appearing when $z \to 0$ are both collinear singularities and infrared singularities. By definition, $z \equiv \frac{P^2}{m_b^2} = \frac{(p_u+p_g)^2}{m_b^2}$. Collinear singularities appear when $p_u \cdot p_g = 0$, and infrared singularities when $p_g = 0$, and for both cases $P^2 = 0$, and therefore $z = 0$.

We square the amplitude in general $n$–dimension, replacing $n \to 4 + 2\varepsilon$, and the squared amplitude is expanded in powers of $\varepsilon$. Special care should be paid to the $\gamma_5$ matrix when we consider it in $n$ dimensions. The anti–commutation relation of $\gamma_5$ is not allowed in general $n$ dimensions. We adopt the Breitenlohner–Maison (BM) scheme (an explanation is found in Appendix D). The BM–scheme is summarized by two principle rules. One is that one should not commute $\gamma_5$ with other $\gamma$ matrices, i.e. $\{\,\gamma_\mu,\,\gamma_5\,\} \neq 0$, and the other is that the trace of $\gamma_5\gamma_\alpha\gamma_\beta\gamma_\gamma\gamma_\sigma$ is expressed with the conventional anti–symmetric metric $\varepsilon$–tensor, i.e. $\mathrm{Tr}[\gamma_5\gamma_\alpha\gamma_\beta\gamma_\gamma\gamma_\sigma] = i4\varepsilon_{\alpha\beta\gamma\sigma}$. To avoid the anti–commutation relation of $\gamma_5$ one does not contract two $\gamma$ matrices with a $\gamma_5$ matrix between them.

The result for the squared amplitude is

$$\overline{|\mathcal{M}^R|^2} \;=\; \frac{G_F^2}{2}\,|V_{ub}|^2\,\alpha_s\,\frac{8\pi}{3}\left[\,\mathcal{M}^{R\,0} + \mathcal{M}^{R\,1}\,\varepsilon + \mathcal{M}^{R\,2}\,\varepsilon^2 + \mathcal{O}(\varepsilon^3)\right], \tag{3.34}$$

$$\mathcal{M}^{R\,0} \;=\; 256\left[\frac{\mathcal{D}^0_{-2}}{(\,p_b\cdot p_g)^2} \;-\; \frac{\mathcal{D}^0_{-1}}{(\,p_b\cdot p_g)} \;+\; \mathcal{D}^0{}_0 \;+\; \mathcal{D}^0{}_1\,(\,p_b\cdot p_g)\right], \tag{3.35}$$

$$\mathcal{D}^0_{-2} \;=\; m_b^2\,(\,p_u\cdot p_e)\big(\,(\,p_g\cdot p_\nu) - (\,p_b\cdot p_\nu)\,\big)\,, \tag{3.36}$$

$$\begin{aligned}\mathcal{D}^0_{-1} \;=\;& \frac{1}{(\,p_u\cdot p_g)}\,\times \\ & \Big(\,(\,p_b\cdot p_u)(\,p_g\cdot p_e)(\,p_b\cdot p_\nu) + 2(\,p_b\cdot p_u)(\,p_u\cdot p_e)(\,p_b\cdot p_\nu) \\ & -\,(\,p_b\cdot p_u)(\,p_u\cdot p_e)(\,p_g\cdot p_\nu) + (\,p_u\cdot p_g)(\,p_u\cdot p_e)(\,p_g\cdot p_\nu) \\ & -\,(\,p_u\cdot p_g)(\,p_b\cdot p_e)(\,p_b\cdot p_\nu) - (\,p_u\cdot p_g)(\,p_u\cdot p_e)(\,p_b\cdot p_\nu)\Big)\,,\end{aligned} \tag{3.37}$$

$$\mathcal{D}^0{}_0 \;=\; (\,p_b\cdot p_\nu)\big(\,(\,p_g\cdot p_e) + (\,p_u\cdot p_e)\,\big) + (\,p_u\cdot p_e)(\,p_u\cdot p_\nu)\,, \tag{3.38}$$

$$\mathcal{D}^0{}_1 \;=\; 0\,, \tag{3.39}$$

$$\mathcal{M}^{R\,1} = 128\left[\frac{\mathcal{D}^1_{-2}}{(p_b\cdot p_g)^2}+\frac{\mathcal{D}^1_{-1}}{(p_b\cdot p_g)}+\mathcal{D}^1{}_0+\mathcal{D}^1{}_1\,(p_b\cdot p_g)\right], \tag{3.40}$$

$$\begin{aligned}\mathcal{D}^1_{-2} = m_b^2\Big(&(p_g\cdot p_u)(p_e\cdot p_\nu)-(p_b\cdot p_u)(p_e\cdot p_\nu)\\&+3(p_u\cdot p_e)(p_g\cdot p_\nu)-3(p_u\cdot p_e)(p_b\cdot p_\nu)\\&+3(p_b\cdot p_e)(p_u\cdot p_\nu)-3(p_g\cdot p_e)(p_u\cdot p_\nu)\Big),\end{aligned} \tag{3.41}$$

$$\begin{aligned}\mathcal{D}^1_{-1} = {}&(p_u\cdot p_g)(p_e\cdot p_\nu)-2(p_b\cdot p_u)(p_e\cdot p_\nu)-m_b^2(p_e\cdot p_\nu)\\&-(p_g\cdot p_e)(p_b\cdot p_\nu)-3(p_u\cdot p_e)(p_b\cdot p_\nu)+5(p_u\cdot p_e)(p_g\cdot p_\nu)\\&-(p_b\cdot p_e)(p_g\cdot p_\nu)+3(p_b\cdot p_e)(p_u\cdot p_\nu)-3(p_g\cdot p_e)(p_u\cdot p_\nu)\\&+\frac{1}{(p_u\cdot p_g)}\times\\&\Big(6(p_b\cdot p_u)(p_u\cdot p_e)(p_b\cdot p_\nu)-3(p_b\cdot p_u)(p_u\cdot p_e)(p_g\cdot p_\nu)\\&-3(p_b\cdot p_u)(p_b\cdot p_e)(p_g\cdot p_\nu)-6(p_b\cdot p_u)(p_b\cdot p_e)(p_u\cdot p_\nu)\\&+2(p_b\cdot p_u)(p_g\cdot p_e)(p_g\cdot p_\nu)+3(p_b\cdot p_u)(p_g\cdot p_e)(p_u\cdot p_\nu)\\&+2(p_e\cdot p_\nu)(p_b\cdot p_u)^2+3(p_b\cdot p_u)(p_g\cdot p_e)(p_b\cdot p_\nu)\Big),\end{aligned} \tag{3.42}$$

$$\begin{aligned}\mathcal{D}^1{}_0 = \frac{1}{(p_u\cdot p_g)}\Big(&2(p_b\cdot p_u)(p_e\cdot p_\nu)+5(p_g\cdot p_e)(p_b\cdot p_\nu)\\&+3(p_u\cdot p_e)(p_b\cdot p_\nu)-(p_b\cdot p_e)(p_g\cdot p_\nu)\\&-(p_u\cdot p_e)(p_g\cdot p_\nu)-3(p_b\cdot p_e)(p_u\cdot p_\nu)\\&-(p_g\cdot p_e)(p_u\cdot p_\nu)\Big),\end{aligned} \tag{3.43}$$

$$\mathcal{D}^1{}_1 = \frac{(p_e\cdot p_\nu)}{(p_u\cdot p_g)}, \tag{3.44}$$

$$\mathcal{M}^{R\,2} = 128\left[\frac{\mathcal{D}^2_{-2}}{(p_b\cdot p_g)^2}+\frac{\mathcal{D}^2_{-1}}{(p_b\cdot p_g)}+\mathcal{D}^2{}_0+\mathcal{D}^2{}_1(p_b\cdot p_g)\right], \tag{3.45}$$

$$\begin{aligned}\mathcal{D}^2_{-2} = 2\,m_b^2\Big(&(p_u\cdot p_e)(p_g\cdot p_\nu)-(p_u\cdot p_e)(p_b\cdot p_\nu)\\&+(p_b\cdot p_e)(p_u\cdot p_\nu)-(p_g\cdot p_e)(p_u\cdot p_\nu)\Big),\end{aligned} \tag{3.46}$$

$$
\begin{aligned}
\mathcal{D}^2_{-1} &= \frac{1}{(p_u\cdot p_g)}\times \\
&\Big((p_u\cdot p_g)^2(p_e\cdot p_\nu)+5(p_u\cdot p_g)(p_u\cdot p_e)(p_g\cdot p_\nu) \\
&\quad -5(p_u\cdot p_g)(p_g\cdot p_e)(p_u\cdot p_\nu)-2(p_b\cdot p_u)(p_u\cdot p_e)(p_g\cdot p_\nu) \\
&\quad +2(p_b\cdot p_u)(p_g\cdot p_e)(p_u\cdot p_\nu) \\
&\quad +(p_b\cdot p_\nu)\Big((p_g\cdot p_e)+2(p_u\cdot p_e)\Big)\Big(2(p_b\cdot p_u)-(p_u\cdot p_g)\Big) \\
&\quad -(p_b\cdot p_e)\Big(2(p_b\cdot p_u)-(p_u\cdot p_g)\Big)\Big((p_g\cdot p_\nu)+2(p_u\cdot p_g)\Big)\Big)\,, \qquad (3.47)
\end{aligned}
$$

$$
\begin{aligned}
\mathcal{D}^2{}_0 &= \frac{1}{(p_u\cdot p_g)}\Big((p_b\cdot p_\nu)\Big(5(p_g\cdot p_e)+2(p_u\cdot p_e)\Big) \\
&\qquad -(p_u\cdot p_e)(p_g\cdot p_\nu)-2(p_u\cdot p_g)(p_e\cdot p_\nu) \\
&\qquad +(p_g\cdot p_e)(p_u\cdot p_\nu) \\
&\qquad -(p_b\cdot p_e)\Big(5(p_g\cdot p_\nu)+2(p_u\cdot p_\nu)\Big)\Big)\,, \qquad (3.48)
\end{aligned}
$$

$$
\mathcal{D}^2{}_1 = \frac{(p_e\cdot p_\nu)}{(p_u\cdot p_g)}\,. \qquad (3.49)
$$

The leptonic tensor $L_{\mu\nu}$ is defined as

$$
L_{\mu\nu} = Tr[\bar{u}(p_e)\gamma_\mu(1-\gamma_5)v(p_\nu)\,\bar{v}(p_\nu)\gamma_\nu(1-\gamma_5)u(p_e)]\,. \qquad (3.50)
$$

For calculational convenience, we define a new leptonic tensor as in [3]

$$
\ell^{\mu\nu} \equiv p_e^\mu\, p_\nu^\nu\,, \qquad (3.51)
$$

and the corresponding hadronic tensor $h^j{}_i{}^{\mu\nu}$ for each $\mathcal{D}^j{}_i$ is defined as

$$
\mathcal{D}^j{}_i = h^j{}_i{}^{\mu\nu}\,\ell_{\mu\nu}\,, \qquad (3.52)
$$

and the specific expressions of $h^j{}_i{}^{\mu\nu}$ are in Appendix E.

The real correction contributions to the decay rate $d\Gamma^R$ are expressed as

$$
\begin{aligned}
d\Gamma^R &= \frac{1}{2\,p_b^0}\,\frac{1}{(2\,\pi)^{2n-3}}\,\frac{d^{n-1}\vec{p_e}}{2\,p_e^0}\,\frac{d^{n-1}\vec{p_\nu}}{2\,p_\nu^0}\,\frac{d^{n-1}\vec{P}}{2\,P^0}\,\delta^{(n)}(\,p_b - P - p_e - p_\nu\,)\,\times \\
&\quad \frac{1}{(2\,\pi)^{n-1}}\,p_b^2 d\,z\,\frac{d^{n-1}\vec{p_u}}{2p_u^0}\,\frac{d^{n-1}\vec{p_g}}{2p_g^0}\,\delta^{(n)}(\,P - p_u - p_g\,)\,\overline{|\mathcal{M}^R|^2} \\
&= \frac{1}{2\,p_b^0}\,\frac{1}{(2\,\pi)^{2n-3}}\,d\mathcal{R}_3^{(n)}(\,p_b;\,P,\,p_e,\,p_\nu\,)\,\times \\
&\quad \frac{1}{(2\,\pi)^{n-1}}\,p_b^2 dz\,d\mathcal{R}_2^{(n)}(\,P;\,p_u,\,p_g\,)\,\overline{|\mathcal{M}^R|^2}\,. \qquad (3.53)
\end{aligned}
$$

We introduce a new hadronic tensor $\mathcal{H}^{\mu\nu}$:

$$
\mathcal{H}^{\mu\nu} = \mathcal{A}\,g^{\mu\nu} + \mathcal{B}\,p_b^\mu p_b^\nu + \mathcal{C}\,P^\mu P^\nu + \mathcal{D}\,p_b^\mu P^\nu + \mathcal{E}\,P^\mu p_b^\nu\,, \qquad (3.54)
$$

which is defined as

$$
\mathcal{H}^{\mu\nu}\,\ell_{\mu\nu} \equiv d\mathcal{R}_2^{(n)}(\,P;\,p_u,\,p_g\,)\,\overline{|\mathcal{M}^R|^2}\,. \qquad (3.55)
$$

The squared amplitude $\overline{|\mathcal{M}^R|^2}$ is decomposed with the corresponding hadronic tensor $h^{\mu\nu}$ like

$$
\overline{|\mathcal{M}^R|^2} = h^{\mu\nu}\,\ell_{\mu\nu}\,, \qquad (3.56)
$$

and we obtain

$$
\begin{aligned}
\mathcal{H}^{\mu\nu}\,\ell_{\mu\nu} &= d\mathcal{R}_2^{(n)}(\,P,\,p_u,\,p_g\,)\,\overline{|\mathcal{M}^R|^2} \\
&= d\mathcal{R}_2^{(n)}(\,P;\,p_u,\,p_g\,)\,h^{\mu\nu}\,\ell_{\mu\nu}\,. \qquad (3.57)
\end{aligned}
$$

Eq.(3.57) says also

$$
\mathcal{H}^{\mu\nu} = d\mathcal{R}_2^{(n)}(\,P;\,p_u,\,p_g\,)\,h^{\mu\nu}\,. \qquad (3.58)
$$

We introduce projection operators ${}^i\mathcal{P}^{\mu\nu}$

$$
\begin{aligned}
{}^1\mathcal{P}^{\mu\nu} &= g^{\mu\nu} \\
{}^2\mathcal{P}^{\mu\nu} &= p_b^\mu p_b^\nu \\
{}^3\mathcal{P}^{\mu\nu} &= P^\mu P^\nu \\
{}^4\mathcal{P}^{\mu\nu} &= p_b^\mu P^\nu \\
{}^5\mathcal{P}^{\mu\nu} &= P^\mu p_b^\nu \,. \qquad (3.59)
\end{aligned}
$$

Applying the projection operators onto Eq.(3.58), we obtain

$$
{}^i\mathcal{P}_{\mu\nu}\,\mathcal{H}^{\mu\nu} = \mathcal{S}^i \,, \qquad (3.60)
$$

where the variables $\mathcal{S}^i$ are defined as

$$
\mathcal{S}^i \equiv d\mathcal{R}_2^{(n)}(\, P;\, p_u,\, p_g\,)\,{}^i\mathcal{P}_{\mu\nu}\,h^{\mu\nu} \,. \qquad (3.61)
$$

The coefficients $\mathcal{A}$, $\mathcal{B}$, $\mathcal{C}$, $\mathcal{D}$ and $\mathcal{E}$ are expressed in terms of the $\mathcal{S}^i$

$$
\begin{aligned}
\mathcal{A} &= \frac{1}{2\,(1+\varepsilon)}\,\mathcal{S}^1 \\
&\quad + \frac{1}{2\,(1+\varepsilon)}\,\frac{1}{m_b^2}\,\frac{z}{\mathcal{P}_3(y,z)^2}\,\mathcal{S}^2 \;+\; \frac{1}{2\,(1+\varepsilon)}\,\frac{1}{m_b^2}\,\frac{1}{\mathcal{P}_3(y,z)^2}\,\mathcal{S}^3 \\
&\quad - \frac{1}{2\,(1+\varepsilon)}\,\frac{1}{m_b^2}\,\frac{\mathcal{P}_0(y,z)}{\mathcal{P}_3(y,z)^2}\,\mathcal{S}^4 \;-\; \frac{1}{2\,(1+\varepsilon)}\,\frac{1}{m_b^2}\,\frac{\mathcal{P}_0(y,z)}{\mathcal{P}_3(y,z)^2}\,\mathcal{S}^5 \,,
\end{aligned}
$$

$$
\begin{aligned}
\mathcal{B} &= \frac{1}{2\,(1+\varepsilon)}\,\frac{1}{m_b^2}\,\frac{z}{\mathcal{P}_3(y,z)^2}\,\mathcal{S}^1 + \frac{(3+2\varepsilon)}{2\,(1+\varepsilon)}\,\frac{1}{m_b^4}\,\frac{z^2}{\mathcal{P}(y,z)^4}\,\mathcal{S}^2 \\
&\quad + \frac{1}{4\,(1+\varepsilon)}\,\frac{1}{m_b^4}\,\frac{1}{\mathcal{P}_3(y,z)^4}\;\times \\
&\quad \Big(1+y^2+4z+z^2-2y(1+z)+\varepsilon(1-y+z)^2\Big)\,\mathcal{S}^3 \\
&\quad - \frac{(3+2\varepsilon)}{2\,(1+\varepsilon)}\,\frac{1}{m_b^4}\,\frac{z\,\mathcal{P}_0(y,z)}{\mathcal{P}_3(y,z)^4}\,\mathcal{S}^4 \;-\; \frac{(3+2\varepsilon)}{2\,(1+\varepsilon)}\,\frac{1}{m_b^4}\,\frac{z\,\mathcal{P}_0(y,z)}{\mathcal{P}_3(y,z)^4}\,\mathcal{S}^5 \,,
\end{aligned}
$$

$$
\begin{aligned}
\mathcal{C} &= \frac{1}{2\,(1+\varepsilon)}\,\frac{1}{m_b^2}\,\frac{1}{\mathcal{P}_3(y,z)^2}\,\mathcal{S}^1 \\
&+ \frac{1}{4\,(1+\varepsilon)}\,\frac{1}{m_b^4}\,\frac{1}{\mathcal{P}_3(y,z)^4}\,\times \\
&\quad \Big(1+y^2+4z+z^2-2y(1+z)+\varepsilon(1-y+z)^2\Big)\,\mathcal{S}^2 \\
&+ \frac{(3+2\varepsilon)}{2(1+\varepsilon)}\,\frac{1}{m_b^4}\,\frac{1}{\mathcal{P}_3(y,z)^4}\,\mathcal{S}^3 \;-\; \frac{(3+2\varepsilon)}{2(1+\varepsilon)}\,\frac{1}{m_b^4}\,\frac{\mathcal{P}_0(y,z)}{\mathcal{P}_3(y,z)^4}\,\mathcal{S}^4 \\
&- \frac{(3+2\varepsilon)}{2(1+\varepsilon)}\,\frac{1}{m_b^4}\,\frac{\mathcal{P}_0(y,z)}{\mathcal{P}_3(y,z)^4}\,\mathcal{S}^5\,,
\end{aligned}
$$

$$
\begin{aligned}
\mathcal{D} &= \frac{-1}{2\,(1+\varepsilon)}\,\frac{1}{m_b^2}\,\frac{\mathcal{P}_0(y,z)}{\mathcal{P}_3(y,z)^2}\,\mathcal{S}^1 \;-\; \frac{(3+2\varepsilon)}{2\,(1+\varepsilon)}\,\frac{1}{m_b^4}\,\frac{z\,\mathcal{P}_0(y,z)}{\mathcal{P}_3(y,z)^4}\,\mathcal{S}^2 \\
&- \frac{(3+2\varepsilon)}{2\,(1+\varepsilon)}\,\frac{1}{m_b^4}\,\frac{\mathcal{P}_0(y,z)}{\mathcal{P}_3(y,z)^4}\,\mathcal{S}^3 \\
&+ \frac{1}{8\,(1+\varepsilon)}\,\frac{1}{m_b^4}\,\frac{1}{\mathcal{P}_3(y,z)^4} \\
&\quad \Big((1-y)^2+(10-2y)z+z^2+8z\varepsilon\Big)\,\mathcal{S}^4 \\
&+ \frac{(3+2\varepsilon)}{2\,(1+\varepsilon)}\,\frac{1}{m_b^4}\,\frac{\mathcal{P}_0(y,z)^2}{\mathcal{P}_3(y,z)^4}\,\mathcal{S}^5\,,
\end{aligned}
$$

$$
\begin{aligned}
\mathcal{E} &= \frac{-1}{2\,(1+\varepsilon)}\,\frac{1}{m_b^2}\,\frac{\mathcal{P}_0(y,z)}{\mathcal{P}_3(y,z)^2}\,\mathcal{S}^1 \;-\; \frac{(3+2\varepsilon)}{2\,(1+\varepsilon)}\,\frac{1}{m_b^4}\,\frac{z\,\mathcal{P}_0(y,z)}{\mathcal{P}_3(y,z)^4}\,\mathcal{S}^2 \\
&- \frac{(3+2\varepsilon)}{2\,(1+\varepsilon)}\,\frac{1}{m_b^4}\,\frac{\mathcal{P}_0(y,z)}{\mathcal{P}_3(y,z)^4}\,\mathcal{S}^3 \;+\; \frac{(3+2\varepsilon)}{2\,(1+\varepsilon)}\,\frac{1}{m_b^4}\,\frac{\mathcal{P}_0(y,z)^2}{\mathcal{P}_3(y,z)^4}\,\mathcal{S}^4 \\
&+ \frac{1}{8\,(1+\varepsilon)}\,\frac{1}{m_b^4}\,\frac{1}{\mathcal{P}_3(y,z)^4}\,\times \\
&\quad \Big((1-y)^2+(10-2y)z+z^2+8z\varepsilon\Big)\,\mathcal{S}^5\,,
\end{aligned}
\tag{3.62}
$$

where the functions $\mathcal{P}_0(y,z)$ and $\mathcal{P}_3(y,z)$ are defined as

$$
\begin{aligned}
\mathcal{P}_0(y,z) &\equiv \frac{1-y+z}{2}\,, \\
\mathcal{P}_3(y,z) &\equiv \frac{\sqrt{1+y^2+z^2-2y-2z-2yz}}{2}\,.
\end{aligned}
\tag{3.63}
$$

We should pay attention to the scalar product $(\,p_b\cdot p_g\,)$ in calculating the $\mathcal{S}^i$. All other scalar products like $(\,p_u\cdot p_g\,)$ or $(\,p_u\cdot P\,)$ are expressed with the kinematic

variables $z$, $y$ and $x_e$ and are therefore independent of the integration variables $\vec{p_u}$ and $\vec{p_g}$. We can sort the integrand of the $\mathcal{S}^i$ in the order of $(\, p_b \cdot p_g \,)$ and define each order of integration as

$$\begin{aligned}
\mathcal{I}_{\,1} &\equiv d\mathcal{R}_2^{(n)}(\, P;\, p_u,\, p_g \,)(\, p_b \cdot p_g \,)\,, \\
\mathcal{I}_{\,0} &\equiv d\mathcal{R}_2^{(n)}(\, P;\, p_u,\, p_g \,)\,, \\
\mathcal{I}_{-1} &\equiv d\mathcal{R}_2^{(n)}(\, P;\, p_u,\, p_g \,)\frac{1}{(\, p_b \cdot p_g \,)}\,, \\
\mathcal{I}_{-2} &\equiv d\mathcal{R}_2^{(n)}(\, P;\, p_u,\, p_g \,)\,\frac{1}{(\, p_b \cdot p_g \,)^2}\,,
\end{aligned} \tag{3.64}$$

and the explicit formulas of the ${}^i\mathcal{S}$ are

$$\begin{aligned}
{}^1\mathcal{S} = \\
&128\left[(1+\varepsilon)^3\,\frac{1}{m_b^2}\,\frac{4}{z}\,\mathcal{I}_{\,1} - \,4\,(1+\varepsilon)^2\,\frac{1}{z}\left(1-y+z\,\varepsilon\right)\mathcal{I}_{\,0}\right. \\
&\quad + (1+\varepsilon)^2\,m_b^2\,\frac{1}{z}\left(2+2\,y^2-y\,(4+2\,z)+2\,z+z^2+\varepsilon\,z^2\right)\mathcal{I}_{-1} \\
&\quad \left. - (1+\varepsilon)^2\,m_b^4\,(1-y)\,\mathcal{I}_{-2}\right],
\end{aligned}$$

$$\begin{aligned}
{}^2\mathcal{S} = \\
&64\left[\,4\,(1+\varepsilon)\,\frac{1}{z}\left(2-z+\varepsilon\right)\mathcal{I}_{\,1}\right. \\
&\quad + 2\,m_b^2\,\frac{1}{z}\left(\,(1-y+z)\,(z-4)+\right. \\
&\qquad\qquad \left.(1-y+z)\,(z-2)\,\varepsilon-2\,z\,\varepsilon^2\right)\mathcal{I}_{\,0} \\
&\quad + m_b^4\,\frac{1}{z}\left(4\,(1-y+z)^2+\right. \\
&\qquad\qquad \left.\left\{\,2+2\,y^2+2\,z+z^2-2\,y\,(2+z)\,\right\}\varepsilon+z^2\,\varepsilon^2\right)\mathcal{I}_{-1} \\
&\quad \left. - m_b^6\left(2\,(1-y+z)+(1-y)\,\varepsilon\right)\mathcal{I}_{-2}\,\right],
\end{aligned}$$

$$
\begin{aligned}
{}^{3}\mathcal{S} = \\
& 64 \Bigg[ 4\,\varepsilon\,(1+\varepsilon)\mathcal{I}_{\ 1} \\
& \quad - 2\,(1+\varepsilon)\,m_b^2 \Big( 1 - y - z + 2\,z\,\varepsilon \Big) \mathcal{I}_{\ 0} \\
& \quad + (1+\varepsilon)\,m_b^4 \Big( 2 + 2\,y^2 + 2\,z - 2\,y\,(2+z) + (1+\varepsilon)\,z^2 \Big)\, \mathcal{I}_{-1} \\
& \quad - (1+\varepsilon)\,m_b^6\,(1-y)\,z\,\mathcal{I}_{-2} \Bigg],
\end{aligned}
$$

$$
\begin{aligned}
{}^{4}\mathcal{S} = \\
& 64 \Bigg[ 4\,\frac{1}{z} \Big( 1 - y - z + \{\, 3 - 3\,y - z \,\}\,\varepsilon + \{\, 3 - 3\,y + 2\,z \,\}\,\varepsilon^2 \Big) \mathcal{I}_{\ 1} \\
& \quad + 2\,m_b^2\,\frac{1}{z} \Big( -2 + 4\,y - 2\,y^2 + z^2 + \\
& \qquad \{\, (8+z)\,y - 4 - 4\,y^2 + 2\,z - z^2 \,\}\,\varepsilon + \\
& \qquad \{\, 2\,y(2+z) - 2 - 2\,y^2 - 3\,z - 5\,z^2 \,\}\,\varepsilon^2 \Big) \mathcal{I}_{\ 0} \\
& \quad + m_b^4\,\frac{1}{z} \Big( 2 - 6\,y + 6\,y^2 - 2\,y^3 + (4 - 8\,y + 4\,y^2)\,z + \\
& \qquad (1 - 3\,y)\,z^2 + z^3 + \{\, 4 - 12\,y + 12\,y^2 - 4\,y^3 + \\
& \qquad (2 - 10\,y + 8\,y^2)\,z - (3 + 7\,y)\,z^2 + 3\,z^3 \,\}\,\varepsilon + \\
& \qquad \{\, 2 - 6\,y + 6\,y^2 - 2\,y^3 - 4\,(1-y)\,y\,z - \\
& \qquad 5\,y\,z^2 + 3\,z^3 \,\}\,\varepsilon^2 \Big) \mathcal{I}_{-1} \\
& \quad - m_b^6 \Big( (1-y)\,(1-y+z) + \{\, 2 + 2\,y^2 - z - 2\,y\,(2+z) \,\}\,\varepsilon + \\
& \qquad \{\, 1 + y^2 - z - y\,(2+z) \,\}\,\varepsilon^2 \Big) \mathcal{I}_{-2} \Bigg],
\end{aligned}
$$

$$
\begin{aligned}
{}^{5}\mathcal{S} = \\
& 64 \Bigg[ 4\,\frac{1}{z} \Big( -1 + y + x + (2\,y - 2 - z)\,\varepsilon \Big)\,\varepsilon\,\mathcal{I}_{\ 1} \\
& \quad + 2\,m_b^2\,\frac{1}{z} \Big( (z-2)\,z + \{\, 2 + 2\,y^2 - (4-z)\,y - 2\,z + z^2 \,\}\,\varepsilon +
\end{aligned}
$$

$$
\begin{aligned}
& \left\{\ 2-4\,y+2\,y^2+z+3\,z^3\ \right\}\varepsilon^2\Big)\,\mathcal{I}_{\ 0} \\
&+\ m_b^4\,\frac{1}{z}\Big(\,4\,z\,(1-y+z)+\left\{\ -2+6\,y-6\,y^2+2\,y^3+\right. \\
&\qquad (2+2\,y-4\,y^2)\,z+(6+3\,y)\,z^2-z^3\ \Big\}\,\varepsilon+ \\
&\qquad \left\{\ -2+6\,y-6\,y^2+2\,y^3+4\,(1-y)\,y\,z+\right. \\
&\qquad \left.(5+4\,y)\,z^2-2\,z^3\ \right\}\varepsilon^2\Big)\,\mathcal{I}_{-1} \\
&+\ m_b^6\Big(\ -2\,z+\left\{\,1+y^2-2\,z-y\,(2+z)\,\right\}\varepsilon+ \\
&\qquad \left\{\,1+y^2-z-y\,(2+z)\,\right\}\varepsilon^2\ \Big)\,\mathcal{I}_{-2}\ \Bigg]\,. \qquad (3.65)
\end{aligned}
$$

The specific calculations of $\mathcal{I}_i$ are explained in Appendix A. The extraction of these singularities are possible by the expansion of $z^{1-\varepsilon}$ and $z^{1-2\varepsilon}$, which are elucidated in Appendix A.

### 3.3.3 Differential Decay Rate with $\alpha_s$ Corrections

In the previous two sections we calculated the virtual and real gluon corrections and showed both of them to have singularities of the types $\frac{1}{\varepsilon}$ and $\frac{1}{\varepsilon^2}$. These singularities cancel each other when the two corrections are summed, and finally we obtain a finite result for the decay rate. The triple differential decay rate in variables $x_e$, $y$ and $z$ with $\alpha_s$ corrections is

$$
\begin{aligned}
\frac{d^3\,\Gamma}{dx_e dy dz} &= \frac{d^3\,\Gamma^{Born}}{dx_e dy dz}\ +\ \frac{d^3\,\Gamma^{\alpha_s}}{dx_e dy dz}\ +\ \mathcal{O}(\alpha_s^2) \\
&= \frac{G_F^2|V_{ub}|^2 m_b^5}{16\pi^3}\Bigg[\delta(z)\,(x_e-y)\,(1-x_e+y) \\
&\quad +\ \frac{C_F\alpha_s}{4\pi}\Bigg(\delta(z)\,f_0(x_e,y)\ +\ \left[\frac{1}{z}\right]_+ f_1(x_e,y,z) \\
&\qquad +\ \left[\frac{\ln(z)}{z}\right]_+ f_2(x_e,y,z)\ +\ f_3(x_e,y,z)\Bigg)\Bigg]\,, \qquad (3.66)
\end{aligned}
$$

$$
\begin{aligned}
f_0(x_e,y,z) &= 5\,(x_e-y)\,(x_e-y-1) \\
&\quad +\ \frac{4}{3}\pi^2\,(x_e-y)\,(x_e-y-1) \\
&\quad -\ 2\,(5x_e-5y-4)\,(x_e-y)\,\ln(1-y) \\
&\quad +\ 8\,(x_e-y)\,(x_e-y-1)\,\ln(1-y)^2
\end{aligned}
$$

$$+ 4\,(x_e - y)\,(x_e - y - 1)\,\mathrm{Li}_2(y)\,, \tag{3.67}$$

$$\begin{aligned} f_1(x_e,y,z) &= \frac{1}{2^6\,\mathcal{P}_3(y,z)^6}\Bigg(\big(x_e-y\big)\big(x_e-y+z-1\big)(1-y)^4\times \\ &\qquad\qquad \big(7-14y+7y^2-6(1+y)z+3z^2\big)\Bigg) \\ &\quad - \frac{1}{2^2\,\mathcal{P}_3(y,z)^5}\Bigg(\big(x_e-y\big)\big(x_e-y+z-1\big)(1-y)^5\times \\ &\qquad\qquad \ln\big(\mathcal{P}_0(y,z)+\mathcal{P}_3(y,z)\big)\Bigg)\,, \end{aligned} \tag{3.68}$$

$$f_2(x_e,y,z) = \frac{1}{2^3\,\mathcal{P}_3(y,z)^5}\big(x_e-y\big)\big(x_e-y+z-1\big)(1-y)^5\,, \tag{3.69}$$

$$\begin{aligned} f_3(x_e,y,z) &= \frac{-1}{2^6\,\mathcal{P}_3(y,z)}\big(g_0(y,z)+x_e\,g_1(y,z)+x_e^2\,g_2(y,z)\big) \\ &\quad + \frac{-1}{2^4\,\mathcal{P}_3(y,z)}\Bigg(\big(h_0(y,z)+x_e\,h_1(y,z)+x_e^2\,h_2(y,z)\big)\times \\ &\qquad\qquad \ln\left(\frac{\mathcal{P}_0(y,z)+\mathcal{P}_3(y,z)}{\mathcal{P}_0(y,z)-\mathcal{P}_3(y,z)}\right)\Bigg)\,, \end{aligned} \tag{3.70}$$

$$\begin{aligned} g_0(y,z) &= y\,(11+9\,y-120\,y^2+170\,y^3-45\,y^4-51\,y^5+26\,y^6) \\ &\quad + y\,(-26-43\,y+54\,y^2+44\,y^3+52\,y^4-81\,y^5)\,z \\ &\quad + y\,(37+84\,y+28\,y^2+64\,y^3+107\,y^4)\,z^2 \\ &\quad + y\,(-45-95\,y-105\,y^2-75\,y^3)\,z^3 \\ &\quad + y\,(32+53\,y+27\,y^2)\,z^4+(-9-4\,y)\,y\,z^5\,, \end{aligned} \tag{3.71}$$

$$\begin{aligned} g_1(y,z) &= -19+12\,y+101\,y^2-144\,y^3-9\,y^4+100\,y^5-41\,y^6 \\ &\quad + (46+44\,y-80\,y^2-68\,y^3-30\,y^4+88\,y^5)\,z \\ &\quad + (-37-152\,y-62\,y^2-120\,y^3-77\,y^4)\,z^2 \\ &\quad + (5+120\,y+117\,y^2+30\,y^3)\,z^3 \\ &\quad + (8-32\,y-4\,y^2)\,z^4-3\,z^5\,, \end{aligned} \tag{3.72}$$

$$\begin{aligned} g_2(y,z) &= 19-61\,y+54\,y^2+14\,y^3-41\,y^4+15\,y^5 \\ &\quad + (-27-6\,y+76\,y^2-26\,y^3-17\,y^4)\,z \\ &\quad + (10+56\,y+58\,y^2+4\,y^3)\,z^2 \\ &\quad + (5-24\,y+3\,y^2)\,z^3+(-3-y)\,z^4\,, \end{aligned} \tag{3.73}$$

$$
\begin{aligned}
h_0(y,z) &= y\,(-12\,y + 28\,y^2 - 12\,y^3 - 12\,y^4 + 8\,y^5) \\
&\quad + y\,(1 + 6\,y - 2\,y^2 + 16\,y^3 - 21\,y^4)\,z \\
&\quad + y\,(4\,y + 8\,y^2 + 24\,y^3)\,z^2 \\
&\quad + y\,(-6 - 16\,y - 16\,y^2)\,z^3 \\
&\quad + y\,(6 + 6\,y)\,z^4 - y\,z^5\,, \qquad (3.74)
\end{aligned}
$$

$$
\begin{aligned}
h_1(y,z) &= 2 + 6\,y - 16\,y^2 - 8\,y^3 + 30\,y^4 - 14\,y^5 \\
&\quad + (-1 - 11\,y - y^2 - 13\,y^3 + 26\,y^4)\,z \\
&\quad + (-1 - 2\,y - 23\,y^2 - 22\,y^3)\,z^2 \\
&\quad + (-1 + 13\,y + 10\,y^2)\,z^3 \\
&\quad + (1 - 2\,y)\,z^4\,, \qquad (3.75)
\end{aligned}
$$

$$
\begin{aligned}
h_2(y,z) &= -2 + 12\,y^2 - 16\,y^3 + 6\,y^4 \\
&\quad + (-1 + 13\,y - 5\,y^2 - 7\,y^3)\,z \\
&\quad + (8\,y + 4\,y^2)\,z^2 \\
&\quad + (1 - y)\,z^3\,. \qquad (3.76)
\end{aligned}
$$

The results in Eqs.(3.66)–(3.76) agree with the results in [4], which were calculated in the finite gluon mass regularization scheme.

# Chapter 4

# Radiatively Corrected Spectra from $b$-quark decay

We can obtain various spectra from $b$-quark and $B$-meson decays. Firstly, the electron energy spectrum can be used in determining $|V_{ub}|$. In the end point region of the electron energy spectrum, the $b \to c$ background is removed and pure $b \to u$ events can be collected. However, the disadvantage of this method is that the relevant region is too narrow to take a sufficient number of events.

The spectrum of the leptonic invariant mass allows a wider range to select events, as noted by Bauer, Ligeti, and Luck [19, 20]. Another relevant spectrum to extract $|V_{ub}|$ is the hadronic invariant mass spectrum [22, 23]. In this chapter we present these three kinds of spectra, supplemented by the hadronic energy spectrum from $b$-quark decay. The same kinds of spectra from $B$-meson decay are shown in Chapter 5. We compare the Born approximated results with the radiatively corrected results and observe how the spectra are changed by $QCD$ corrections of order $\alpha_s$.

In the previous chapter we presented the analytical results for the triple differential decay rate, which are expressed in terms of variables $x_e = \frac{2E_e}{m_b}$, $y = \frac{W^2}{m_b^2}$, and $z = \frac{P^2}{m_b^2}$ as defined in Section 3.1. The explicit analytical forms of differential decay rate $\frac{d\Gamma}{dx_e}$, $\frac{d\Gamma}{dz}$, and $\frac{d\Gamma}{dy}$ are found in references [4] and [21].

We compare the radiative corrections at different values of the strong coupling constant $\alpha_s$. In this section, we fix the mass of $b$-quark as $m_b = 4.80\ GeV$. We take $\alpha_s(m_b^2 = 4.80^2\ GeV^2) = 0.22$ which corresponds to $\Lambda^{(5)}_{QCD} = 100\ MeV$ and $\alpha_s(m_b^2 = 4.80^2\ GeV^2) = 0.25$ which corresponds to $\Lambda^{(5)}_{QCD} = 200\ MeV$. All the numerical analyses were carried out using VEGAS [60].

## 4.1 Electron Energy Spectrum

After integrating the triple differential decay rate in Eq.(3.66) in Chapter 3 over $y$ and $z$, we obtain the differential decay formula with respect to $x_e$. The variable $x_e$ is defined as $x_e \equiv \frac{2\,E_e}{m_b}$ in Section 3.1 and varies from 0 to 1. Subsequently, the electron energy $E_e$ varies from 0 to $\frac{m_b}{2}$ and the differential decay rate formula with respect to $x_e$ reads [4]

$$\begin{aligned}
\frac{1}{\Gamma_0}\frac{d\Gamma}{dE_e} &= \frac{16}{m_b^4}E_e^2\,(3m_b-4E_e)\left[1\;-\;\frac{C_F\,\alpha_s}{2\pi}\,\mathcal{F}_E(E_e)\right], \\
\mathcal{F}_E(E_e) &= \ln^2\left(\frac{m_b-2E_e}{m_b}\right)+2\mathrm{Li}_2\left(\frac{2\,E_e}{m_b}\right)+\frac{2\pi^2}{3} \\
&\quad -\left(\frac{172\,E_e^2-153\,E_e\,m_b+41\,m_b^2}{12\,E_e\,(4E_e-3m_b)}\right) \\
&\quad +\left(\frac{125\,E_e^3-168\,E_e^2\,m_b+72\,E_e\,m_b^2-41\,m_b^3}{24\,E_e^2\,(4E_e-3m_b)}\right)\times \\
&\quad \ln\left(\frac{m_b-2\,E_e}{m_b}\right), \qquad (4.1)
\end{aligned}$$

and the Born approximation of the $b$-quark decay rate $\Gamma_0$ and the radiatively corrected decay rate of the $b$-quark $\Gamma$ are [4]

$$\Gamma_0 = \frac{G_F^2\,|V_{ub}|^2\,m_b^5}{192\,\pi^3}, \qquad (4.2)$$

$$\Gamma = \Gamma_0\left[1\;-\;\frac{C_F\,\alpha_s}{2\pi}\left(\pi^2\;-\;\frac{25}{4}\right)\right], \qquad (4.3)$$

where $C_F=\frac{4}{3}$. We use the formula in Eq.(4.1) for the numerical analysis.

Figure 4.1(a) shows three electron energy spectra from $b$-quark decay. The Born approximation of the electron energy spectrum is normalized with $\Gamma_0$ and the radiatively corrected spectra with $\Gamma$ at the relevant $\alpha_s$ values. The dotted line in Figure 4.1(a) is the Born approximation of the electron energy spectrum and the solid line shows the radiatively corrected spectrum at $\alpha_s = 0.22$. They coincide with the results in [4], where the spectrum is depicted with respect to $x_e$. The dashed line in Figure 4.1(a) is the radiatively corrected spectrum at

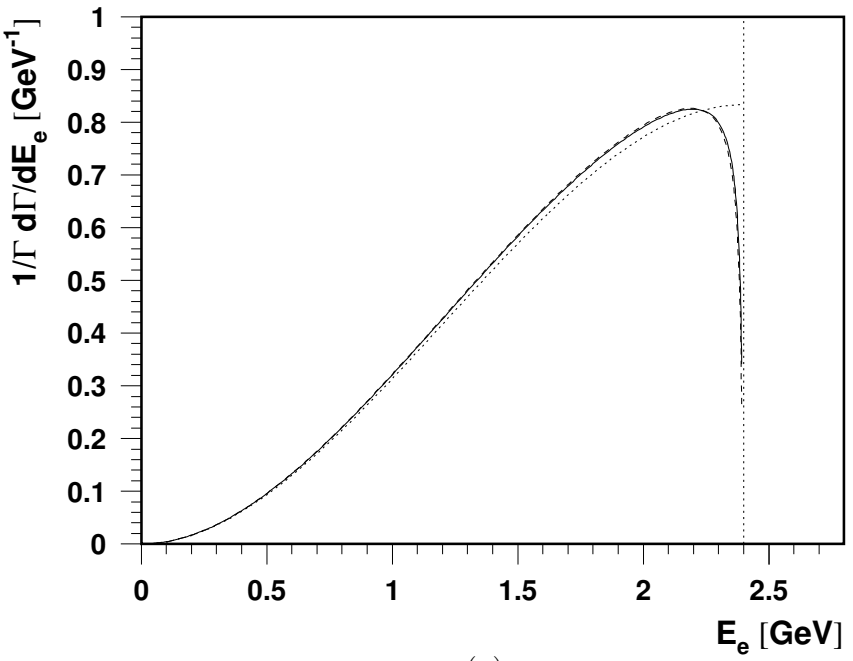


(a)

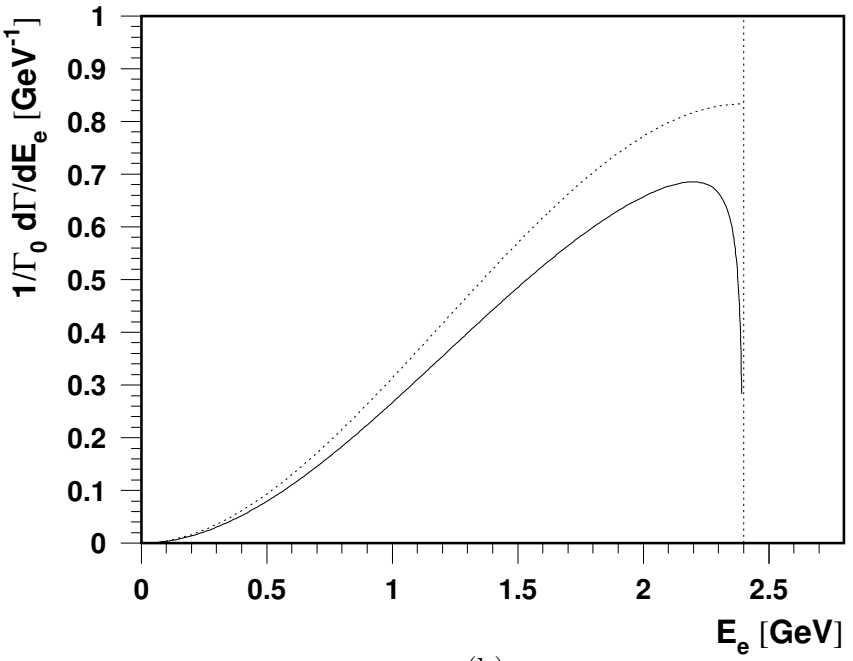


(b)

Figure 4.1: (a) The radiatively corrected electron energy spectrum normalized with $\Gamma$. The dotted line shows the Born approximation of the spectrum normalized with $\Gamma_0$. The solid line displays the radiatively corrected spectrum at $\alpha_s = 0.22$, and the dashed line at $\alpha_s = 0.25$. (b) The electron energy spectrum normalized by $\Gamma_0$. The dotted line shows the Born approximation of the spectrum. The solid line displays the radiatively corrected spectrum at $\alpha_s = 0.22$.

$\alpha_s = 0.25$ and normalized with $\Gamma$ at $\alpha_s = 0.25$. As seen in Figure 4.1(a), *QCD* corrections change the shape of the spectrum mostly at the end point of electron energy. However, the change of the strong coupling constant value from $\alpha_s = 0.22$ to $\alpha_s = 0.25$ does not affect the shape of the spectrum visibly.

The spectra in Figure 4.1(b) are both normalized with $\Gamma_0$. The dotted line in Figure 4.1(b) is the Born approximation of the electron energy spectrum and the solid line in Figure 4.1(b) presents the spectrum with *QCD* corrections at $\alpha_s = 0.22$. The ratio of $\Gamma$ to $\Gamma_0$ is $\Gamma/\Gamma_0 = 0.8310$ at $\alpha_s = 0.22$ and $\Gamma/\Gamma_0 = 0.8080$ at $\alpha_s = 0.25$. The difference between $\Gamma(\alpha_s = 0.22)$ and $\Gamma(\alpha_s = 0.25)$ is not large, but $\Gamma$ is different from $\Gamma_0$ by approximately 20 % for both cases. From this fact, we can conclude that the major effect of the order $\alpha_s$ corrections is in the integrated decay rate $\Gamma$, and $\frac{1}{\Gamma}\frac{d\Gamma}{dE_e}$ is not changed very much by *QCD* corrections of order $\alpha_s$.

## 4.2 Leptonic Invariant Mass Spectrum

The four–momentum of the lepton system is denoted by $W = p_e + p_\nu$, and the scaled squared momentum or invariant mass of $e - \bar{\nu}_e$ system is defined as $y \equiv \frac{W^2}{m_b^2}$ in Section 3.1. After integrating the triple differential decay rate over $z$ and $x_e$, we obtain the leptonic invariant mass spectrum. The explicit formula is found in [21] and reads in terms of $W^2$

$$\frac{1}{\Gamma_0}\frac{d\Gamma}{dW^2} = \frac{2}{m_b^2}\left(1-\frac{W^2}{m_b^2}\right)^2\left(1+2\frac{W^2}{m_b^2}\right)\left[1-\frac{2\alpha_s}{3\,\pi}\,\mathcal{F}_W(W^2)\right], \tag{4.4}$$

$$\begin{aligned}\mathcal{F}_W(W^2) &= \frac{m_b^6\, f_W(W^2)}{2\,(m_b^2-W^2)^2\,(m_b^2+2W^2)} \;+\; \pi^2 \;+\; 2\mathrm{Li}_2\left(\frac{W^2}{m_b^2}\right) \\ &\quad - 2\mathrm{Li}_2\left(\frac{m_b^2-W^2}{m_b^2}\right), \end{aligned} \tag{4.5}$$

$$\begin{aligned} f_W(W^2) &= 8\,\frac{W^2}{m_b^2}\left(1-\frac{W^2}{m_b^2}-2\frac{W^4}{m_b^4}\right)\ln\left(\frac{\sqrt{W^2}}{m_b}\right) \\ &\quad + 2\left(1-\frac{W^2}{m_b^2}\right)^2\left(5+4\frac{W^2}{m_b^2}\right)\ln\left(\frac{m_b^2-W^2}{m_b^2}\right) \end{aligned}$$

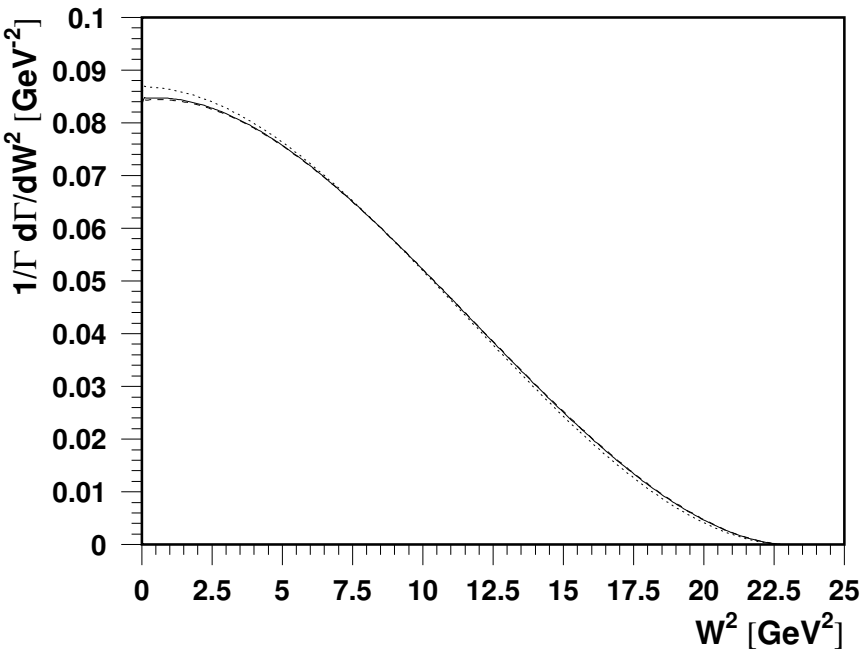


Figure 4.2: The leptonic invariant mass spectrum with radiative corrections. The dotted line shows the Born approximation of the leptonic invariant mass spectrum. The solid line displays the radiatively corrected spectrum at $\alpha_s = 0.22$, and the dashed line at $\alpha_s = 0.25$.

$$- \left(1 - \frac{W^2}{m_b^2}\right)\left(5 + 9\frac{W^2}{m_b^2} - 6\frac{W^4}{m_b^4}\right). \tag{4.6}$$

The spectrum with respect to $W^2$ is displayed in Figure 4.2 at $\alpha_s(m_b^2 = 4.8^2\ GeV^2) = 0.22$ at $\Lambda_{QCD} = 100\ MeV$ and at $\alpha_s(m_b^2 = 4.8^2\ GeV^2) = 0.25$ at $\Lambda_{QCD} = 200\ MeV$. The contributions of the $QCD$ corrections of order $\alpha_s$ are distinguished in the region of small $W^2$. As is seen in Figure 4.2, the contribution of the change of $\alpha_s$ is not significant. The change in the spectrum from $\alpha_s = 0.22 \rightarrow \alpha_s = 0.25$ is invisible. The effect of $QCD$ corrections of order $\alpha_s$ lies mostly in the total decay rate $\Gamma_0 \rightarrow \Gamma$. We consider the strong coupling constant $\alpha_s = \alpha_s(W^2)$, the scale of which depends on the leptonic in-

| $W^2\,(GeV^2)$ | $\alpha_s(W^2)$ | $\Lambda_{QCD}\,(MeV)$ | $W^2\,(GeV^2)$ | $\alpha_s(W^2)$ | $\Lambda_{QCD}\,(MeV)$ |
|---|---|---|---|---|---|
| 2.5 | 0.25 | 100 | $4.8^2$ | 0.22 | 100 |
| 2.5 | 0.32 | 200 | $4.8^2$ | 0.25 | 200 |
| 2.5 | 0.51 | 500 | $4.8^2$ | 0.36 | 500 |

Table 4.1: $\alpha_s(W^2)$ at various $\Lambda_{QCD}$.

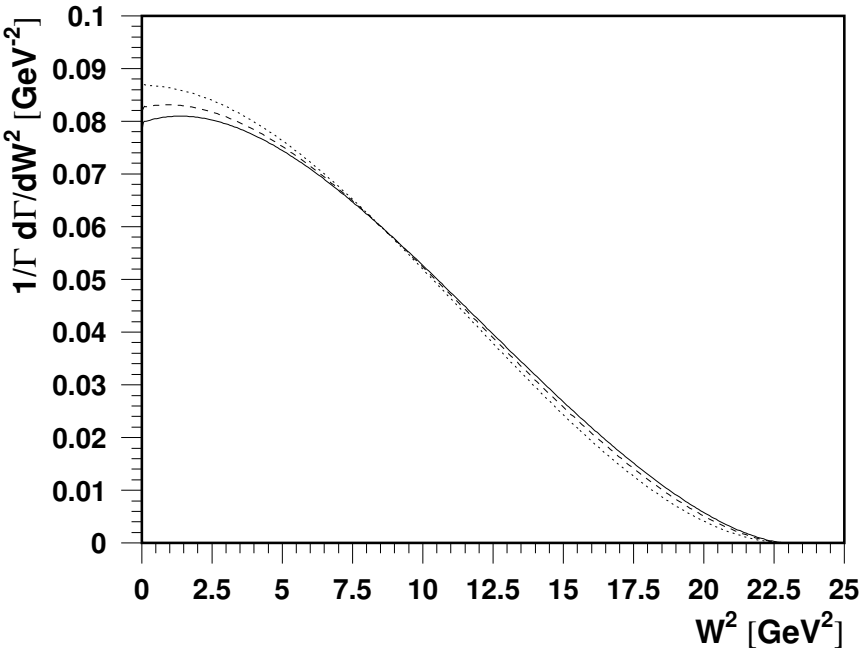


(a)

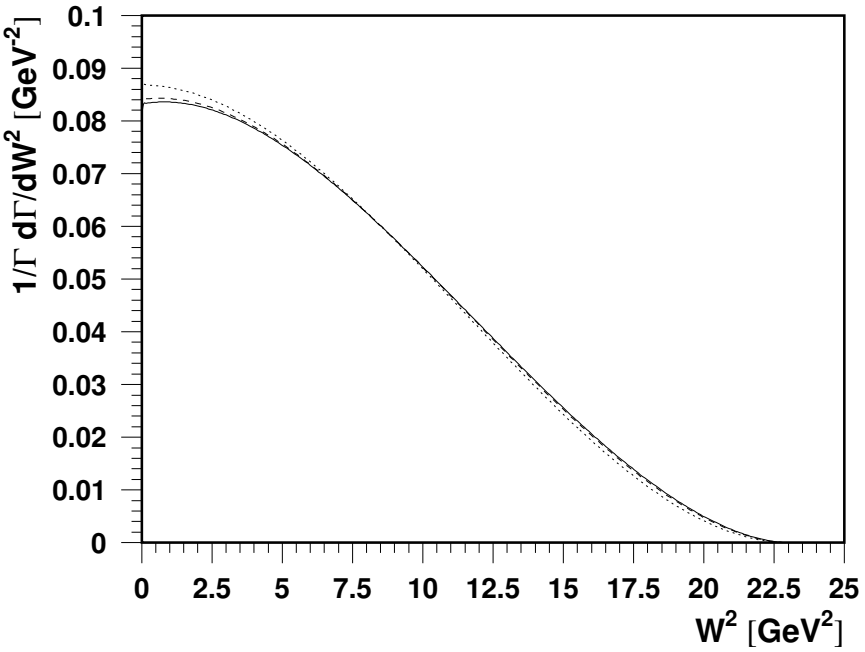


(b)

Figure 4.3: The radiatively corrected leptonic invariant mass spectrum at various $\alpha_s$ is compared with the Born approximation of the spectrum. (a) The dotted line shows the Born approximation of the leptonic invariant mass spectrum. The solid line displays the radiatively corrected spectrum at $\alpha_s = 0.51$, and the dashed line at $\alpha_s = 0.36$. (b) The dotted line shows the Born approximation of the leptonic invariant mass spectrum. The solid line displays the radiatively corrected spectrum at $\alpha_s = 0.32$, and the dashed line at $\alpha_s = 0.26$.

variant mass $W^2$ instead of $\alpha_s = \alpha_s(m_b^2)$. The various $\alpha_s$ values are displayed in Table 4.1 and $\alpha_s(W^2 = 4.8^2\ GeV^2)$ is found to be less sensitive to $\Lambda_{QCD}$ than $\alpha_s(W^2 = 2.5\ GeV^2)$.

The spectra at $\alpha_s = 0.51$ and at $\alpha_s = 0.36$ are displayed in Figure 4.3, and the spectra at $\alpha_s = 0.32$ and at $\alpha_s = 0.26$ in Figure 4.3. In Figure 4.2 and 4.3 we have examined the influence of the $\alpha_s(W^2)$ value. As shown in both figures, we have found that this influence is not large.

## 4.3 Hadronic Energy Spectrum

According to Heavy Quark Effective Theory (HQET), we expand the hadronic energy $E_H$ and the squared hadronic invariant mass $s_H$ in terms of $\bar{\Lambda}$, $\lambda_1$, and $\lambda_2$ [61, 62],

$$E_H = \bar{\Lambda} - \frac{\lambda_1 + 3\lambda_2}{2M_B} + \left( M_B - \bar{\Lambda} + \frac{\lambda_1 + 3\lambda_2}{2M_B} \right) \hat{E}_0 + \mathcal{O}(1/m_b)\,, \quad (4.7)$$

$$s_H = m_f^2 + \bar{\Lambda}^2 + (M_B^2 - 2\bar{\Lambda}M_B + \bar{\Lambda}^2 + \lambda_1 + 3\lambda_2)(\hat{s}_0 - \hat{m}_f^2) + (2\bar{\Lambda}M_B - 2\bar{\Lambda}^2 - \lambda_1 - 2\lambda_2)\,\hat{E}_0 + \mathcal{O}(1/m_b)\,, \quad (4.8)$$

where $\hat{m}_f = m_f/m_b$ and $m_f$ is the mass of the quark in the final state.

In HQET, the four–momentum of the $B$-meson is denoted as $P_B^\mu = M_B\, v^\mu$, and the $\hat{E}_0$ and $\hat{s}_0$ are defined in the parton level [63],

$$\hat{E}_0 = v \cdot (p_b - W)/m_b = 1 - v \cdot \hat{W}\,, \quad (4.9)$$

$$\hat{s}_0 = (p_b - W)^2/m_b^2 = 1 - 2v \cdot \hat{W} + \hat{W}^2\,, \quad (4.10)$$

where $\hat{W}^\mu \equiv W^\mu/m_b$, and $W$ denotes the lepton system as defined in Section 3.1. The relationship between the quark mass and meson mass in HQET [61, 62] gives rise to the parameters $\bar{\Lambda}$, $\lambda_1$ and $\lambda_2$,

$$M_B = m_b + \bar{\Lambda} - \frac{\lambda_1 + 3\lambda_2}{2m_b} + \mathcal{O}(1/m_b^2)\,, \quad (4.11)$$

$$M_{B^*} = m_b + \bar{\Lambda} - \frac{\lambda_1 - \lambda_2}{2m_b} + \mathcal{O}(1/m_b^2)\,. \quad (4.12)$$

We obtain a relation for the hadronic energy $E_H$

$$\begin{aligned} E_H &= M_B - v\cdot W \\ &= M_B - \frac{p_b\cdot W}{m_b} \\ &= \bar{\Lambda} + \frac{p_b\cdot P}{m_b}\,, \end{aligned} \tag{4.13}$$

where $\bar{\Lambda} = M_B - m_b$ and the $\frac{1}{m_b}$ terms and terms of higher orders of $\frac{1}{m_b}$ in Eq.(4.11) and in Eq.(4.12) are ignored. $P$ and $W$ are defined in Section 3.1. Further explanation of $\lambda_1$ and $\lambda_2$ is found in Chapter 5.

We write Eq.(4.13) in terms of $z$ and $y$, and the result reads

$$\frac{1}{m_b}(E_H - \bar{\Lambda}) = 1 - y + z\,. \tag{4.14}$$

We define a new variable $\hat{z} \equiv 1 - y + z$ and obtain $\hat{z}\, m_b = E_H - \Lambda$. The differential decay rate formula in terms of $\hat{z}$ is found in [4]. Subsequently, we obtain the differential decay rate formula in terms of $E_H$

$$\begin{aligned} \frac{1}{\Gamma_0}\frac{d\Gamma}{dE_H} &= \frac{16}{m_b^3}\left(E_H - \bar{\Lambda}\right)\left(\frac{3m_b - 4E_H + 4\bar{\Lambda}}{m_b}\right)\times \\ &\qquad \left[1 - C_F\,\frac{\alpha_s}{2\pi}\mathcal{F}_H^1(E_H)\right], \qquad \bar{\Lambda} \;\le\; E_H \;\le\; \frac{m_b}{2} + \bar{\Lambda}\,, \\ \frac{1}{\Gamma_0}\frac{d\Gamma}{dE_H} &= C_F\,\frac{\alpha_s}{2\pi}\,\mathcal{F}_H^2(E_H)\,, \qquad \frac{m_b}{2} + \bar{\Lambda} \;\le\; E_H \;\le\; m_b + \bar{\Lambda}\,, \end{aligned} \tag{4.15}$$

and

$$\begin{aligned} \mathcal{F}_H^1 &= 2\mathrm{Li}_2\left(\frac{m_b - 2(E_H - \bar{\Lambda})}{m_b}\right) + \pi^2 + \left(\frac{8E_H - 8\bar{\Lambda} - 9m_b}{4E_H - 4\bar{\Lambda} - 3m_b}\right)\ln\left(\frac{2(E_H - \bar{\Lambda})}{m_b}\right) \\ &\quad - \frac{1}{90\, m_b^3\,(4E_H - 4\bar{\Lambda} - 3m_b)}\times \\ &\quad \Big( -16E_H^4 + E_H^3\big(64\bar{\Lambda} + 84m_b\big) - E_H^2\big(96\bar{\Lambda}^2 + 252\bar{\Lambda}m_b + 585m_b^2\big) \\ &\qquad + E_H\big(64\bar{\Lambda}^3 + 252\bar{\Lambda}^2 m_b + 1170m_b^2 + 1860m_b^3\big) \\ &\qquad - 16\bar{\Lambda}^4 - 84\bar{\Lambda}^3 m_b - 585\bar{\Lambda}^2 m_b^2 - 1860\bar{\Lambda}m_b^2 - 1215m_b^4\Big)\,, \\ \mathcal{F}_H^2 &= \frac{16}{m_b^3}\left(E_H - \bar{\Lambda}\right)\left(\frac{3m_b - 4E_H + 4\bar{\Lambda}}{m_b}\right)\times \end{aligned}$$

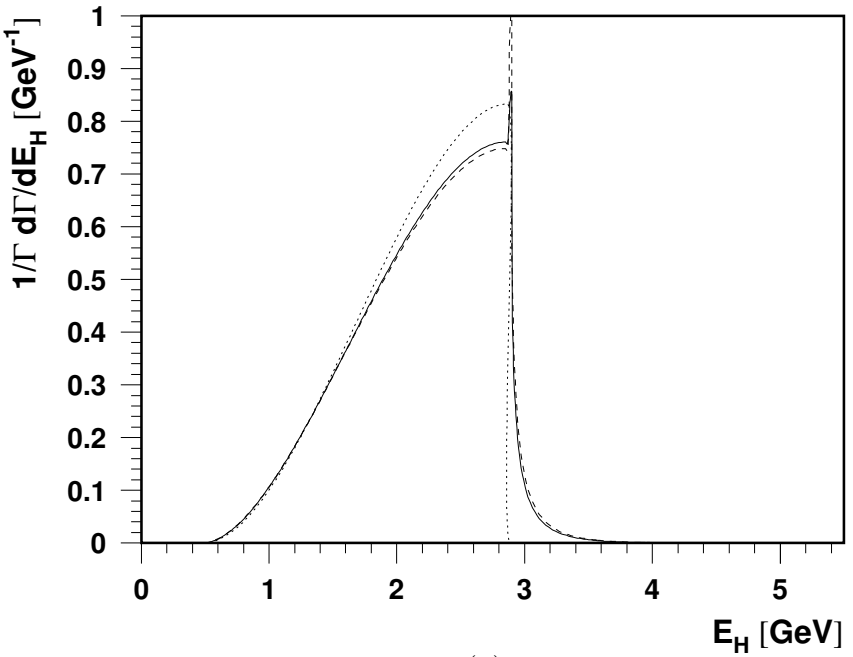


(a)

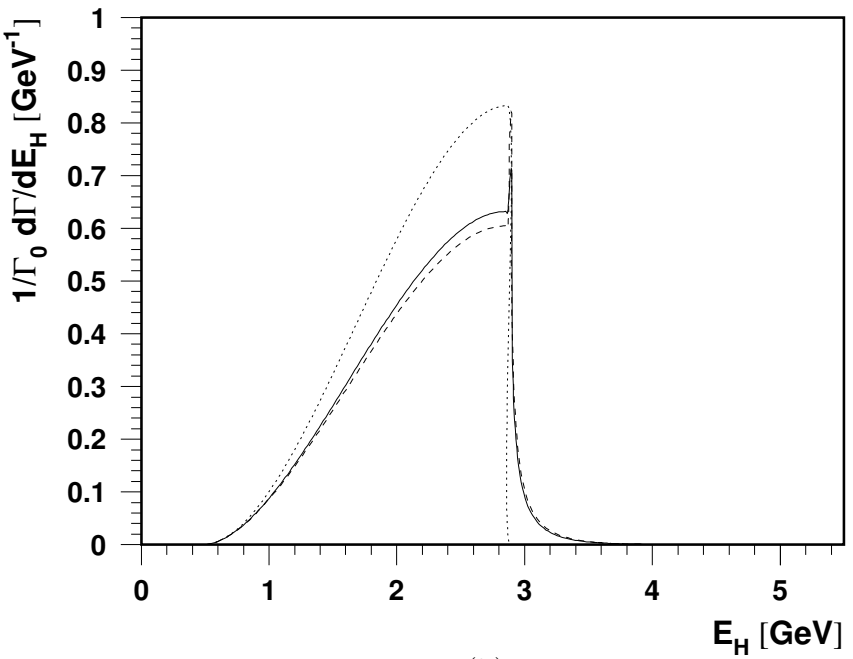


(b)

Figure 4.4: (a) The hadronic energy spectrum $d\Gamma/dE_H$ in units of $\Gamma$. The dotted line shows the Born approximation of the spectrum normalized with $\Gamma_0$. The solid line displays the radiatively corrected spectrum at $\alpha_s = 0.22$, and the dashed line at $\alpha_s = 0.25$. (b) The hadronic energy spectrum $d\Gamma/dE_H$ normalized with $\Gamma_0$. The dotted line shows the Born approximation of the spectrum. The solid line displays the radiatively corrected spectrum at $\alpha_s = 0.22$, and the dashed line at $\alpha_s = 0.25$.

$$\left[\ln^2\left(\frac{2(E_H-\bar{\Lambda})-m_b}{m_b}\right)-2\ln^2\left(\frac{2(E_H-\bar{\Lambda})}{m_b}\right)-4\mathrm{Li}_2\left(\frac{m_b}{2(E_H-\bar{\Lambda})}\right)+\frac{\pi^3}{3}\right]$$
$$+\left(\frac{4(m_b-E_H+\bar{\Lambda})}{45\,m_b^7}\right)\times$$
$$\Big(32E_H^5\;-\;8\,E_H^4\,(20\bar{\Lambda}+17m_b)\;+\;2\,E_H^3\,(160\bar{\Lambda}^2+272\bar{\Lambda}m_b+517m_b^2)$$
$$-\,2\,E_H^2\,(160\bar{\Lambda}^3+408\bar{\Lambda}^2m_b+1551\bar{\Lambda}m_b^2+1473m_b^3)$$
$$+\,E_H\,(160\bar{\Lambda}^4+544\bar{\Lambda}^3m_b+3102\bar{\Lambda}^2m_b^2+5892\bar{\Lambda}m_b^3+1899m_b^4)$$
$$-\,32\bar{\Lambda}^5-136\bar{\Lambda}^4m_b-1034\bar{\Lambda}^3m_b^2-2946\bar{\Lambda}^2m_b^3-1899\bar{\Lambda}m_b^4+312m_b^5\Big)$$
$$+\frac{2}{3\,m_b^4}\,\ln\left(\frac{2(E_H-\bar{\Lambda})-m_b}{m_b}\right)\times$$
$$\Big(-64E_H^3+48\,E_H^2\,(4\bar{\Lambda}+m_b)-24\,E_H\,(8\bar{\Lambda}^2+4\bar{\Lambda}m_b-m_b^2)$$
$$+\,64\bar{\Lambda}^3\;+\;48\bar{\Lambda}^2m_b\;-\;24\bar{\Lambda}m_b^2\;+\;5m_b^3\Big)\,. \tag{4.16}$$

In the Born approximation, the hadronic energy spectrum expands until the point $E_H=\frac{m_b}{2}+\bar{\Lambda}$, and it gains contributions from the radiative corrections beyond that point.

The radiatively corrected hadronic energy spectra at different $\alpha_s$ values are displayed in Figure 4.4 in comparison with the Born approximation of the spectrum. The contribution of *QCD* corrections of order $\alpha_s$ is dominant beyond $E_H=\frac{m_b}{2}+\bar{\Lambda}$. Whereas the Born approximation of the hadronic energy spectrum ends at $E_H=\frac{m_b}{2}+\bar{\Lambda}$, the radiatively corrected spectrum expands beyond that point and does not fall to 0 immediately at $E_H=\frac{m_b}{2}+\bar{\Lambda}$. The Born approximation of the hadronic energy spectrum and the radiatively corrected spectra in Figure 4.4(a) are normalized by $\Gamma_0$ and $\Gamma$ in Eqs.(4.2) and (4.3), respectively. We present the hadronic energy spectra which are all normalized by $\Gamma_0$ in Figure 4.4(b).

In Figure 4.4 we have employed $\bar{\Lambda}=M_B-m_b=0.48\;GeV$. In Figure 4.5(a) we display the hadronic energy spectra at $\bar{\Lambda}=0$. The effect of $\bar{\Lambda}$ on the hadronic energy spectrum is observed more clearly in Figure 4.5(b). The shift of the spectrum from left to right according to the change $\bar{\Lambda}=0\rightarrow\bar{\Lambda}=0.48\;GeV$ is by the amount of $\Delta E_H=0.48\;GeV$, which is obviously observed by comparing the two spectra in the Born approximation in Figure 4.5(b). All spectra in Figure 4.5(b) are normalized by $\Gamma_0$. The effect of order $\alpha_s$ corrections to the hadronic energy spectrum is much larger than to the electron energy spectrum or to the leptonic invariant mass spectrum. The effect of the $\alpha_s$ corrections is most apparent at the end point of $E_H$.

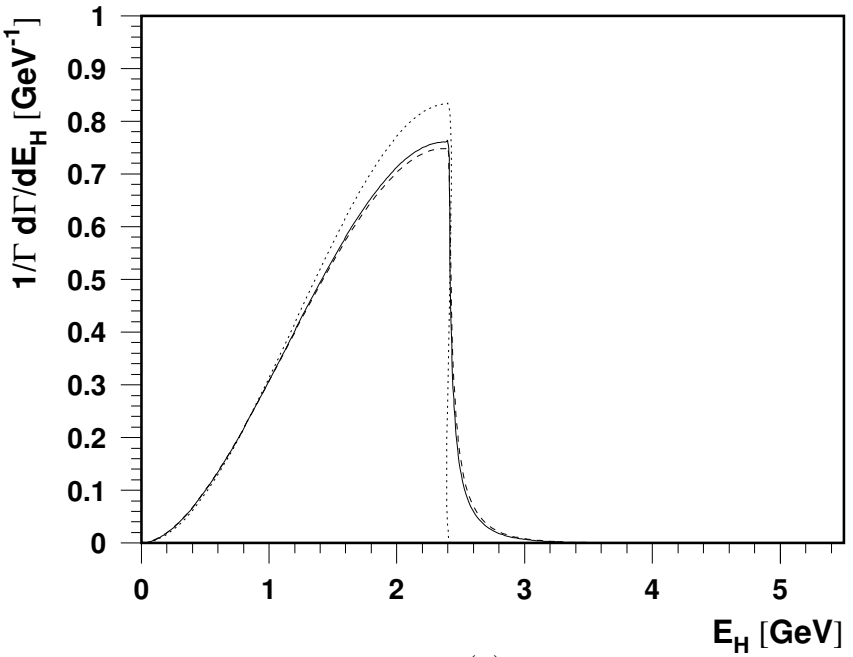


(a)

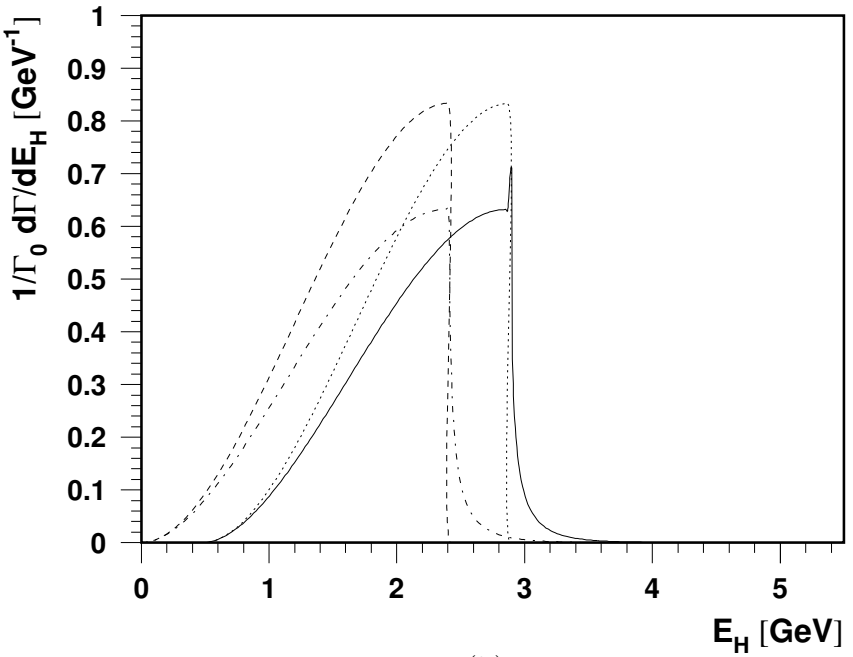


(b)

Figure 4.5: (a) The hadronic energy spectra at $\bar{\Lambda} = 0$. The dotted line shows the Born approximation of the spectrum. The solid line displays the spectrum with the radiative corrections at $\alpha_s = 0.22$, and the dashed line at $\alpha_s = 0.25$. (b) The comparison between the spectra with $\bar{\Lambda} = 0.48\ GeV$ and those with $\bar{\Lambda} = 0$ is displayed. The dashed line is the Born approximation of the hadronic energy spectrum, and the dot–dashed line is the spectrum with the radiative corrections at $\alpha_s = 0.22$. For both of the dashed line and the dot–dashed line, $\bar{\Lambda} = 0$. The dotted line shows the Born approximation of the spectrum with $\bar{\Lambda} = 0.48\ GeV$, and the solid line is the spectrum with the radiative corrections at $\alpha_s = 0.22$ with $\bar{\Lambda} = 0.48\ GeV$.

## 4.4 Hadronic Invariant Mass Spectrum

The squared hadronic invariant mass is given by

$$S_H = P^2 + \bar{\Lambda}\, m_b\, (1 - y + z) + \bar{\Lambda}^2\,, \tag{4.17}$$

and the hadronic invariant mass $M_H$ is defined as $M_H \equiv \sqrt{S_H}$. We display both the squared hadronic invariant mass $S_H$ spectrum and the hadronic invariant mass $M_H$ spectrum for $b$-quark decay in this section.

After replacing the variable $z$ with $S_H$ and integrating over $x_e$ and $y$, we obtain the differential decay rate in terms of $S_H$ as in [4], which reads

$$\begin{aligned}
\frac{1}{\Gamma_0}\frac{d\Gamma}{dS_H} &= \mathcal{F}_S^1(S_H,\bar{\Lambda}) - C_F\frac{\alpha_s}{2\,\pi}\,\mathcal{F}_S^2(S_H,\bar{\Lambda})\,, \qquad \bar{\Lambda}^2 \;\le\; S_H \;\le\; \bar{\Lambda}\,(m_b+\bar{\Lambda})\,,\\
\frac{1}{\Gamma_0}\frac{d\Gamma}{dS_H} &= C_F\frac{\alpha_s}{2\,\pi}\,\mathcal{F}_S^3(S_H,\bar{\Lambda})\,, \qquad \bar{\Lambda}\,(m_b+\bar{\Lambda}) \;\le\; S_H \;\le\; (m_b+\bar{\Lambda})^2\,,\\
\mathcal{F}_S^1 &= \frac{2}{\bar{\Lambda}^4 m_b^4}\left(S_H-\bar{\Lambda}^2\right)^2\left(2\bar{\Lambda}^2+3\bar{\Lambda}\,m_b-2S_H\right),\\
\mathcal{F}_S^2 &= \frac{2}{\bar{\Lambda}^4 m_b^4}\left(S_H-\bar{\Lambda}^2\right)^2\left(2\bar{\Lambda}^2+3\bar{\Lambda}\,m_b-2S_H\right)\times\\
&\quad\left[\pi^2+2\mathrm{Li}_2\!\left(\frac{\bar{\Lambda}^2+\bar{\Lambda}m_b-S_H}{\bar{\Lambda}m_b}\right)-2\mathrm{Li}_2\!\left(\frac{m_b^2S_H-\bar{\Lambda}^2}{\bar{\Lambda}^2}\right)\right]\\
&\quad+\ \ln\!\left(\frac{S_H}{\bar{\Lambda}^2}\right)\left(S_H^3\left\{-\frac{2}{3\,\bar{\Lambda}^4\,m_b^4}-\frac{16}{3\,\bar{\Lambda}^3\,m_b^5}+\frac{2}{\bar{\Lambda}^2m_b^6}-\frac{4}{3\bar{\Lambda}m_b^7}\right\}\right.\\
&\qquad\qquad+\ S_H^2\left\{-\frac{3}{\bar{\Lambda}^3\,m_b^3}+\frac{8}{\bar{\Lambda}^2\,m_b^4}+\frac{13}{\bar{\Lambda}\,m_b^5}-\frac{2}{m_b^6}-\frac{4}{3\,\bar{\Lambda}m_b^7}\right\}\\
&\qquad\qquad\left.+\ S_H\left\{\frac{6}{\bar{\Lambda}\,m_b^3}-\frac{4}{m_b^4}-10\,\frac{\bar{\Lambda}}{m_b^5}-8\,\frac{\bar{\Lambda}^2}{m_b^6}-4\,\frac{\bar{\Lambda}^3}{m_b^7}\right\}\right)\\
&\quad+\ \ln\!\left(\frac{S_H-\bar{\Lambda}^2}{\bar{\Lambda}\,m_b}\right)\left(-S_H\,\frac{8}{\bar{\Lambda}^4\,m_b^4}+S_H^2\left\{\frac{24}{\bar{\Lambda}^2\,m_b^4}+\frac{18}{\bar{\Lambda}^3\,m_b^3}\right\}\right.\\
&\qquad\qquad\left.-\ S_H\left\{\frac{24}{m_b^4}+\frac{36}{\bar{\Lambda}\,m_b^3}\right\}+8\frac{\bar{\Lambda}^2}{m_b^4}+18\frac{\bar{\Lambda}}{m_b^3}\ \right)\\
&\quad+\ S_H^3\left\{\frac{167}{9\,\bar{\Lambda}^4\,m_b^4}+\frac{34}{9\,\bar{\Lambda}^3\,m_b^5}-\frac{13}{3\,\bar{\Lambda}^2\,m_b^6}+\frac{40}{9\,\bar{\Lambda}\,m_b^7}\right\}\\
&\quad+\ S_H^2\left\{-\frac{51}{2\bar{\Lambda}^3\,m_b^3}-\frac{64}{\bar{\Lambda}^2\,m_b^4}-\frac{25}{2\,\bar{\Lambda}\,m_b^5}+\frac{15}{m_b^6}+4\,\frac{\bar{\Lambda}}{m_b^7}\right\}
\end{aligned}$$

$$
\begin{aligned}
&+ S_H \left\{ \frac{48}{\bar{\Lambda}\, m_b^3} + \frac{69}{m_b^4} + 16\, \frac{\bar{\Lambda}}{m_b^5} - 9\, \frac{\bar{\Lambda}^2}{m_b^6} - 8\, \frac{\bar{\Lambda}^3}{m_b^7} \right\} \\
&- \frac{45\, \bar{\Lambda}}{2\, m_b^3} - \frac{212\, \bar{\Lambda}^2}{9\, m_b^4} - \frac{131\, \bar{\Lambda}^3}{18\, m_b^5} - \frac{5\, \bar{\Lambda}^4}{3\, m_b^6} - \frac{4\, \bar{\Lambda}^5}{9\, m_b^7}\,, \\
\mathcal{F}_S^3 \;=\;& \frac{2}{\bar{\Lambda}^4 m_b^4} \left(S_H - \bar{\Lambda}^2\right)^2 \left(2\bar{\Lambda}^2 + 3\bar{\Lambda}\, m_b - 2S_H\right) \times \\
&\left[ \frac{\pi^2}{3} + \ln^2\left(\frac{S_H - \bar{\Lambda}\, m_b - \bar{\Lambda}^2}{m_b\,(\bar{\Lambda} + m_b)}\right) - 2\, \ln^2\left(\frac{S_H - \bar{\Lambda}^2}{\bar{\Lambda}\, m_b}\right) \right. \\
&\quad \left. + 4\mathrm{Li}_2\left(\frac{m_b}{\bar{\Lambda}}\right) - 4\mathrm{Li}_2\left(\frac{\bar{\Lambda}\, m_b}{S_H - \bar{\Lambda}^2}\right) - 2\mathrm{Li}_2\left(\frac{\bar{\Lambda}^2 - S_H}{\bar{\Lambda}^2}\right) \right] \\
&+ \ln\left(\frac{S_H}{(\bar{\Lambda} + m_b)^2}\right) \left( S_H^3 \left\{ -\frac{2}{3\,\bar{\Lambda}^4\, m_b^4} - \frac{16}{3\,\bar{\Lambda}^3\, m_b^5} + \frac{2}{\bar{\Lambda}^2\, m_b^6} - \frac{4}{3\,\bar{\Lambda}\, m_b^7} \right\} \right. \\
&\qquad + S_H^2 \left\{ -\frac{3}{\bar{\Lambda}^3\, m_b^3} + \frac{8}{\bar{\Lambda}^2\, m_b^4} + \frac{13}{\bar{\Lambda}\, m_b^5} - \frac{2}{m_b^6} - 8\, \frac{\bar{\Lambda}}{m_b^7} \right\} \\
&\qquad \left. + S_H \left\{ \frac{6}{\bar{\Lambda}\, m_b^3} - \frac{4}{m_b^4} - 10\, \frac{\bar{\Lambda}}{m_b^5} - 8\, \frac{\bar{\Lambda}^2}{m_b^6} - 4\, \frac{\bar{\Lambda}^3}{m_b^7} \right\} \right) \\
&+ \ln\left(\frac{S_H - \bar{\Lambda} m_b - \bar{\Lambda}^2}{m_b\,(\bar{\Lambda} + m_b)}\right) \left(\frac{1}{3\,(\bar{\Lambda} + m_b)^2}\right) \\
&\qquad \left( S_H^3 \left\{ \frac{2}{\bar{\Lambda}^4\, m_b^2} - \frac{4}{\bar{\Lambda}^3\, m_b^3} - \frac{8}{\bar{\Lambda}^2\, m_b^4} \right\} \right. \\
&\qquad\quad + S_H^2 \left\{ -\frac{15}{\bar{\Lambda}^3\, m_b} - \frac{18}{\bar{\Lambda}^2\, m_b^2} + \frac{24}{\bar{\Lambda}\, m_b^3} + \frac{24}{m_b^4} \right\} \\
&\qquad\quad + S_H \left\{ \frac{78}{\bar{\Lambda}\, m_b} + \frac{42}{m_b^2} - 36\frac{\bar{\Lambda}}{m_b^3} - 24\frac{\bar{\Lambda}^2}{m_b^4} + \frac{24}{\bar{\Lambda}^2} \right\} \\
&\qquad\quad \left. + 10\frac{m_b}{\bar{\Lambda}} - 58\frac{\bar{\Lambda}}{m_b} - 26\frac{\bar{\Lambda}^2}{m_b^2} + 16\frac{\bar{\Lambda}^3}{m_b^3} + 8\frac{\bar{\Lambda}^4}{m_b^4} - 14 \right) \\
&+ \frac{1}{18\,(\bar{\Lambda} + m_b)^2} \left( S_H^3 \left\{ \frac{276}{\bar{\Lambda}^3\, m_b^3} + \frac{318}{\bar{\Lambda}^2\, m_b^4} - \frac{8}{\bar{\Lambda}\, m_b^5} + 34\, \frac{1}{m_b^6} + 80\, \frac{\bar{\Lambda}}{m_b^7} \right\} \right. \\
&\qquad + S_H^2 \left\{ -\frac{276}{\bar{\Lambda}^3\, m_b} - \frac{1218}{\bar{\Lambda}^2\, m_b^2} - \frac{1953}{\bar{\Lambda}\, m_b^3} - 1146\, \frac{1}{m_b^4} - 117\, \frac{\bar{\Lambda}}{m_b^5} \right. \\
&\qquad\qquad \left. + 126\, \frac{\bar{\Lambda}^2}{m_b^6} + 72\, \frac{\bar{\Lambda}^3}{m_b^7} \right\} \\
&\qquad + S_H \left\{ \frac{348}{\bar{\Lambda}^2} + \frac{3432}{m_b^2} + 3306\, \frac{\bar{\Lambda}}{m_b^3} + 894\, \frac{\bar{\Lambda}^2}{m_b^4} \right. \\
&\qquad\qquad \left. - 684\, \frac{\bar{\Lambda}^3}{m_b^5} - 594\, \frac{\bar{\Lambda}^4}{m_b^6} - 144\, \frac{\bar{\Lambda}^5}{m_b^7} - \frac{1602}{\bar{\Lambda}\, m_b} \right\}
\end{aligned}
$$

$$+ 143\,\frac{m_b}{\bar{\Lambda}} + 110 - 869\,\frac{\bar{\Lambda}}{m_b} - 1946\,\frac{\bar{\Lambda}^2}{m_b^2} - 1691\,\frac{\bar{\Lambda}^3}{m_b^3}$$
$$- 742\,\frac{\bar{\Lambda}^4}{m_b^4} - 199\,\frac{\bar{\Lambda}^5}{m_b^5} - 46\,\frac{\bar{\Lambda}^6}{m_b^6} - 8\,\frac{\bar{\Lambda}^7}{m_b^7}\Bigg)\,. \tag{4.18}$$

Figure 4.6 shows the squared hadronic invariant mass spectra from $b$-quark decay. The spectra in the Born approximation in Figure 4.6(a) and (b) are normalized with $\Gamma_0$, and the spectra with radiative corrections with $\Gamma$. The spectra in Figure 4.6(a) agree with the results presented in [4]. The variable in [4] is the scaled squared hadronic invariant mass, which is defined as $\hat{s}_H \equiv S_H/m_b^2$. We draw the squared hadronic invariant mass spectra with respect to $S_H$ referring to the result in [4]. The location of the peak in [4] is $\hat{s}_H \sim 0.11$, which agrees with the location of the peak in Figure 4.6, which is $S_H \sim 0.11 \times m_b^2\ GeV^2 \sim 2.53\ GeV^2$, and $m_b = 4.8\ GeV$. The effect of the radiative corrections is clearly observed in Figure 4.6. In Figure 4.6(b) the spectra are all normalized by $\Gamma_0$.

In Figure 4.7, we present the hadronic invariant mass $M_H$ spectra. Unlike the squared hadronic invariant mass spectrum, the hadronic invariant mass spectrum is concentrated in a smaller region of $M_H$. The effect of the radiative corrections is large both in the squared hadronic invariant mass spectrum and in the hadronic invariant mass spectrum. The change in the hadronic invariant mass spectrum by varying $\alpha_s$ from $\alpha_s = 0.22$ to $\alpha_s = 0.25$ is more visible, whereas the change of the value of $\alpha_s$ does not affect much the electron energy spectrum or the leptonic invariant mass spectrum.

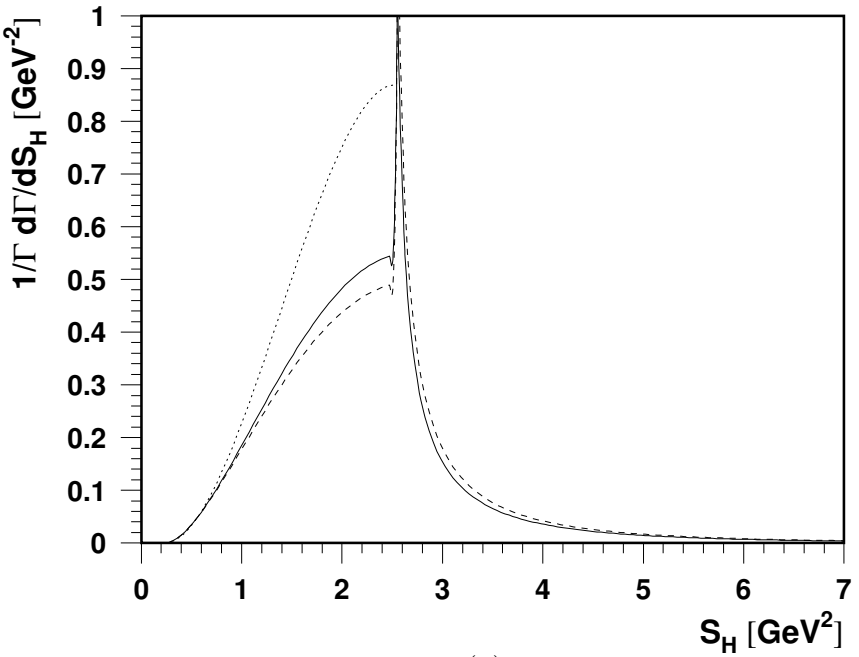


(a)

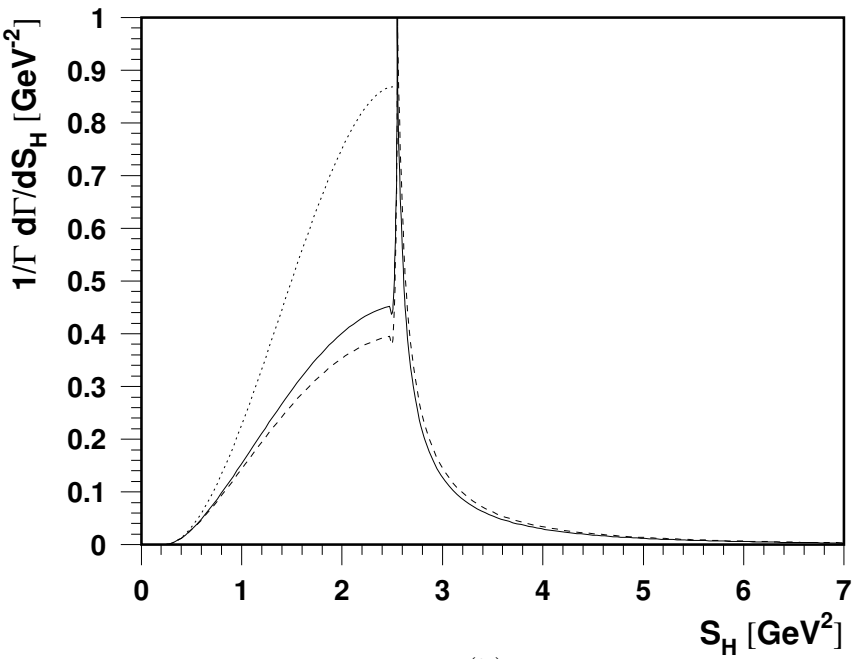


(b)

Figure 4.6: (a) The squared hadronic invariant mass $S_H$ spectrum in units of $\Gamma$. The dotted line shows the Born approximation of the squared hadronic invariant mass spectrum. The solid line displays the spectrum with radiative corrections at $\alpha_s = 0.22$, and the dashed line at $\alpha_s = 0.25$. (b) The squared hadronic invariant mass $S_H$ spectrum normalized with $\Gamma_0$. The dotted line shows the Born approximation of the spectrum. The solid line displays the spectrum with the radiative corrections at $\alpha_s = 0.22$, and the dashed line at $\alpha_s = 0.25$.

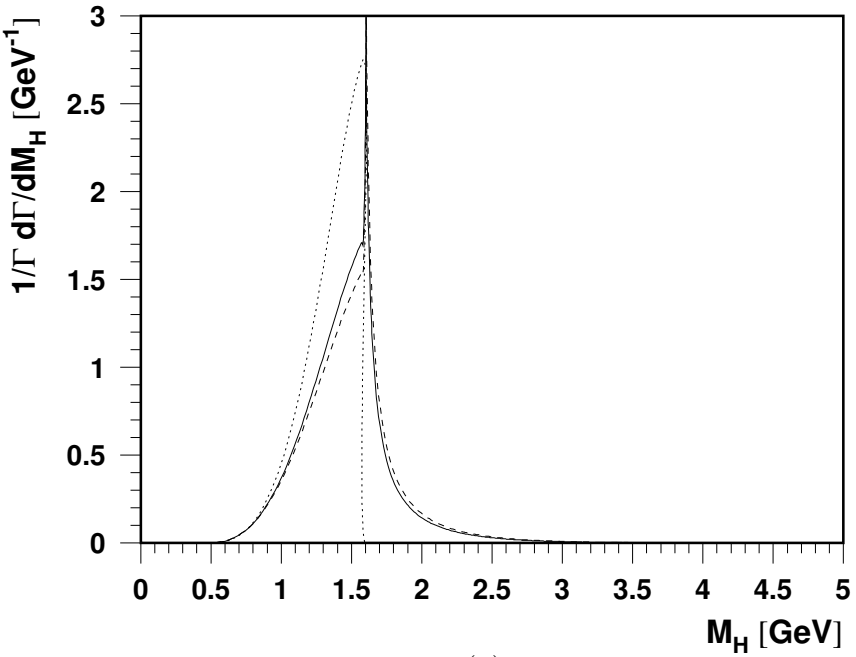


(a)

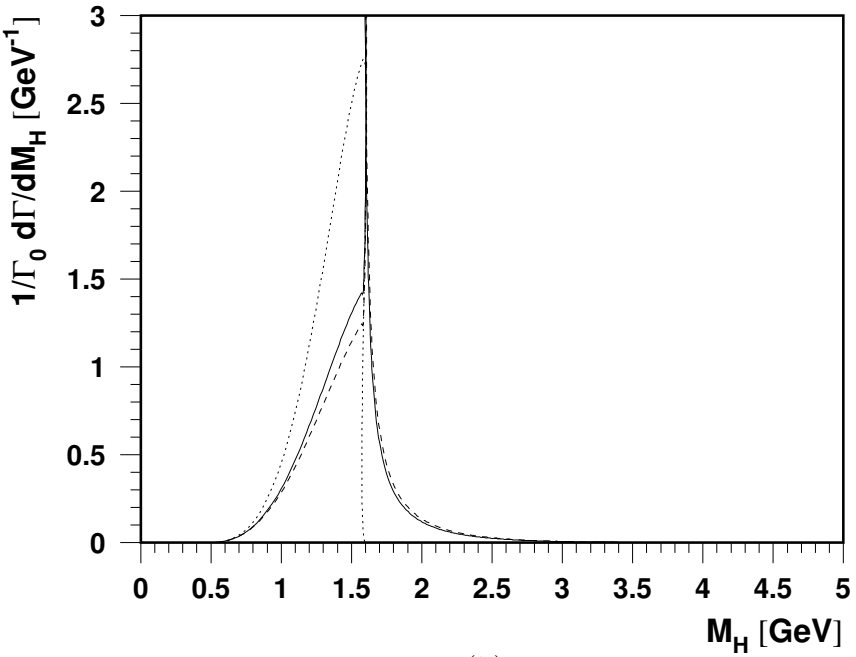


(b)

Figure 4.7: (a) The hadronic invariant mass $M_H$ spectrum in units of $\Gamma$. The dotted line shows the spectrum in the Born approximation. The solid line displays the spectrum with the radiative corrections at $\alpha_s = 0.22$, and the dashed line at $\alpha_s = 0.25$. (b) The hadronic invariant mass $M_H$ spectrum normalized with $\Gamma_0$. The dotted line shows the spectrum in the Born approximation. The solid line displays the spectrum with radiative corrections at $\alpha_s = 0.22$, and the dashed line at $\alpha_s = 0.25$.

# Chapter 5

# $B$-meson decay in the Parton model

## 5.1 Parton model and $B$-meson decay

The parton model describes hadrons as consisting of massless partons, which can be identified with quarks and gluons. The parton model is successful in explaining lepton–hadron scatterings in the Bjorken limit $-q^2 = Q^2 \to \infty$ with fixed Bjorken scaling variable $x \equiv \frac{-q^2}{2m_p\nu}$. For the case of $B$-meson decay, we do not consider the limit $W^2 = Q^2 \to \infty$, but the Light–Cone limit $y^2 \sim 0$, where $y$ is the separation of two currents. In the Light–Cone limit it is possible to employ the Light–Cone expansion of the current commutator. In Section 2.3 we have shown that the structure function $W_{\mu\nu}$ gets a dominant contribution from the region $0 \leq y^2 \leq \frac{1}{W^2}$. Therefore, when $W^2$ is large enough, the Light–Cone expansion is a good approximation. The structure function $W^{\mu\nu}$ can be expressed with a single distribution function after the Light–Cone expansion, which is similar to the case of the parton model. In the case of large $W^2$, the parton model can be applied to $B$-meson decay. The theoretical explanation of the Light–Cone expansion of the $B$-meson matrix is explained in Section 2.3.

The parton model for lepton–hadron scatterings is explained in Section 5.1.1 and application of the parton model to $B$-meson decay in Section 5.1.2. Explanation of the distribution function and the determination of parameters for the distribution function are also described in Section 5.1.2. Various spectra of $B$-meson decay are displayed in Section 5.2.

### 5.1.1 Parton model

The parton model [64] suggests that hadrons may be regarded at short distances as a composition of point–like constituents (partons) which are assumed to be almost free. Lepton–hadron scatterings, which are deep inelastic processes, are well described by the parton model, so we take the well–known lepton–nucleon structure functions in the parton model [65, 64] as the introductory example.

In the parton model, the differential cross–section of a process $A + B \to a + b + X$ has the general form

$$d\sigma[A(p_A) + B(p_B) \to a(p_a) + b(p_b) + X] = \int dx' d\hat{\sigma}_0[A'(x'p_A) + B(p_B) \to a(p_a) + b(p_b) + X]\, f(x')\,, \tag{5.1}$$

where $d\hat{\sigma}_0[A'(x'p_A) + B(p_B) \to a(p_a) + b(p_b) + X]$ is the parton differential cross–section in the Born approximation and $f(x)$ is the distribution function. $A'$ is the parton from the hadron $A$, and $a$ is the parton after the scattering.

For a specific example, we consider lepton–nucleon scatterings. Figure 5.1 shows lepton–nucleon scatterings in the parton model. The momentum of the nucleon is $p$. The momentum of the scattered parton in the nucleon is $\xi p$, which takes momentum from the nucleon by a fraction $\xi$. The momenta of the in–coming and out–going leptons are denoted by $k$ and $k'$ respectively, and the momentum transfer to the parton is $q = k - k'$.

The differential cross–section of lepton–hadron scatterings is conventionally expressed with a hadronic tensor and a leptonic tensor

$$d\hat{\sigma}_0 \;\sim\; \frac{d^3k'}{(2\pi)^3 2k'^0}\, W^{\mu\nu} L_{\mu\nu}\,. \tag{5.2}$$

Referring to Eq.(5.1), the hadronic tensor $W^{\ell}_{\mu\nu}$ for lepton–nucleon scatterings reads

$$W^{\ell}_{\mu\nu} = \int_0^1 d\xi\, \mathrm{K}^{\ell}_{\mu\nu}(\xi) f(\xi)\,, \tag{5.3}$$

where $\mathrm{K}^{\ell}_{\mu\nu}(\xi)$ is the parton tensor [66]

$$\begin{aligned} \mathrm{K}^{\ell}_{\mu\nu}(\xi) &= \frac{1}{4\,\xi\, m_p} \sum_{spin} \frac{d^3p'}{(2\pi)^2\, 2p'_0}\, (2\pi)^3 \delta^{(4)}(p' - \xi p - q) \times \\ &\quad \langle \xi p, \sigma | J^{em}_{\mu}(0) | p', \sigma' \rangle \langle p', \sigma' | J^{em}_{\nu}(0) | \xi p, \sigma \rangle \\ &= \frac{1}{4\,\xi\, m_p}\, \frac{1}{2\, p'_0}\, \delta(p'_0 - \xi p_0 - q_0) \sum_{spin} \bar{u}(\xi p) \gamma_\mu u(p') \bar{u}(p') \gamma_\nu u(\xi p)\,. \end{aligned} \tag{5.4}$$

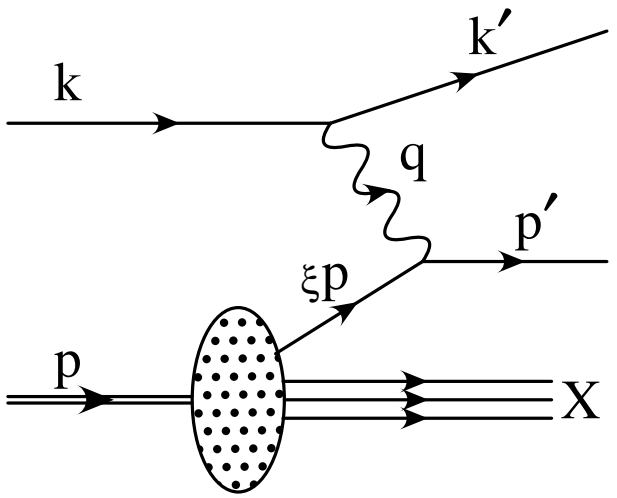


Figure 5.1: Lepton–nucleon scattering: Deep Inelastic Scatterings.

When we keep the partons massless, the $\delta$–function in Eq.(5.4) is calculated as

$$\delta(p_0' - \xi p_0 - q_0)\,\frac{1}{2p_0'} = \theta(\xi p_0 + q_0)\,\frac{\delta(\xi - x)}{2m_p\nu}\,, \tag{5.5}$$

where $x$ is the Bjorken scaling variable $x \equiv -\frac{q^2}{2\,m_p\nu} = \frac{Q^2}{2m_p\nu}$ and $\nu \equiv \frac{p\cdot q}{m_p}$.

After applying Eq.(5.5) and summing Eq.(5.4) over spin, the parton tensor reads

$$\mathrm{K}^{\ell}_{\mu\nu}(\xi) = \delta(\xi - x)\left(\frac{\xi}{\nu}\,\frac{p_\mu p_\nu}{m_p^2} - \frac{1}{2m_p}\,g_{\mu\nu} + \cdots\right). \tag{5.6}$$

Hence, using the hadronic tensor $W^{\ell}_{\mu\nu}$ in Eq.(5.3) for lepton–nucleon scatterings, it is expressed in terms of the Bjorken scaling variable $x$ as

$$W^{\ell}_{\mu\nu} = \frac{xf(x)}{\nu}\,\frac{p_\mu p_\nu}{m_p^2} - \frac{f(x)}{2m_p}\,g_{\mu\nu} + \cdots\,. \tag{5.7}$$

*QCD* corrections in the parton model are carried out by calculating *QCD* corrections to the parton level Born diagrams. While calculating *QCD* corrections in the parton model, one has to pay attention to infrared and ultraviolet divergences and remove them by renormalization. However, mass or collinear singularities remain. The collinear singularities are subtracted and combined by the distribution function.

### 5.1.2 $B$-meson decay in view of the Parton model

We have shown in Section 2.3 that the $B$-meson structure functions $W_i$'s can be expressed with a single distribution function $f(x)$ and the scaling variables $\chi_\pm$ in the Light–Cone expansion

$$\chi_\pm = \frac{W \cdot P_B \pm \sqrt{(W \cdot P_B)^2 - M_B^2(W^2 - m_f^2)}}{M_B^2}, \tag{5.8}$$

which makes it possible to apply the parton model to $B$-meson decay in the range $1\ GeV^2 \leq W^2$.

$B$-meson decay in the parton model description is displayed in Figure 5.2. The $b$-quark extracted from the $B$-meson with momentum $P_B$ has momentum $p_b = \chi P_B$, and through the weak interaction it decays into a light quark – a $u$-quark, for example – and a lepton pair with momentum $W$.

When we employ the parton model, we should be aware of mass or collinear singularities in the $QCD$ corrections, which stem from the integration region when the in–coming parton is massless and the emitted gluon moves collinearly with the parton after the emission. Collinear singularities are observed in the result Eq.(3.76) in Chapter 3, when the $b$-quark mass is set to 0. During the whole calculation of $QCD$ corrections, we have kept a non–vanishing mass for the $b$-quark, $m_b$. For $QCD$ corrections to the hadronic tensor, we replace the $b$-quark momentum with $\chi P_B$, which means that the $b$-quark is a parton in the $B$-meson. We let the mass of $b$-quark run by defining $p_b = \chi P_B$ and $m_b^2 = \chi^2 M_B^2$.

When the parameter $\chi$ of the distribution function $f(\chi)$ goes to zero, the mass of the $b$-quark also drops to zero. The distribution function, however, vanishes at $\chi = 0$ and $\chi = 1$, and therefore the collinear singularities are removed smoothly by the distribution function.

The difference between lepton–nucleon scatterings and $B$-meson decay is the range of leptonic invariant mass $W^2$ for $B$-meson decay and $Q^2 \equiv -q^2$ for lepton–nucleon scatterings. The $Q^2$ range of lepton–nucleon scatterings is determined by the momentum difference of the in–coming lepton and the out–going lepton. The maximal value of the leptonic invariant mass $W^2$ for $B$-meson decay is smaller than that for lepton–nucleon scatterings $Q^2$, which reaches, for example, $Q^2 = 160\ GeV^2$ at BCDMS at CERN. The value of $W^2$ for the $B$-meson decay cannot exceed the mass of the $b$-quark and therefore varies between $0 \leq W^2 \leq m_b^2$. The estimated $b$-quark pole mass is $4.6\ GeV \leq m_b \leq 5.1\ GeV$.

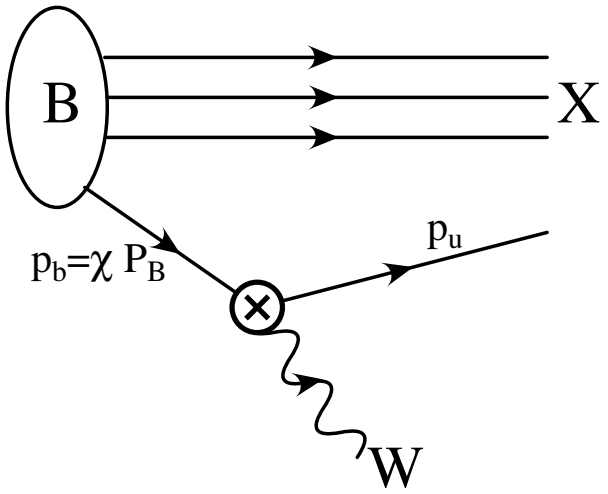


Figure 5.2: $B$-meson decay in the parton model.

### 5.1.3 Distribution Function

It is shown in Section 2.3 that the $B$-meson structure functions are expressed with a single distribution function $f(\chi)$ in the Light–Cone limit in terms of the scaling variable $\chi_\pm$. The interpretation of the distribution function of $f(\chi)$ is the probability to find a $b$-quark with momentum $\chi P_B$ inside a $B$-meson with momentum $P_B$, incorporating long–distance behavior. The properties of the distribution function are determined by experimental results, as the long–distance behavior cannot be calculated explicitly.

Heavy Quark Effective Theory (HQET) provides important parameters, which are measured experimentally. We exploit these experimental results of the HQET parameters to determine the distribution function.

In Section 2.3 we defined the distribution function $f(x)$ as

$$\begin{aligned} f(x) &\equiv \int d(y\cdot P_B)\, e^{i\,x\cdot(y\cdot P_B)}\, \mathcal{F}_0(y\cdot P_b) \\ &= \frac{1}{4\,\pi\, M_B^2} \int d(y\cdot P_B)\, e^{i\,x\cdot(y\cdot P_B)}\, \langle B|\bar{b}(0)\, \not{P}_B\,(1-\gamma_5)\, b(y)|B\rangle|_{y^2=0} \end{aligned} \quad (5.9)$$

In Heavy Quark Effective Theory (HQET), the $b$-quark field $b(x)$ is represented by the velocity dependent $b$-quark field $b_v$ and the relation between $b(x)$ and $b_v(x)$ reads to first order in $1/m_b$ [13]

$$b(x) \;=\; e^{-i\,m_b\,v\cdot x}\left[1+\frac{i\not{D}}{2\,m_b}\right]b_v(x)\,. \tag{5.10}$$

This leads to an Operator Product Expansion as in [67, 69]

$$\begin{aligned}&\bar{b}(0)\,\gamma^\beta\,(1-\gamma_5)\,b(x) = \\ &e^{-i\,m_b\,(v\cdot x)}\sum_{n=0}^{\infty}\frac{(-i)^n}{n!}\,x_{\mu_1}\cdots x_{\mu_n}\,\bar{b}_v(0)\,\gamma^\beta\,(1-\gamma_5)\mathcal{S}[k^{\mu_1}\,\cdots k^{\mu_n}]b_v(0) \\ &+\mathcal{O}\left(\frac{1}{m_b}\right),\end{aligned} \tag{5.11}$$

where $k_\mu = iD_\mu = i(\partial_\mu - ig_sA_\mu)$, and $\mathcal{S}$ denotes a symmetrization. The matrix element $\langle B|\bar{b}(0)\,\gamma^\beta\,(1-\gamma_5)\,b(y)\,|B\rangle$ is expressed in terms of $b_v$ as

$$\begin{aligned}&\langle B|\bar{b}(0)\,\gamma^\beta\,(1-\gamma_5)\,b(y)\,|B\rangle = \\ &2\left(C_{n0}\,P_B^\beta P^{\mu_1}\cdots P^{\mu_n}+\sum_{i=1}^{n}M_B^2C_{ni}\,g^{\beta\,\mu_i}P^{\mu_1}\cdots P^{\mu_{i-1}}P^{\mu_{i+1}}\cdots P^{\mu_n}\right) \\ &+\text{ terms with } g^{\mu_i\,\mu_j}\,.\end{aligned} \tag{5.12}$$

The terms with $g^{\mu_i\,\mu_j}$ can be omitted on the Light–Cone. Combining the equations we obtain

$$f(x)=\sum_{n=0}^{\infty}\frac{(-1)^n}{n!}\left(\sum_{i=0}^{n}C_{ni}\right)\delta^{(n)}\left(x-\frac{m_b}{M_B}\right). \tag{5.13}$$

Finally, we obtain the moment sum rule for the distribution function

$$M_n(m_b/M_B)=\sum_{i=0}^{n}C_{ni}\,, \tag{5.14}$$

where the $n$th moment about a point $\tilde{x}$ of the distribution function is defined by

$$M_n(\tilde{x})=\int_0^1 dx\,(x-\tilde{x})^n f(x)\,, \tag{5.15}$$

and $M_0(\tilde{x}) = C_{00} = 1$ by definition.

The coefficients $C_{ni}$ are estimated from HQET. The effective Lagrangian has the form

$$\mathcal{L}_{HQET} = \bar{b}_v iv\cdot D b_v + \bar{b}_v \frac{(iD)^2}{2\,m_b} b_v + \bar{b}_v \frac{g_s G_{\alpha\,\beta}\sigma^{\alpha\beta}}{4\,m_b} b_v + \mathcal{O}\left(\frac{1}{m_b^2}\right), \qquad (5.16)$$

where $g_s G^{\alpha\,\beta} = i[D^\alpha, D^\beta]$ is the gluon field–strength tensor. The matrix elements of local operators in full $QCD$ are related to those in HQET as written in [35, 70, 71, 72, 73] and the coefficients $C_{ni}$ can be expressed in terms of HQET parameters. The results in [67, 69] are

$$\begin{aligned} C_{10} &= \frac{5\,m_b}{3\,M_B} E_b(B) + \mathcal{O}(\Lambda^3_{QCD}/m_b^3)\,, \\ C_{11} &= \frac{2\,m_b}{3\,M_B} E_b(B) + \mathcal{O}(\Lambda^3_{QCD}/m_b^3)\,, \\ C_{20} &= \frac{2\,m_b^2}{3\,M_B^2} K_b(B) + \mathcal{O}(\Lambda^3_{QCD}/m_b^3)\,, \\ C_{21} &= C_{22} = 0\,, \end{aligned} \qquad (5.17)$$

and the dimensionless HQET parameters $K_b$ and $G_b$ read

$$\begin{aligned} K_b(B) &= -\frac{1}{2\,M_B}\,\langle B|\bar{b}_v\,\frac{(iD)^2}{2\,m_b^2}\,b_v|B\rangle\,, \\ G_b(B) &= -\frac{1}{2\,M_B}\,\langle B|\bar{b}_v\,\frac{g_s\,G_{\alpha\,\beta}\,\sigma^{\alpha\,\beta}}{4\,m_b^2} b_v|B\rangle\,, \end{aligned} \qquad (5.18)$$

and $E_b(B) = K_b(B) + G_b(B)$.

The parameter $K_b(B)$ measures the kinetic energy of $b$-quarks inside $B$-mesons, and the parameter $G_b(B)$ the chromo–magnetic energy due to the spin coupling between the $b$-quark and the light constituents in the $B$-meson. The sum rule in Eq.(5.14) determines the mean value $\mu$ and the variance $\sigma^2$ of the distribution function up to order $(\Lambda_{QCD}/m_b)^2$. From the definition in Eq.(5.15) we obtain

$$\begin{aligned} \mu &\equiv M_1(0) = \tilde{x} + M_1(\tilde{x})\,, \\ \sigma^2 &\equiv M_2(\mu) = M_2(\tilde{x}) - M_1^2(\tilde{x})\,, \end{aligned} \qquad (5.19)$$

and subsequently,

$$\begin{aligned} \mu &= \frac{m_b}{M_B}\,[1 + E_b(B)]\,, \\ \sigma^2 &= \left(\frac{m_b}{M_B}\right)^2 \left[\frac{2\,K_b(B)}{3} - E_b^2(B)\right]. \end{aligned} \qquad (5.20)$$

In Heavy Quark Effective Theory (HQET) the masses of $B$ mesons are expanded in powers of the $b$-quark mass $m_b$ [75]

$$\begin{aligned} M_B &= m_b + \bar{\Lambda} - \frac{\lambda_1 + 3\lambda_2}{2\, m_b}\,, \\ M_{B^*} &= m_b + \bar{\Lambda} - \frac{\lambda_1 - \lambda_2}{2\, m_b}\,, \end{aligned} \tag{5.21}$$

and the parameter $\lambda_1$ characterizes the mass shift due to the kinetic operator, and $\lambda_2$ the effect of chromo–magnetic interaction of the heavy quark and the light quark inside the $B$-meson. $\lambda_1$ and $\lambda_2$ read

$$\begin{aligned} \lambda_1 &\equiv \frac{1}{2\, M_B} \langle B \,|\, \bar{h} (iD)^2 h \,|\, B \rangle\,, \\ \lambda_2 &\equiv \frac{1}{12\, M_B} \langle B \,|\, \bar{h}\, g_s\, G_{\alpha\beta}\, \sigma^{\alpha\beta}\, h \,|\, B \rangle\,, \end{aligned} \tag{5.22}$$

and in terms of $K_b(B)$ and $E_b(B)$

$$\begin{aligned} \lambda_1 &= -2\, m_b^2\, K_b\,, \\ \lambda_2 &= -\frac{2}{3}\, m_b^2 G_b\,. \end{aligned} \tag{5.23}$$

The parameters $\lambda_1$, $\lambda_2$, and $\bar{\Lambda}$ are measured from experiment. $\lambda_2$ is directly measured from the mass difference between $B$ and $B^*$, whereas $\lambda_1$ still contains large uncertainty. The latest measurements of $\bar{\Lambda}$ and $\lambda_1$ at CLEO are [79]

$$\bar{\Lambda} = 0.39 \pm 0.03\,(stat) \pm 0.06\,(syst) \pm 0.12\,(th)\ GeV\,, \tag{5.24}$$

$$\lambda_1 = -0.25 \pm 0.02\,(stat) \pm 0.05\,(syst) \pm 0.14\,(th)\ GeV^2\,, \tag{5.25}$$

and we use $\lambda_1 = -0.24\ GeV^2$ and $\lambda_2 = 0.12\ GeV^2$.

One can try many possible distribution functions respecting the constraints in Eq.(5.20) and Eq.(5.23). The one pioneering model was suggested by Peterson *et al.* [78], which was proposed to explain hadronization, that is, the transition from partonic states into physical hadronic states. One assumes that

$$f_{ptr}(x) = N_{ptr} \frac{1}{x[1 - (1/x) - \epsilon_Q/(1-x)]^2}\,, \tag{5.26}$$

with the normalization constant $N_{ptr}$. The distribution function by Peterson *et al.* depends on one parameter, which is correlated to the mean value of the

distribution. So, we have less freedom for the variance of the distribution function in this case.

We introduce the distribution function suggested by Jin and Paschos [33] and focus on it. The distribution function by Jin and Paschos reads

$$f_{jp}(x) \;=\; N_{jp}\,\frac{x\,(1-x)}{(x-b)^2+a^2}\,, \tag{5.27}$$

where the two parameters $a$ and $b$ are to be determined by experimental results using the relation in Eq.(5.20) and Eq.(5.23). The constant $N_{jp}$ in Eq.(5.27) is determined from

$$\int_0^1 dx\, f(x) \;=\; 1\,. \tag{5.28}$$

Likewise, $N_p$ in Eq.(5.26) is determined by using Eq.(5.28).

The total $b$-quark decay rate

$$\Gamma_{b\to ue\bar{\nu}} \sim \frac{G_F^2\,|V_{ub}|^2\,m_b^5}{16\,\pi} \tag{5.29}$$

is dependent on the mass of the $b$-quark, which is not directly measurable. We replace the $b$-quark mass with $\chi\,M_B$ in the radiative corrections and let the $b$-quark mass run $p_b^2 = \chi^2\,M_B^2$. There are two approaches to handle the $b$-quark mass in the parton model. One is to keep the $b$-quark mass $m_b^2$ and give the $b$-quark momentum $p_b = (m_b, \vec{p}_{bT}, p_{b\,z})$, and the other is to let the $b$-quark mass change $p_b^2 = \chi^2\,M_B^2$ and give the $b$-quark momentum $p_b = \chi\,P_B$. For the latter case $p_b = (\chi\,M_B, \vec{0})$ in the $B$-meson rest frame.

The estimation of $K_b$ and $G_b$ from the experimental data $\lambda_1$ and $\lambda_2$ using Eq.(5.20) and Eq.(5.23) depends on the $b$-quark mass, which contains large uncertainties. Therefore the estimation of $K_b$ and $G_b$ from the definition of HQET depends on the reference $b$-quark mass, and this reference $b$-quark mass controls the parameters $a$, which is mainly responsible for the variance of the distribution function, and $b$, which is related with the ratio between the $b$-quark mass and the $B$-meson mass. Therefore, the reference $b$-quark mass has the main influence on the mean value of the distribution function, and the distribution function shows the most probability to find a $b$-quark with the reference $b$-quark mass.

There are in general several mass definitions. Two representative definitions are the $\overline{MS}$ mass and the pole mass. The $\overline{MS}$ mass $\overline{m_b}(\overline{m_b})$ is determined in the $\overline{MS}$–renormalization scheme taking the renormalization scale $\mu = \overline{m_b}$. The pole–mass $m_b$ is the pole of the quark propagator. Several groups have calculated the $b$-quark mass using different methods, and the latest status of the $b$-quark

| $m_b\,(GeV)$ | $\mu$ | $\sigma^2$ | $a$ | $b$ |
|---|---|---|---|---|
| 4.65 | 0.878 | 0.0028636 | 0.00566 | 0.889 |
| 4.80 | 0.907 | 0.0028640 | 0.00417 | 0.917 |
| 4.95 | 0.935 | 0.0028643 | 0.00298 | 0.946 |

Table 5.1: $a$ and $b$ at various $m_b$ for the Jin and Paschos model.

| $m_b\,(GeV)$ | $\mu$ | $\sigma^2$ | $\epsilon_Q$ | $\sigma^2(f_p(x))$ |
|---|---|---|---|---|
| 4.65 | 0.878 | 0.0028636 | 0.002016 | 0.0141495 |
| 4.80 | 0.907 | 0.0028640 | 0.000910 | 0.0184300 |
| 4.95 | 0.935 | 0.0028643 | 0.00032 | 0.0073793 |

Table 5.2: $\epsilon_Q$ at various $m_b$ for the Peterson *et al.* model.

$\overline{m_b}(\overline{m_b})$ mass ranges from 4.0 $GeV$ to 4.5 $GeV$ and the corresponding range of the pole mass $m_b$ is $4.6 - 5.1$ $GeV$ [27].

A recent result of $\overline{m_b}(\overline{m_b})$ using the SVZ sum rule is [80]

$$\overline{m_b}(\overline{m_b}) = 4.191 \pm 0.051\ GeV\,, \tag{5.30}$$

and it show a good agreement with the results in [81, 82, 83, 84, 85, 86, 87, 88] and this result corresponds to the pole mass [89, 90, 91, 92]

$$\begin{aligned} m_b^{2-loop} &= 4.65 \pm 0.06\ GeV\,, \\ m_b^{3-loop} &= 4.82 \pm 0.06\ GeV\,. \end{aligned} \tag{5.31}$$

We adopt $m_b = 4.80 \pm 0.15\,GeV$ which is the mean value of the recent results.

Employing the experimental results $\lambda_1 = -0.24\ GeV^2$ [79] and fixing $\lambda_2 = \frac{(M_{B^*}-M_B)^2}{4} = 0.12\ GeV^2$ [69], we obtain the corresponding $\mu$, $\sigma^2$, $a$ and $b$ determined from Eq.(5.20) and Eq.(5.23) and they are in Table 5.1.

In the same way, we can determine the parameter $\epsilon_Q$ in Eq.(5.26). In this case we cannot find an $\epsilon_Q$ which satisfies both the mean value and the variance in Eq.(5.20) for certain $\lambda_1$, $\lambda_2$ and $m_b$. We determine the parameter $\epsilon_Q$ in such a way that the mean value of the distribution function Eq.(5.26) is the same as the mean value from Eq.(5.20) with $\lambda_1 = -0.25\ GeV^2$ and $\lambda_2 = 0.12\ GeV^2$ at a certain $m_b$. The results are found in Table 5.2.

The value $\sigma^2(f_p(x))$ is the variance of the distribution function Eq.(5.26) with the corresponding $\epsilon_Q$, and $\sigma^2$ is determined by the experimental results $\lambda_1$ and $\lambda_2$

using Eq.(5.20). The two variances are different whereas the distribution function Eq.(5.26) has the same mean value in Table 5.2 with the corresponding $\epsilon_Q$. In the following sections we present various spectra with this information on the distribution function.

## 5.2 Spectra from $B$-meson decay

In this section we present various kinds of spectra from $B$-meson decay with the use of the Light–Cone expansion and the parton model. We present both the Born approximation of the spectrum and the radiatively corrected spectrum.

The Born approximation of $B$-meson decay in the parton model with scaling variables $\chi_\pm$ is obtained by inserting Eq.(2.34) into Eq.(2.11) and reads [33]

$$\begin{aligned}\frac{d^3\Gamma}{dE_e\, dW^2\, dW^0} &= \frac{G_F^2\,|V_{ub}|^2}{4\,\pi^2\,M_B}\,\frac{W^0-E_e}{\sqrt{(W^0)^2-W^2+m_f^2}}\times \\ &\Big(f(\chi_+)\big(2\chi_+E_eM_B-W^2\big)-\big(\chi_+\to\chi_-\big)\Big)\,, \qquad (5.32)\end{aligned}$$

and

$$\chi_\pm = \frac{W\cdot P_B \pm \sqrt{(W\cdot P_B)^2-M_B^2(W^2-m_f^2)}}{M_B^2}\,, \qquad (5.33)$$

where $m_f = m_u = 0$. The contribution from $\chi_-$ is negligible and therefore we keep only the terms with $\chi_+$. The electron energy spectrum is directly obtained by integrating Eq.(5.32) over $W^0$ and $W^2$.

The contribution from the radiative corrections $d\Gamma^{rad}$ is added by replacing the four–momentum of the $b$-quark by $\chi P_B$ in the $QCD$ corrections $d\Gamma^{\alpha_s}$ of the $b$-quark decay in Chapter 3 and reads

$$d\Gamma^{rad} = \int_0^1 d\chi d\Gamma^{\alpha_s}\,. \qquad (5.34)$$

We generate the Born approximation of the spectrum and compare it with the spectrum with the $QCD$ corrections of order $\alpha_s$. The analyses are carried out with the $b$-quark masses $m_b = 4.65,\, 4.80,\, 4.95\ GeV$. The uncertainty in

the $b$-quark mass is taken over by the parameters $a$ and $b$ of the distribution function as noted in Section 5.1.3. The parameter $a$ governs the variance of the distribution function and the $b$ parameter its mean value.

### 5.2.1 Electron Energy Spectrum

The electron energy spectrum from $b$-quark decay and from $B$-meson decay are compared in Figure 5.3. We take $m_b = 4.80\ GeV$, and the corresponding values of $a$ and $b$ for the distribution function suggested by Jin and Paschos in Eq.(5.27) are $a = 0.00417$ and $b = 0.917$, which are displayed in Table 5.1. The dotted line in Figure 5.3 is the electron energy spectrum from $b$-quark decay in the Born approximation, and the dot–dashed line the spectrum with radiative corrections at $\alpha_s = 0.22$. The Born approximation of the electron energy spectrum from $B$-meson decay and the spectrum with radiative corrections at $\alpha_s = 0.22$ are depicted by the dashed line and by the solid line in Figure 5.3, respectively.

In Figure 5.3 one can observe the difference in the end point region of the electron energy between the spectrum from $B$-meson decay and that from $b$-quark decay. The electron energy spectrum from $B$-meson decay extends until $E_e = \frac{M_B}{2}$, whereas the spectrum from $b$-quark decay ends up at $E_e = \frac{m_b}{2}$. The effect of $QCD$ corrections is smaller in the case of $B$-meson decay than in the case of $b$-quark decay. The contribution of $QCD$ corrections to $B$-meson decay is apparent for the total decay rate $\Gamma_0 \rightarrow \Gamma$ but not for the electron energy spectrum.

We compare the electron energy spectrum at $m_b = 4.65\ GeV$ and $m_b = 4.80\ GeV$ in Figure 5.4. In Figure 5.4(a) and Figure 5.4(b) the dotted line and the solid line are the Born approximation of the spectrum and the radiatively corrected spectrum with $a = 0.00417$ and $b = 0.917$ respectively. The dashed lines in Figure 5.4(a) and Figure 5.4(b) are the Born approximation of the spectrum with $a = 0.00566$ and $b = 0.889$, and the dot–dashed lines the spectrum with $QCD$ corrections. The strong coupling constant is $\alpha_s = 0.22$ for Figure 5.4(a) and $\alpha_s = 0.25$ for Figure 5.4(b).

In Figure 5.4 we can clearly observe that the effect of $QCD$ corrections on the electron energy spectrum is not significant. The change of the strong coupling constant $\alpha_s = 0.22 \rightarrow \alpha_s = 0.25$ does not result in a big change in the spectrum. The $QCD$ corrected spectra at $\alpha_s = 0.22$ in Figure 5.4(a) and at $\alpha_s = 0.25$ in Figure 5.4(b) are almost overlapped with the spectra of the Born approximation, but the change of the $b$-quark mass gives non–trivial effects on the electron energy spectrum. The peak of the spectrum moves depending on the $b$ value, which is dependent on the ratio of $b$-quark mass to $B$-meson mass.

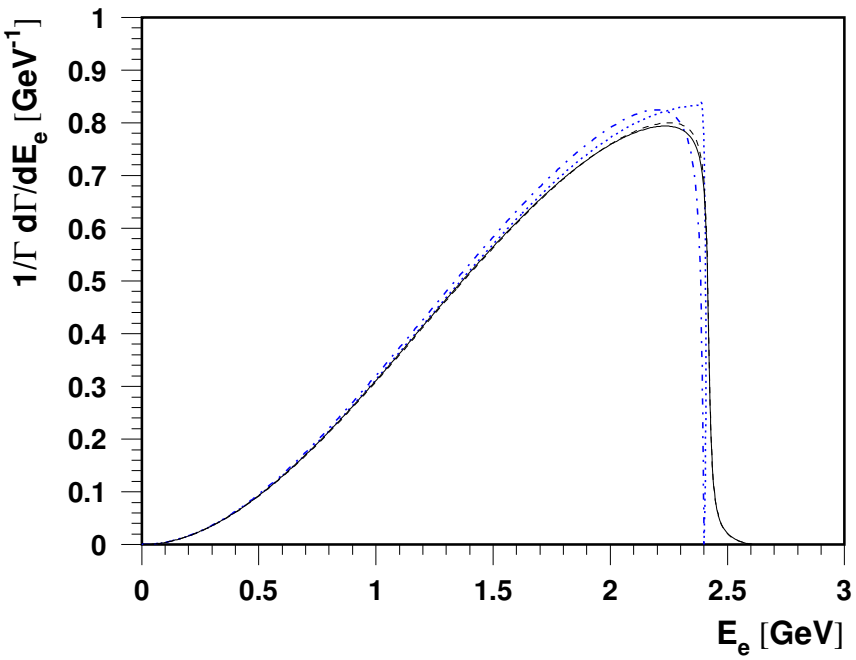


Figure 5.3: The electron energy spectrum from $B$-meson decay is compared with that from $b$-quark decay. The $b$-quark mass is assumed to be $m_b = 4.80\ GeV$.

In Figure 5.5 the spectra from $B$-meson decay with various $a$ and $b$ are compared, which correspond to $m_b = 4.65\ GeV$, $m_b = 4.80\ GeV$, and $m_b = 4.95\ GeV$. Figure 5.5(a) shows the Born approximation of the electron energy spectrum at various $m_b$ values. Comparison of the electron energy spectrum at the three $m_b$ values and the corresponding $a$ and $b$ values is found in Table 5.1.

The shape of the spectra depends highly on the values of $a$ and $b$, i.e. on the $b$-quark mass, which shows that the effect of uncertainty in the $b$-quark mass is not trivial for the study of $B$-meson decay. As one can observe in Figure 5.5, the curves are shifted from left to right as one changes from $m_b = 4.65\ GeV$ to $m_b = 4.95\ GeV$. The electron energy spectra at $\alpha_s = 0.22$ are shown in Figure 5.5(b). The inclusion of $QCD$ corrections with $\alpha_s = 0.22$ does not influence the shape of the electron energy spectra from $B$-meson decay, which is observed in Figure 5.5(b).

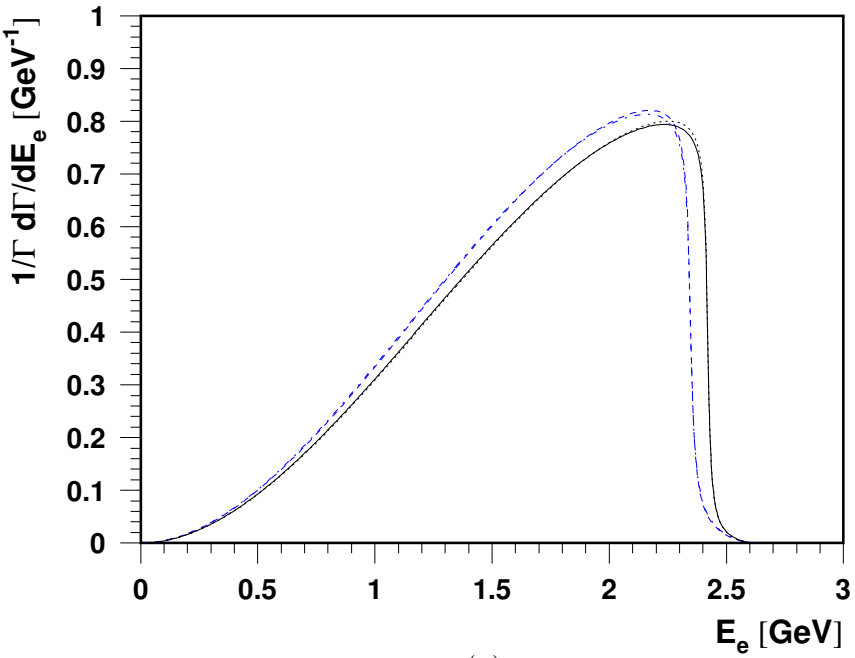


(a)

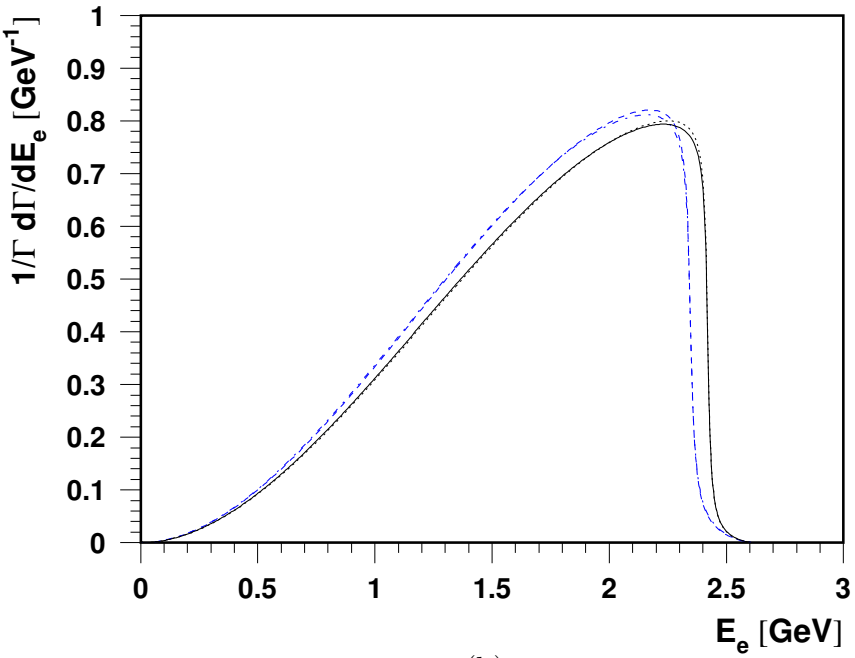


(b)

Figure 5.4: (a) The dotted line is the Born approximation of the spectrum with $a = 0.00417$ and $b = 0.917$, and the solid line the spectrum with radiative corrections at $\alpha_s = 0.22$ with $a = 0.00417$ and $b = 0.917$. The dashed line is the Born approximation of the spectrum with $a = 0.00566$ and $b = 0.889$, and the dot–dashed line the spectrum with radiative corrections at $\alpha_s = 0.22$ with $a = 0.00566$ and $b = 0.889$. (b) The dotted line is the Born approximation of the spectrum with $a = 0.00417$ and $b = 0.917$, and the solid line the spectrum with radiative corrections at $\alpha_s = 0.25$ with $a = 0.00417$ and $b = 0.917$. The dashed line is the Born approximation of the spectrum with $a = 0.00566$ and $b = 0.889$, and the dot–dashed line the spectrum with radiative corrections at $\alpha_s = 0.25$ with $a = 0.00566$ and $b = 0.889$.

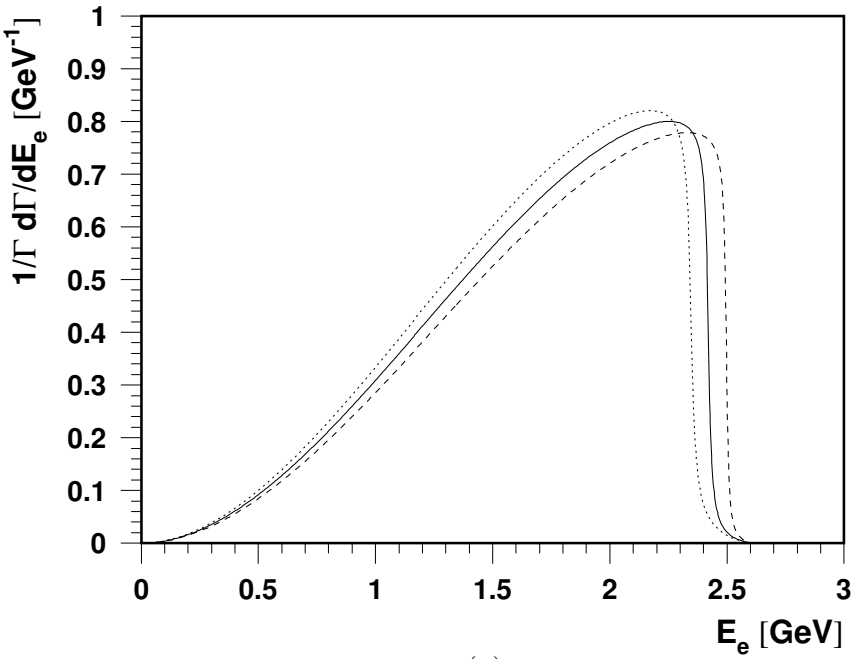


(a)

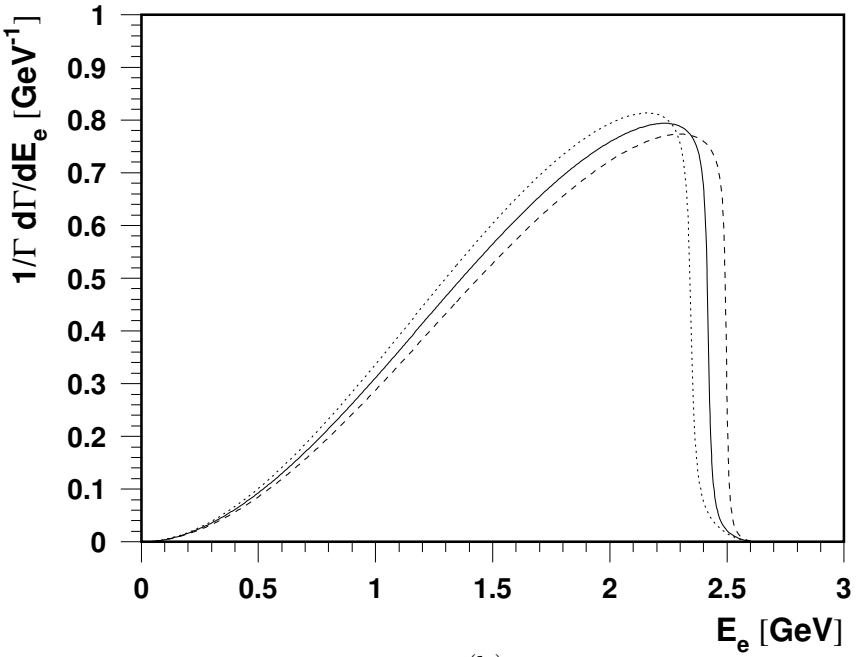


(b)

Figure 5.5: (a) The Born approximation of the electron energy spectrum from $B$-meson decay with various $a$ and $b$. (b) The electron energy spectra from $B$-meson decay with the radiative corrections at $\alpha_s = 0.22$. For both (a) and (b), the solid line is with $a = 0.00417$ and $b = 0.917$, the dotted line with $a = 0.00566$ and $b = 0.889$, and the dashed line with $a = 0.00298$ and $b = 0.946$.

### 5.2.2 Leptonic Invariant Mass Spectrum

Spectra of the leptonic invariant mass $W^2$ from $B$-meson decay are displayed in Figure 5.6 and Figure 5.7. As in the case of the electron energy spectrum in Section 5.2.1, we take various $a$, $b$, and $\alpha_s$ values and observe the change of shape of the spectrum.

Figure 5.6 shows the comparison for $b$-quark and $B$-meson decays for each of $\alpha_s = 0.22$ and $\alpha_s = 0.25$. At low $W^2$ the radiative corrections give significant contributions to the leptonic invariant mass spectrum in both cases.

One more thing to note in Figure 5.6 is that the $W^2$ spectrum from $B$-meson decay has moved upward in the small $W^2$ region with $QCD$ corrections included, whereas the $W^2$ spectrum with $QCD$ corrections from $b$-quark decay has moved downward in the same region.

The $W^2$ spectra with various $b$-quark masses are displayed in Figure 5.7. Figure 5.7(a) shows the Born approximation of the $W^2$ spectrum with different $a$ and $b$ values, and Figure 5.7(b) the $W^2$ spectrum with $QCD$ corrections at $\alpha_s = 0.22$. The shape of the spectrum changes obviously depending on the $b$-quark mass, i.e. the values of $a$ and $b$. However, the change from $QCD$ corrections is small for the $W^2$ spectrum, too. It means that the non–perturbative $QCD$ effect is more important than the perturbative $QCD$ corrections.

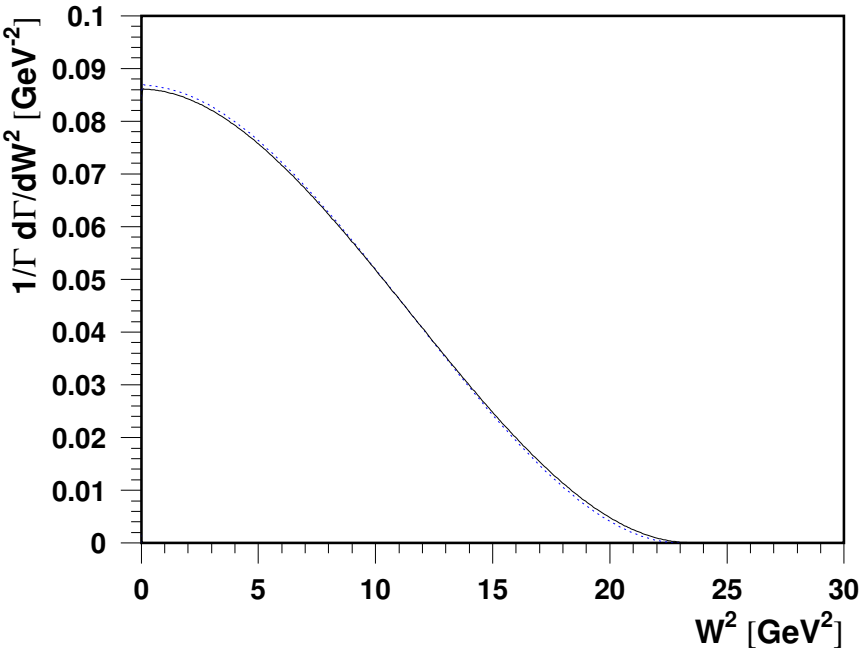


(a)

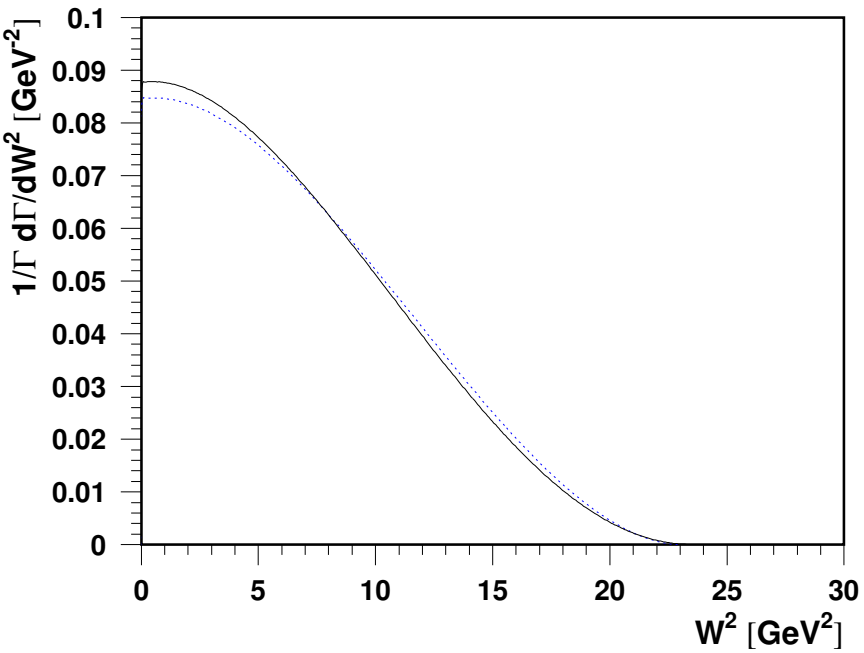


(b)

Figure 5.6: The $W^2$ spectrum from $B$-meson decay is compared with that from $b$-quark decay. In both (a) and (b), the dotted line is the $W^2$ spectrum from $b$-quark decay, and the solid line the spectrum from $B$-meson decay. The $b$-quark mass is assumed to be $m_b = 4.80\ GeV$. (a) The Born approximation of the $W^2$ spectrum from $b$-quark decay and from $B$-meson decay. (b) The $W^2$ spectrum with the radiative corrections at $\alpha_s = 0.22$ from $b$-quark decay and $B$-meson decay.

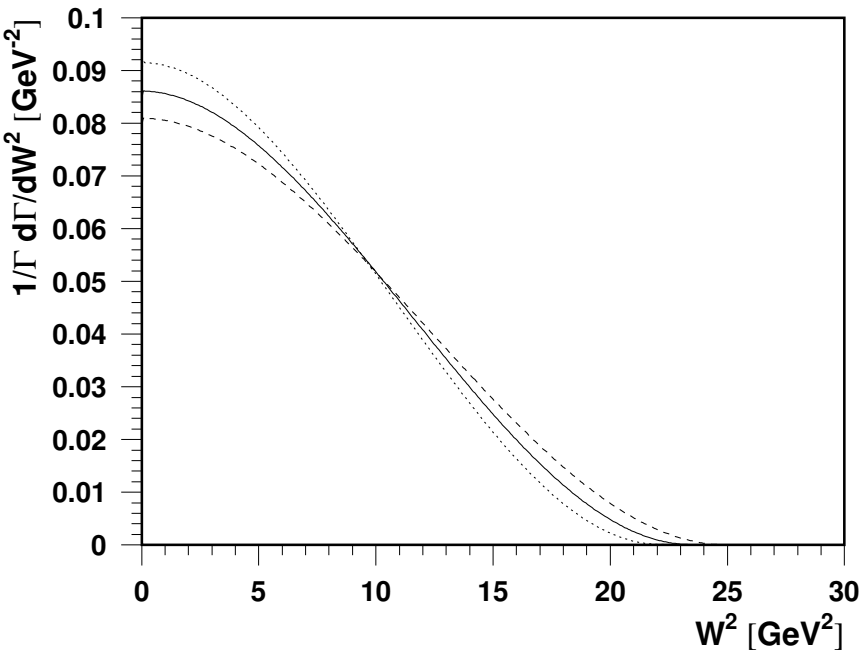


(a)

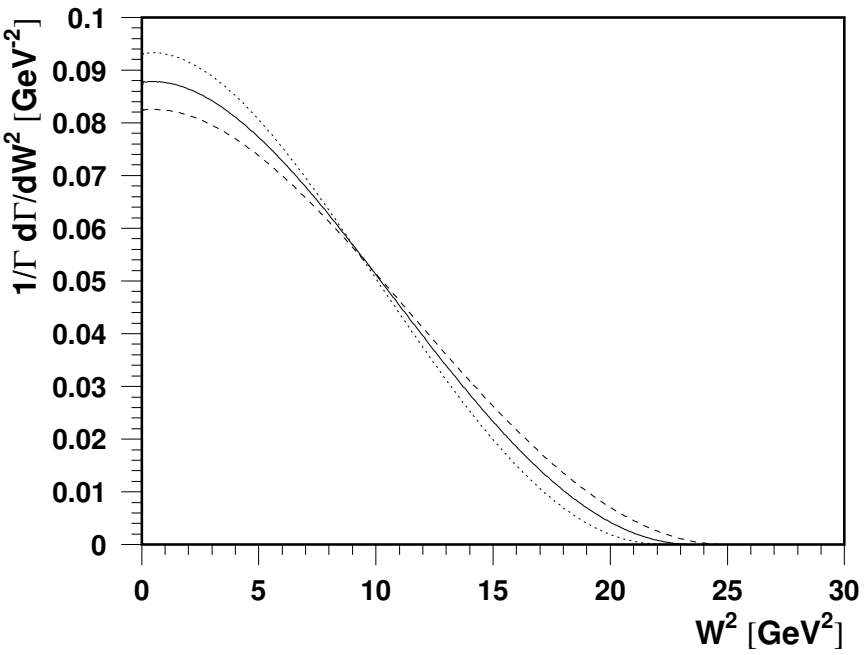


(b)

Figure 5.7: The dotted line: $m_b = 4.65\ GeV$; the solid line: $m_b = 4.80\ GeV$; the dashed line: $m_b = 4.95\ GeV$. (a) The Born approximation of the $W^2$ spectrum at various $a$ and $b$. (b) The $W^2$ spectrum with radiative corrections at $\alpha_s = 0.22$.

### 5.2.3 Hadronic Energy Spectrum

In this section we compare the hadronic energy $E_H$ spectrum from $B$-meson decay with that from $b$-quark decay in Chapter 4 and display the change of the spectrum according to $b$-quark mass. In Figure 5.8(a) the Born approximation of the hadronic energy spectrum from $B$-meson decay is compared with that from $b$-quark decay. Figure 5.8(b) shows the radiatively corrected spectra both from $B$-meson decay and from $b$-quark decay. The $b$-quark mass is assumed $m_b = 4.80\ GeV$, and strong coupling constant $\alpha_s = 0.22$ is used in Figure 5.8.

The hadronic energy spectrum from $B$-meson decay almost overlaps with that from $b$-quark decay up to $E_H \sim 2.6\ GeV$. The difference between the spectrum from $B$-meson decay and that from $b$-quark decay is dominant in the end point region of hadronic energy. The tail observed in the hadronic energy spectrum from $B$-meson decay in Figure 5.8(a) beyond $E_H \sim 2.8\ GeV$, appears in the spectrum from $b$-quark decay only after $QCD$ corrections are added. As seen in Figure 5.8(b), the tails become more apparent after $QCD$ corrections are included. The tails both from $B$-meson decay and from $b$-quark decay overlap with each other after $QCD$ corrections, and no significant difference is observed between the hadronic energy spectrum of $B$-meson decay and $b$-quark decay as seen in Figure 5.8(b). From this fact, we conjecture that the non–perturbative effect is not large for the hadronic energy spectrum and that $QCD$ corrections to $b$-quark decay can amend the non–perturbative aspect of $QCD$ to some degree.

In Figure 5.9 the spectra with various values of the $b$-quark mass are displayed. $b$-quark masses under consideration are $m_b = 4.65\ GeV$, $m_b = 4.80\ GeV$, and $m_b = 4.95\ GeV$. The corresponding $a$ and $b$ values for the distribution function suggested by Jin and Paschos are found in Table 5.1. Figure 5.9(a) shows the Born approximation of the hadronic energy spectrum, and Figure 5.9(b) the radiatively corrected spectrum. The shapes of the spectra are different depending on the parameters $a$ and $b$. The hadronic energy spectrum moves from left to right as the value of $a$ increases from $a = 0.00298$ (for $m_b = 4.95\ GeV$) to $a = 0.00566$ (for $m_b = 4.65\ GeV$). The $QCD$ corrections make the shape of the spectrum wider as observed in Figure 5.9(b).

The sharp peak in the $B$-meson decay spectrum with $QCD$ corrections is due to the fact that the radiative corrections have two different expressions beyond $E_H = M_B/2$. At the point $E_H = M_B/2$ where the two expressions meet, one observes a discontinuity. The sharp peak is also observed in the $b$-quark decay spectra in Figure 4.4 and in Figure 4.5 and becomes smoother in the $B$-meson decay spectra in Figure 5.8(b) and in Figure 5.9(b).

The hadronic energy spectra from $B$-meson decay in the parton model can be compared with results in other models. The hadronic energy spectra in ACCMM and the results in HQET are compared in [21]. The hadronic energy spectra in

the parton model is more similar to the results in HQET approaches.

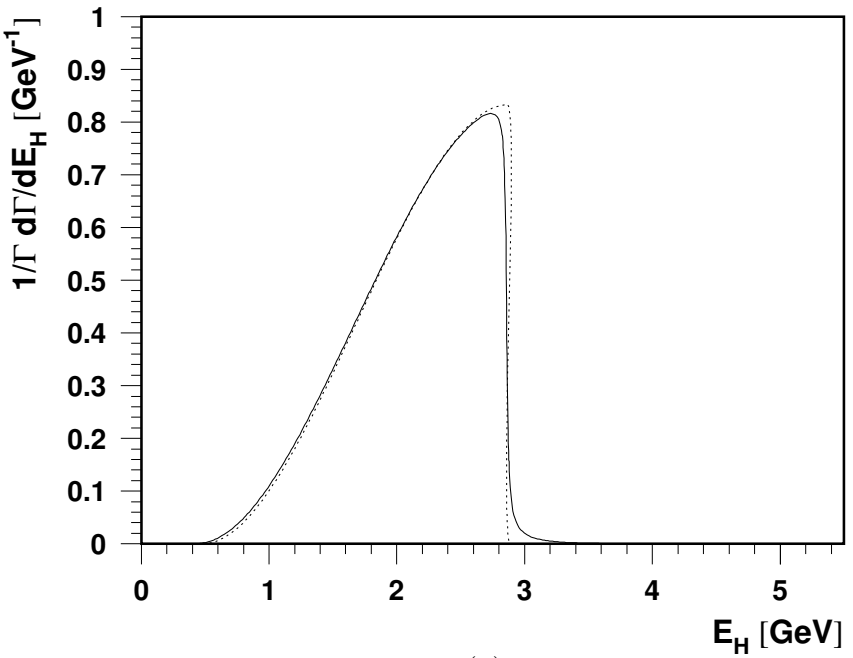


(a)

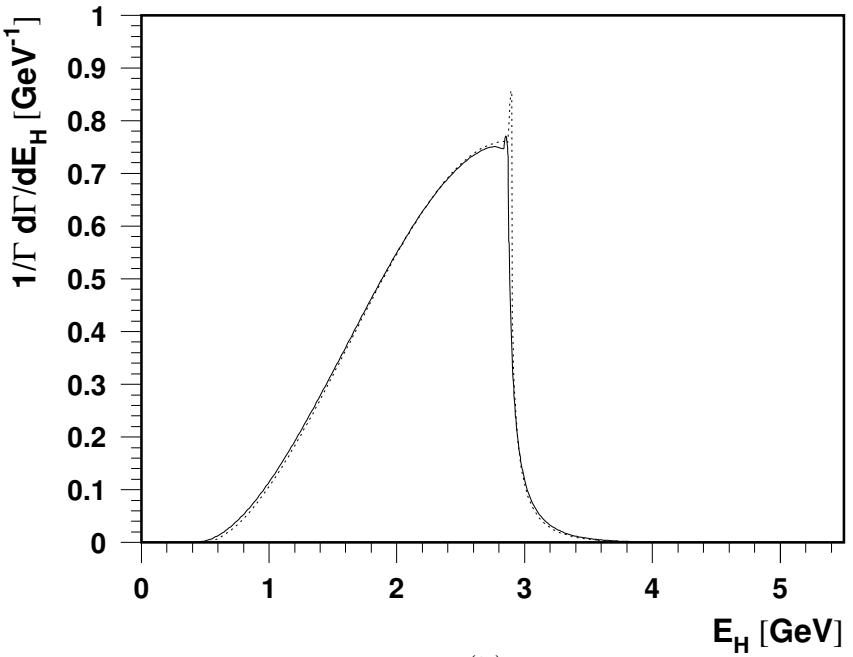


(b)

Figure 5.8: The hadronic energy spectrum from $B$-meson decay compared with that from $b$-quark decay at $m_b = 4.80\ GeV$. The solid line shows the spectrum from $B$-meson decay, and the dotted line from $b$-quark decay. (a) The Born approximation of the hadronic energy spectrum. (b) The hadronic energy spectrum with radiative corrections at $\alpha_s = 0.22$.

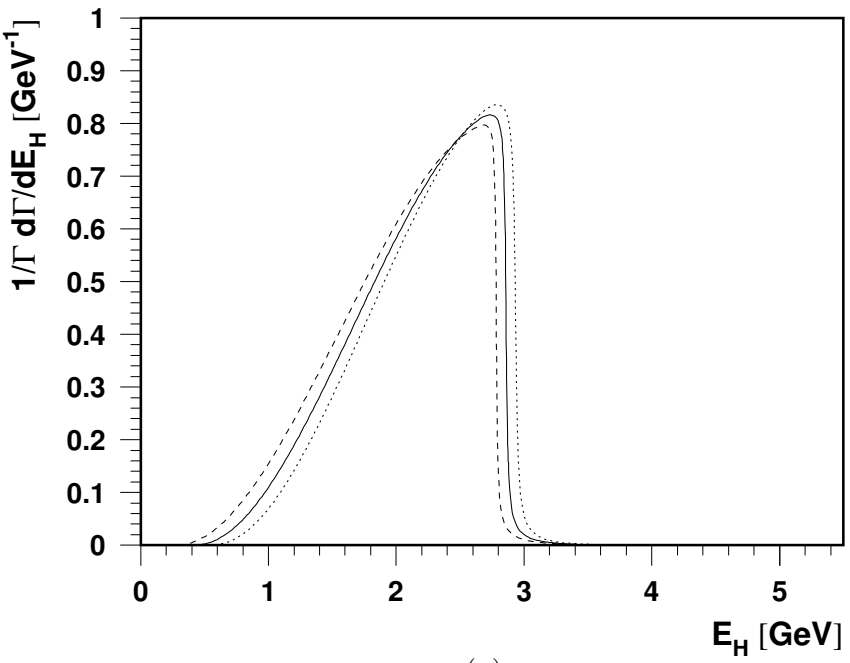


(a)

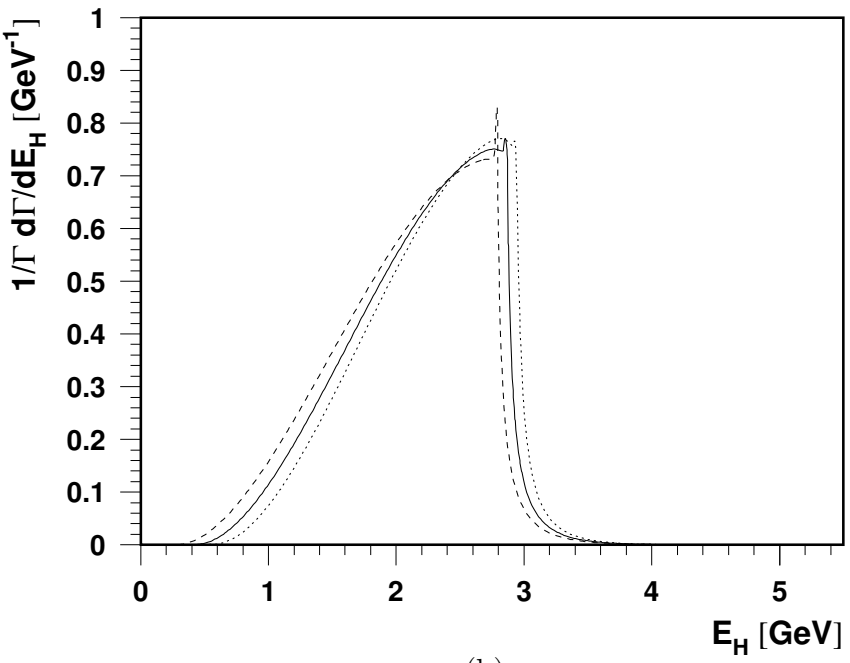


(b)

Figure 5.9: The hadronic energy spectrum from $B$-meson decay with various $a$ and $b$; the dotted line: $a = 0.00566$, $b = 0.889$; the solid line: $a = 0.00417$, $b = 0.917$; the dashed line: $a = 0.00298$, $b = 0.946$. (a) The Born approximation of the hadronic energy spectrum from $B$-meson decay. (b) The hadronic energy spectrum from $B$-meson decay with radiative corrections at $\alpha_s = 0.22$.

### 5.2.4 Hadronic Invariant Mass Spectrum

In this section we present the hadronic invariant mass $M_H$ spectrum and the squared hadronic invariant mass spectrum $S_H$. The squared hadronic invariant mass $S_H$ is defined in Eq.(4.8) in HQET ignoring higher order terms $\mathcal{O}(\frac{1}{m_b})$ and reads

$$S_H = P^2 + \frac{\bar{\Lambda}}{m_b}\left(m_b^2 - W^2 + P^2\right) + \bar{\Lambda}^2\,, \tag{5.35}$$

where $P$ is the quark–gluon system defined in Section 3.1. The hadronic invariant mass is defined as $M_H \equiv \sqrt{S_H}$.

Figure 5.10 shows the comparison between the squared hadronic invariant mass spectrum from $b$-quark decay and that from $B$-meson decay. The $b$-quark mass is assumed to be $m_b = 4.80\ GeV$, and the strong coupling constant $\alpha_s = 0.22$. In Figure 5.10(a) we observe that the Born approximation of the squared hadronic invariant mass spectrum from $B$-meson decay is obviously different from that from $b$-quark decay. The outstanding difference is observed at the end point of $S_H$. The tail beyond $S_H \sim 2.5\ GeV^2$, which is found in the $B$-meson decay spectrum, is not observed in the $b$-quark decay spectrum. After $QCD$ corrections are included, the two spectra from $B$-meson decay and from $b$-quark decay become similar at the end point of $S_H$. The sharp divergence around $S_H \sim 2.8\ GeV^2$ in $b$-quark decay has been smoothed in the $B$-meson decay spectrum. The squared hadronic invariant mass spectra from $B$-meson decay both at the Born Approximation and with $QCD$ corrections have moved to left compared to those from $b$-quark decay. We conjecture that the effect of non–perturbative $QCD$ has shifted the spectra from right to left.

In Figure 5.11 we compare the squared hadronic invariant mass spectrum from $B$-meson decay with various values of the $b$-quark mass. The corresponding values of $a$ and $b$ are displayed in Table 5.1. Depending on the values of $a$ and $b$, the spectrum shows different shapes. As the $b$-quark mass increases, the squared hadronic invariant mass spectrum moves from right to left and becomes narrower. The sharp peak from $QCD$ corrections has become smoothed and it becomes smoother as the $b$-quark mass becomes smaller.

The hadronic invariant mass $M_H$ spectrum is displayed in Figure 5.12 and in Figure 5.13. As the case of the squared hadronic invariant mass spectrum, we compare the hadronic invariant mass spectrum from $B$-meson decay with that from $b$-quark decay in Figure 5.12. The major difference is observed in the end point region of $M_H$, which is similar to the case of the squared hadronic invariant mass spectrum.

After $QCD$ corrections are included, no significant difference is observed between the hadronic invariant mass spectrum of $B$-meson decay and that of the

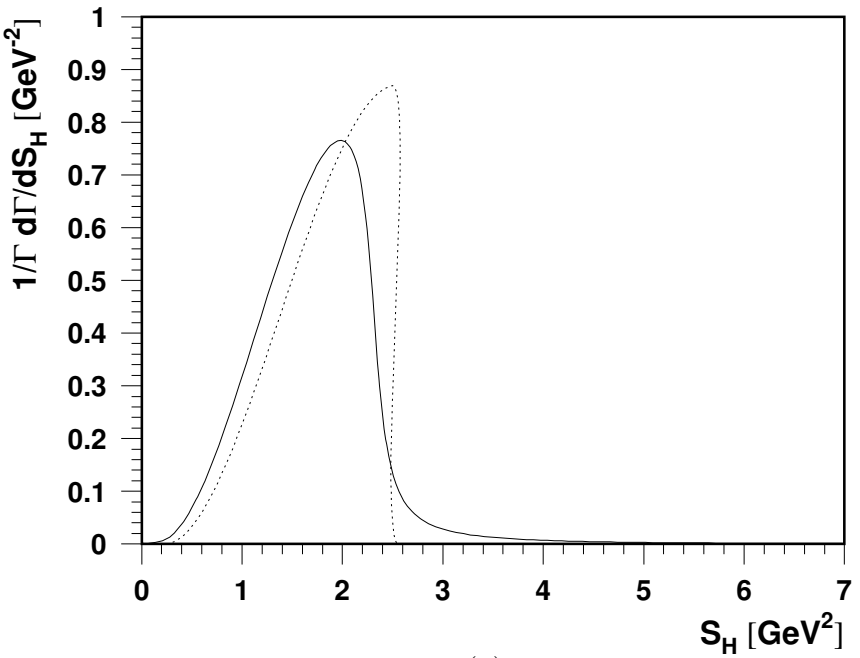


(a)

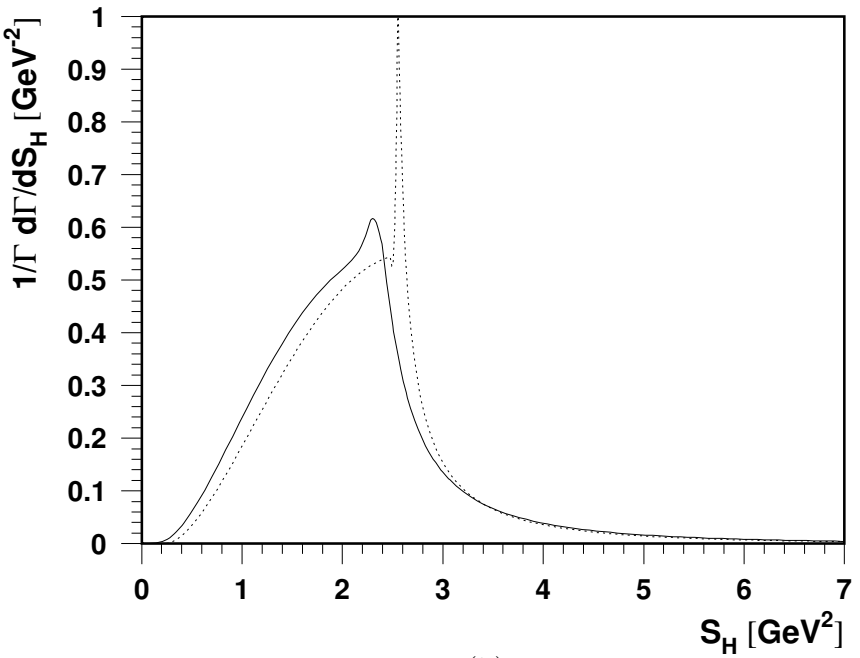


(b)

Figure 5.10: (a) The Born approximation of the squared hadronic invariant mass spectrum of $B$-meson decay is compared with that of $b$-quark decay. The solid line shows the spectrum of $B$-meson decay, and the dotted line of $b$-quark decay. (b) The spectrum with radiative corrections at $\alpha_s = 0.22$ are displayed. The solid line is the spectrum from $B$-meson decay, and the dotted line from $b$-quark decay.

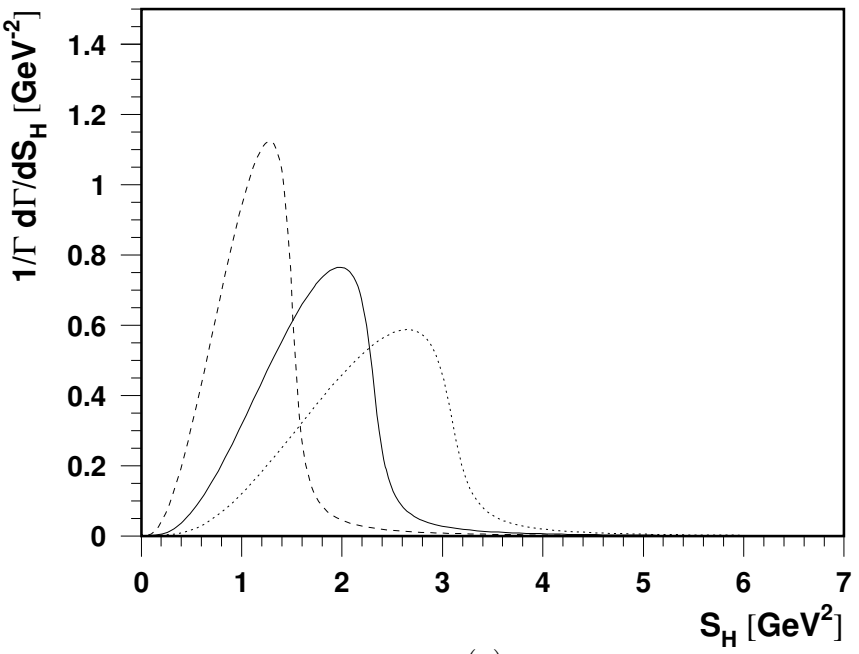


(a)

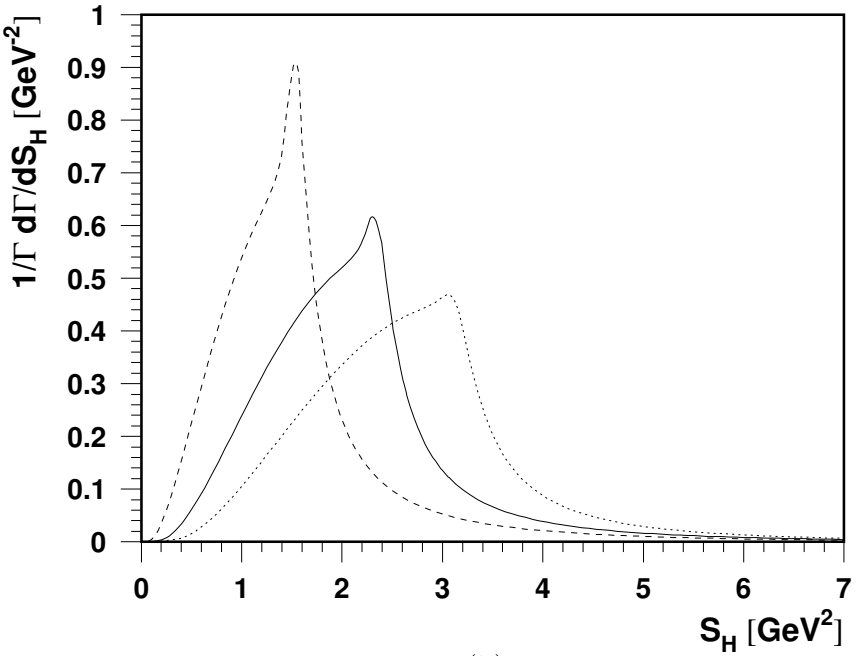


(b)

Figure 5.11: For both (a) and (b); the dotted line: $m_b = 4.65\ GeV$; the solid line: $m_b = 4.80\ GeV$; the dashed line: $m_b = 4.95\ GeV$. (a) The Born approximation of the squared hadronic invariant mass spectrum from $B$-meson decay. (b) The squared hadronic invariant mass spectrum with radiative corrections at $\alpha_s = 0.22$ from $B$-meson decay.

$b$-quark decay. From this fact, we conjecture that the non–perturbative effect is not large for the hadronic invariant mass spectrum and that $QCD$ corrections to $b$-quark decay can amend the non–perturbative aspect of $QCD$.

Figure 5.13 shows the hadronic invariant mass spectra with various $a$ and $b$ values which correspond to various values of the $b$-quark mass. The hadronic invariant mass spectra in Figure 5.13 can be compared with the results in [68], where different $a$ and $b$ are employed. The mean value and variance of the distribution function assumed in [68] are $\mu = 0.93$ and $\sigma^2 = 0.006$ respectively, and the corresponding $a$ and $b$ are $a = 0.0056$ and $b = 0.953$. The mean value and variance employed for Figure 5.13 are in Table 5.1. For example, when $m_b = 4.80\ GeV$, the mean value is $\mu = 0.907$ and the variance is $\sigma^2 = 0.0028640$. The variance in our analysis is smaller than that in [68], which results in a narrower shape of the hadronic invariant mass spectrum. The change in the hadronic invariant mass spectrum depending on the various $a$ and $b$ is similar to that in the squared hadronic invariant mass spectrum. As the $b$-quark mass increases, the hadronic invariant mass spectrum moves from right to left. Depending on the $b$-quark mass, the spectrum moves visibly, from which one can think that the hadronic invariant mass spectrum is suitable for investigating the $b$-quark mass.

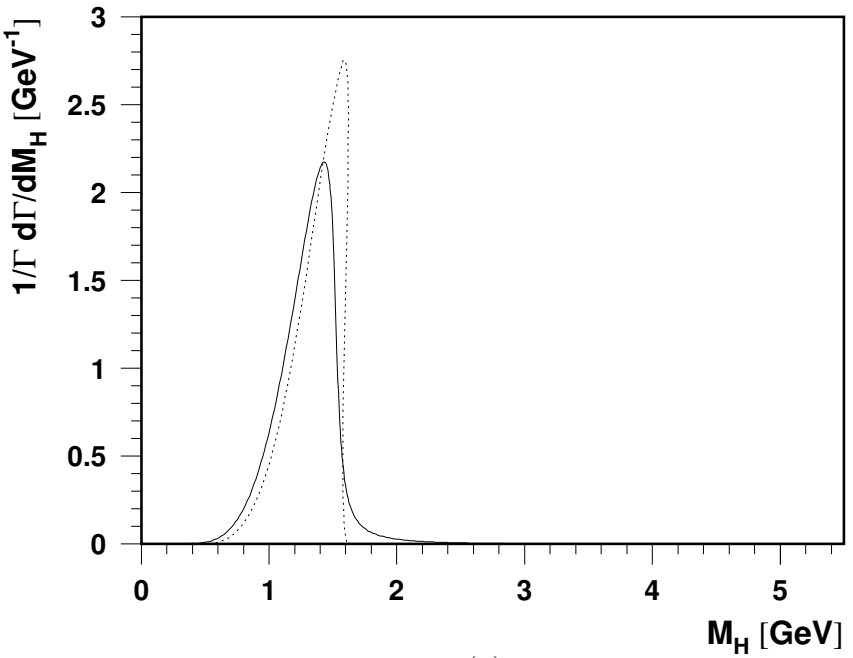


(a)

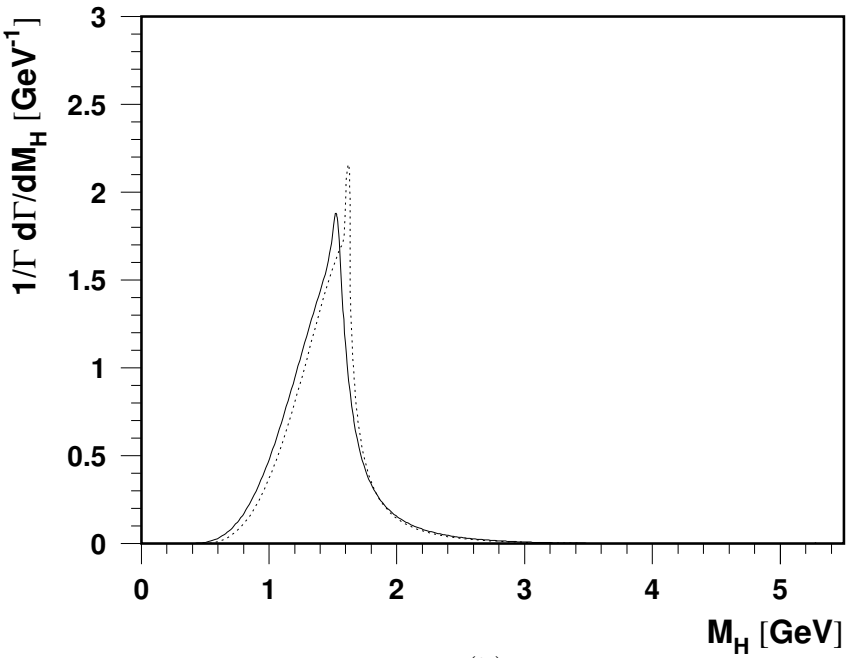


(b)

Figure 5.12: (a) The Born approximation of the hadronic invariant mass spectrum from $B$-meson decay is compared with that from $b$-quark decay. The solid line shows the spectrum from $B$-meson decay, and the dotted line from $b$-quark decay. (b) The solid line is the hadronic invariant mass spectrum with radiative corrections at $\alpha_s = 0.22$ from $B$-meson decay, and the dotted line that from $b$-quark decay.

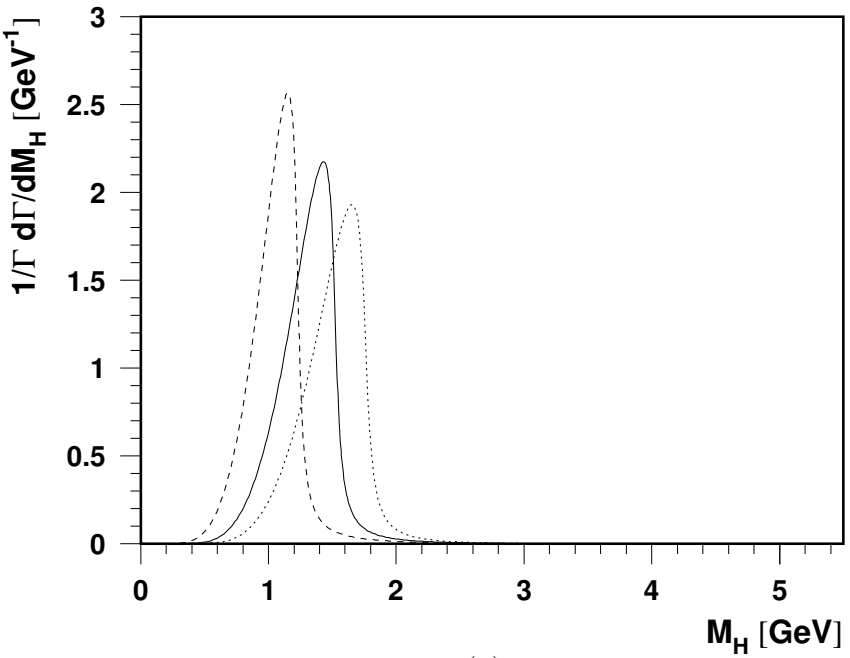


(a)

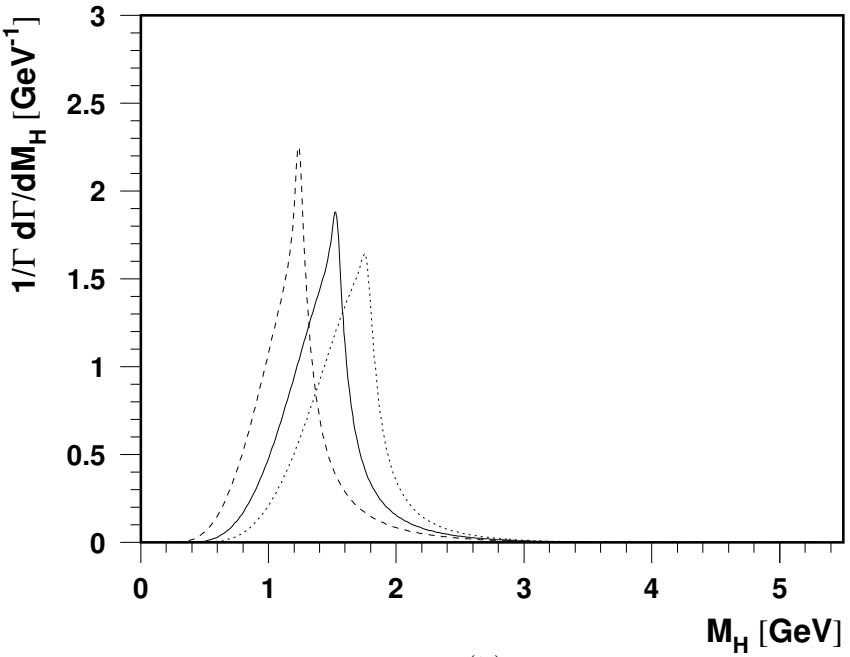


(b)

Figure 5.13: (a) The Born approximation of the hadronic invariant mass spectrum from $B$-meson decay with various $a$ and $b$ is displayed. (b) The hadronic invariant mass spectrum with radiative corrections at $\alpha_s = 0.22$. For both (a) and (b), the solid line is for $m_b = 4.80\ GeV$, the dashed line for $m_b = 4.65\ GeV$, and the dotted line for $m_b = 4.95\ GeV$.

# Chapter 6

# Evolution of the distribution function $f(x, W^2)$

In Chapter 5 we applied the naive parton model without considering further *QCD* interactions inside the $B$-meson. The parameters of the distribution function were determined using HQET parameters. In this chapter we consider further *QCD* interactions of the $b$-quark inside the $B$-meson and improve the naive parton model.

It is simply imagined that $b$-quarks might emit gluons before they decay into light quarks, resulting in changing the distribution function. One standard method to handle the further *QCD* interactions inside hadrons is Altarelli–Parisi type evolution of the distribution function.

One factors out the terms with collinear divergences, which appear when in–coming particles are massless, using the Leading Logarithmic Approximation (LLA). The leading logarithmic terms are factorized at a factorization scale $\mu_f^2$ into two parts. One part contains the $W^2$ dependence and the other the collinear divergences. The part with the collinear divergences is absorbed into the distribution function, and finally we obtain the $W^2$ dependent distribution function. We reproduce the Altarelli–Parisi evolution equation from $b$-quark decays and proceed the Altarelli–Parisi type evolution for the distribution function.

## 6.1 Altarelli–Parisi Evolution Equation

The distribution function is modified under consideration of further *QCD* interactions and gains a leptonic invariant mass $W^2$ dependence. One standard method is Altarelli–Parisi type evolution [94]. In this section, we briefly revisit the Altarelli–Parisi evolution equation, taking lepton–nucleon scatterings as an example.

The Altarelli–Parisi evolution equation is a set of integro–differential equations for the leptonic invariant mass $Q^2 = -q^2$ dependence of quark and gluon distributions in the case of lepton–nucleon scatterings $e + p \longrightarrow e' + X$.

For the case of one flavor of quarks we write a non singlet quark density as

$$f^{NS}(x,t) \;=\; f(x,t) \;-\; \bar{f}(x,t)\,, \tag{6.1}$$

where $t \equiv \frac{1}{2}\ln(Q^2/\mu_0^2)$ with a fixed reference momentum $\mu_0^2$. The moments of parton densities are defined as

$$M_n^{NS}(t) \;=\; \int_0^1 dx\, x^{n-1}\, f^{NS}(x,t)\,, \tag{6.2}$$

and the predicted $t$ dependence of moments is [96, 97]

$$M_n^{NS}(t) \;=\; M_n^{NS}(0)\left[\frac{\alpha}{\alpha(t)}\right]^{A_n^{NS}/2\pi b}\,, \tag{6.3}$$

where $\alpha(t)$ is the running coupling constant of *QCD*, and $b$ for *QCD* is given by

$$b = \frac{33 - 2f}{12\pi}\,, \tag{6.4}$$

with $f$ the number of flavors.

The Leading Logarithmic Approximation simplifies the running coupling constant $\alpha(t)$ as

$$\frac{\alpha}{\alpha(t)} = 1 \;+\; b\,\alpha\,t\,, \tag{6.5}$$

with $\alpha = \alpha(0)$. After differentiating Eq.(6.3) we obtain a differential equation

$$\frac{d\,M_n^{NS}(t)}{d\,t} = \frac{\alpha(t)}{2\pi}\,A_n^{NS} M_n^{NS}(t)\,, \tag{6.6}$$

and Eq.(6.3) is the solution of Eq.(6.6) with initial value $M_n^{NS}(0)$ at $t = 0$. We put Eq.(6.2) into Eq.(6.6) and obtain the Altarelli–Parisi evolution equation

$$\frac{d\, f^{NS}(x,t)}{d\, t} = \frac{\alpha(t)}{2\pi} \int_x^1 \frac{d\, y}{y} f^{NS}(y,t)\, \mathcal{P}\left(\frac{x}{y}\right), \tag{6.7}$$

provided

$$\int_0^1 dz\, z^{n-1}\, \mathcal{P}(z) = A_n^{NS}\,. \tag{6.8}$$

Eq.(6.8) can be rewritten in infinitesimal form as

$$\begin{aligned} f^{NS}(x,t) \,+\, df^{NS}(x,t) \;\; &= \;\; \int_0^1 dy \int_0^1 dx \delta(zy - x) f^{NS}(y,t) \times \\ &\left\{ \delta(z-1) \,+\, \frac{\alpha(t)}{2\pi}\, \mathcal{P}_{NS}(z)\, dt \right\}. \end{aligned} \tag{6.9}$$

The functions $\mathcal{P}_{NS}(z)$ are called splitting functions and are universal. In Section 6.2 we reproduce the splitting functions in the small $m_b$ limit.

## 6.2 Factorization

In Chapter 2, we obtained the Born approximation of the $B$-meson decay rate in the Light–Cone expansion and the triple differential decay rate formula in the Born approximation reads

$$\begin{aligned} \frac{d^3\Gamma}{dE_e\, dW^2\, dW^0} \;\; &= \;\; \frac{G_F^2\, |V_{ub}|^2}{4\,\pi^2\, M_B} \frac{W^0 - E_e}{\sqrt{(W^0)^2 - W^2 + m_u^2}} \times \\ &f(\chi_+) \left(2\chi_+\, E_e\, M_B - W^2\right), \end{aligned} \tag{6.10}$$

and we set $m_u = 0$. In the Born approximation the main contribution is from the variable $\chi_+$ and we ignore the contribution from the other variable $\chi_-$.

In the deep inelastic region, where we consider further $QCD$ interactions of the partons, $\chi_-$ approaches the Bjorken scaling variable. Replacing the $B$-meson

mass $M_B$ with the $b$-quark mass $m_b$ and expanding it in the powers of small $m_b$, we obtain

$$\begin{aligned}
\chi_- &= \frac{W\cdot P_B - \sqrt{(W\cdot P_B)^2 - M_B^2\, W^2}}{M_B^2} \\
&\xrightarrow{M_B\to m_b,\, P_B\to p_b} \frac{W\cdot p_b - \sqrt{(W\cdot p_b)^2 - m_b^2\, W^2}}{m_b^2} \\
&= \frac{W\cdot p_b}{m_b^2} - \frac{W\cdot p_b}{m_b^2}\left(1 - \frac{m_b^2\, W^2}{2(W\cdot p_b)^2} - \frac{1}{8}\left(\frac{m_b^2\, W^2}{(W\cdot p_b)^2}\right)^2 + \mathcal{O}(m_b^6)\right) \\
&= \frac{W^2}{2W\cdot p_b} + \mathcal{O}(m_b^2)\,, \qquad (6.11)
\end{aligned}$$

which is the same as the Bjorken scaling variable. We define

$$\chi'_- \equiv \frac{W^2}{2W\cdot p_b}\,. \qquad (6.12)$$

In Eq.(6.11) $W^2$ is positive and we do not need to change the sign as in the case of lepton–nucleon scatterings. From Eq.(6.11) we conclude that the scaling variable $\chi_-$ can be identified as the Bjorken scaling variable in the deep inelastic region, where further $QCD$ interactions become significant. The distribution function $f(x)$ is modified by considering further $QCD$ interactions of the $b$-quark inside the $B$-meson and obtains the $W^2$ dependence.

In Chapter 3 we obtained radiative corrections to semi–leptonic $b$-quark decays. The differential decay rate is expressed in the variables $x$, $y$, and $z$, which are scaled by $p_b^2 = m_b^2$. The results in Chapter 3 were proven to be identical with the results in [4]. For the convenience of calculation we adopt the results in [4].

The $b$-quark mass $m_b$ is given in the parton model as $m_b^2 = \chi^2\, M_B^2$, and $\chi$ is the momentum fraction of the $b$-quark from the $B$-meson. The collinear singularity appears when $\chi \to 0$ and consequently, $m_b^2 \to 0$. One method to remove this collinear singularity is the Leading Logarithmic Approximation (LLA). We take the leading logarithmic terms which are divergent as $m_b^2 \to 0$ and factorize with a factorization scale $\mu_f^2$. The divergent part with $\ln(\mu_f^2/m_b^2)$ is absorbed into the distribution function, and one gets an evolution equation of the distribution function as the result.

In the limit of $m_b \to 0$, we express the variables $\hat{p}^2$ and $z$ in [4] using $\chi'_-$ as

$$\hat{p}^2 \equiv \frac{P^2}{m_b^2} = \frac{(1+y)(\chi'_- - 1)}{\chi'_-}\,, \qquad (6.13)$$

$$z \equiv \frac{2v\cdot p}{m_b} = 1 - y + \frac{(1+y)(\chi'_- - 1)}{\chi'_-}\,, \qquad (6.14)$$

where $W$ and $P$ are the momenta of lepton system and quark–gluon system respectively as defined in Section 3.1.

We expand the invariant functions $W_i$ in [4] in powers of small $m_b^2$. All other $W_i$ except $W_1$ vanish in the small $m_b^2$ limit, and we obtain the same tensor structure as that of the Born approximation in Eq.(2.34). Taking the limit of $m_b \to 0$ we extract from $W_1$ the collinear contribution of order $\alpha_s$ to the $b$-quark deep inelastic tensor, which reads

$$\frac{\alpha_s}{2\pi} P_{qq}(\chi'_-) \ln(\mu^2/m_b^2)\,, \tag{6.15}$$

with

$$\mu^2 \equiv m_b^2 - W^2\,, \tag{6.16}$$

and

$$\begin{aligned} P_{qq}(\chi'_-) &= C_F \left[ \frac{2}{[1-\chi'_-]_+} - (1+\chi'_-) \right] \\ &= C_F \frac{1+{\chi'_-}^2}{(1-\chi'_-)_+}\,, \end{aligned} \tag{6.17}$$

where $C_F = \frac{4}{3}$. The logarithmic term in Eq.(6.15) is factorized with the factorization scale $\mu_f^2$ and the change in the distribution function by the radiative corrections reads

$$\begin{aligned} \Delta f(x,\mu^2) &= \frac{\alpha_s(\mu^2)}{2\,\pi} \int_0^1 dy\, du\, f(y,\mu^2) P_{qq}(u) \times \\ &\quad \Big[\delta(yu-x) - \delta(y-x)\Big] d(\ln(\mu^2))\,. \end{aligned} \tag{6.18}$$

Eq.(6.18) is written as the same form as the non–singlet contribution of the Altarelli–Parisi evolution equation

$$\frac{df(x,t)}{dt} = \frac{\alpha_s(t)}{2\,\pi} \int \frac{dy}{y}\, f(y,t) P_{qq}(x/y)\,, \tag{6.19}$$

with $t = \frac{1}{2}\ln(\mu^2/\mu_0^2)$, where the factorization scale $\mu_f^2$ is replaced with the reference momentum scale $\mu_0^2$.

We replace the splitting function $P_{qq}(z)$ in Eq.(6.19) with the conventional splitting function

$$P_{qq}(z) = C_F \left[ \frac{3}{2}\delta(1-z) + \frac{1+z^2}{(1-z)_+} \right], \tag{6.20}$$

which includes the contributions from virtual corrections. The distribution function in Eq.(6.19) depends on $\mu^2$, and we use $\mu^2$ as the evolution variable. We define $b = xP_B$ and $m_b^2 = x^2 M_B^2$ using the parton model description, and the $b$-quark mass changes inside the $B$-meson depending on the scaling variable $x$.

Including the evolved distribution function, we write the differential decay rate as

$$d\Gamma = \int_0^1 dx\, d\hat{\Gamma} f(x, \mu^2)\,, \tag{6.21}$$

where

$$\frac{d\hat{\Gamma}}{dE_e\, dW^2\, dW^0} = \frac{G_F^2\, |V_{ub}|^2}{4\,\pi^2\, M_B} \frac{\left(2\, M_B\, x\, E_e - W^2\right)}{\sqrt{(W^0)^2 - W^2 + m_u^2}} \left(W^0 - E_e\right), \tag{6.22}$$

and $f(x, \mu^2)$ is obtained by solving the Altarelli–Parisi evolution equation.

We consider that the evolution of the distribution function starts from the leptonic invariant mass $W^2 = 1\ GeV^2$, which corresponds to $\mu^2 = m_b^2 - 1\ GeV^2$, and continues until the value of the evolution variable $\mu^2$ reaches the reference momentum scale $\mu_0^2 = 1\ GeV^2$. We should note that $m_b^2$ is not fixed but varies depending on $x$. When $\mu^2 = x^2 M_B^2 - 1\ GeV^2 \leq 1\ GeV^2$, which corresponds to $x \sim 0.27$, there happens to be no evolution of the distribution function.

## 6.3 Spectra with Evolved Distribution Function

In the last section we showed that the distribution function obtains $\mu^2$ dependence from the *QCD* corrections, where $m_b^2$ is given by $m_b^2 = x^2 M_B^2$, and the evolution equation of the distribution function is the Altarelli–Parisi equation in the small $m_b$ limit, i.e. in the region of small $x$. The solution of the Altarelli–Parisi equation is carried out numerically. In this section, we display the numerical solution of the Altarelli–Parisi evolution equation for the distribution function and show how the distribution function changes depending on the leptonic invariant mass $W^2$. We use the evolution program which was used in [99].

We adopt two different models for the distribution functions. One is the model suggested by Jin and Paschos, and it reads at the reference momentum $\mu_0^2 = 1\ GeV^2$

$$f_{jp}(x, \mu_0^2) = N_{jp} \frac{x(1-x)}{(x-b)^2 + a^2}\,, \tag{6.23}$$

which we used for the naive parton model investigation in Chapter 5. In Chapter 5 we used the distribution function at the reference momentum in Eq.(6.23), which is independent of $\mu^2$. The other one is

$$f_{ptr}(x, \mu_0^2) = N_{ptr} \frac{x(1-x)}{\left((1-x)^2 + \epsilon_Q x\right)^2}\,, \tag{6.24}$$

which is the fragmentation function found by Peterson *et al.* [78]. Both $N_{jp}$ and $N_{ptr}$ in Eq.(6.23) and Eq.(6.24) are constants to keep the normalization condition $\int_0^1 dx f(x, \mu_0^2) = 1$. The $\mu^2$ dependent distribution $f(x, \mu^2)$ should also satisfy the normalization condition

$$\int_0^1 dx f(x, \mu^2) = 1\,. \tag{6.25}$$

The parameters $a$ and $b$ in Eq.(6.23) are found in Table 5.1 and $\epsilon_Q$ in Eq.(6.24) in Table 5.2

We have checked if the normalization condition in Eq.(6.25) was still kept numerically at each point of $\mu^2$ with the normalization constants $N_{jp}$ and $N_{ptr}$ which were determined for the distribution functions at the reference momentum scale. In Table 6.1 and Table 6.2 we present the numerical results of $S[\, f(x, \mu^2)\,] \equiv \int_0^1 dx f(x, \mu^2)$ at various points of $\mu^2$ with fixed $m_b$ for each $f_{jp}(x, \mu^2)$ and $f_{ptr}(x, \mu^2)$. $E[\, f(x, \mu^2)\,]$ represents errors from the numerical integration.

The values of $S[\, f(x, \mu^2)\,]$ are centered around 1, and the errors $E[\, (f(x, \mu^2)\,]$ are found to be small. From the data in Table 6.1 and Table 6.2 we conclude that $f(x, \mu^2)$ keeps the normalization condition in Eq.(6.25) up to 10 % at each point of $\mu^2$.

Evolution starts from the leptonic invariant mass $W^2 = 1\ GeV^2$, which corresponds to the Light–Cone region. The evolution range is, therefore, $1\ GeV^2 \leq \mu^2 \leq m_b^2 - 1\ GeV^2$. In Figure 6.1 and Figure 6.2 we present the behavior of $f_{jp}(x, \mu^2)$ and $f_{ptr}(x, \mu^2)$. In Figure 6.1(a) and Figure 6.2(a) the $b$-quark mass is fixed as $m_b^2 = 4.80^2\ GeV^2$ and in Figure 6.1(b) and Figure 6.2(b) the $b$-quark mass varies according to $m_b^2 = x^2 M_B^2$. We compare each case at different points of $\mu^2$. The distribution functions $f_{jp}(x, \mu^2)$ and $f_{ptr}(x, \mu^2)$ around small $x$ increase

| $W^2$ | $S[\, f_{jp}(x,\mu^2)\,]$ | $E[\, f_{jp}(x,\mu^2)\,]$ |
|---|---|---|
| 21.93800 | 1.142124534 | 0.1381640672E-02 |
| 20.83600 | 1.139075041 | 0.1401385991E-02 |
| 17.53000 | 1.126130819 | 0.1613053493E-02 |
| 15.32600 | 1.117343783 | 0.1482947962E-02 |
| 12.02000 | 1.099180460 | 0.1312843524E-02 |
| 8.71400 | 1.079625368 | 0.1642389805E-02 |
| 6.51000 | 1.061116576 | 0.1287984662E-02 |
| 4.30600 | 1.036525965 | 0.1631325111E-02 |
| 2.10200 | 1.008489013 | 0.2059279941E-02 |
| 1.00000 | 1.003213882 | 0.1493989490E-02 |

Table 6.1: The numerical integration of $f_{jp}(x, \mu^2)$ from 0 to 1 at various $\mu^2$.

| $W^2$ | $S[\, f_{ptr}(x,\mu^2)\,]$ | $E[\, f_{ptr}(x,\mu^2)\,]$ |
|---|---|---|
| 21.93800 | 1.141752720 | 0.2556202002E-02 |
| 20.83600 | 1.134530425 | 0.2216120018E-02 |
| 17.53000 | 1.121706963 | 0.2931362018E-02 |
| 15.32600 | 1.117235065 | 0.2805365715E-02 |
| 12.02000 | 1.099050164 | 0.2308317227E-02 |
| 8.71400 | 1.076738596 | 0.2496725414E-02 |
| 6.51000 | 1.056773901 | 0.2182442229E-02 |
| 4.30600 | 1.041793942 | 0.2096810378E-02 |
| 2.10200 | 1.009744167 | 0.2084070817E-02 |
| 1.00000 | 1.000792861 | 0.2969027730E-02 |

Table 6.2: The numerical integration of $f_{ptr}(x, \mu^2)$ from 0 to 1 at various $\mu^2$.

after evolution as $\mu^2$ increases with fixed $m_b$. The difference in the evolved distribution function between the fixed $b$-quark mass and the varying $b$-quark mass is observed in the small $x$ region.

The specific behavior of $f_{jp}(x,\mu^2)$ and $f_{ptr}(x,\mu^2)$ with fixed $m_b$ at a certain $x$ according to the change of $\mu^2$ is depicted in Figure 6.3 and Figure 6.4. We have chosen $x = 0.01, 0.3, 0.6, 0.7, 0.9, 0.95$ and the behavior of $f_{jp}(x,\mu^2)$ and $f_{ptr}(x,\mu^2)$ are different at each point of $x$. This is due to the different shape of the two different distribution functions. The peak point of $f_{ptr}(x,\mu_0^2)$ is closer to $x = 1$ than that of $f_{jp}(x,\mu_0^2)$.

The electron energy spectrum with the evolved distribution function is displayed in Figure 6.5. In Figure 6.5(a) we compare the electron energy spectrum in the naive parton model with that of the evolved distribution function. The distribution function used for Figure 6.5(a) is $f_{jp}(x,\mu^2)$ with $m_b^2 = x^2 M_B^2$. The electron energy spectrum with the evolved distribution function is shifted from right to left, which corresponds to the fact that the evolution makes the mean values of the distribution functions become smaller. In Figure 6.5(b) the electron energy spectrum with $f_{jp}(x,\mu^2)$ is compared with that with $f_{ptr}(x,\mu^2)$. The difference is found in the end point region of the electron energy. The electron energy spectrum with $f_{ptr}(x,\mu^2)$ does not approach 0 as rapidly as the spectrum with $f_{jp}(x,\mu^2)$ does. This is from the fact that peak point of $f_{ptr}(x,\mu_0^2)$ is closer to $x = 1$ than that of $f_{jp}(x,\mu_0^2)$, which is observed in Figure 6.1 and Figure 6.2.

In Figure 6.6 the electron energy spectra with various evolution ranges are displayed, and we can observe the effect of the evolution range. The dashed line is the electron energy spectrum with the evolution starting point $W^2 = 5\ GeV^2$, which corresponds to $\mu^2 = x^2 M_B^2 - 5\ GeV^2$, and the dot–dashed line the spectrum with the evolution starting point $W^2 = 20\ GeV^2$, which corresponds to $\mu^2 = x^2 M_B^2 - 20\ GeV^2$. As the evolution range becomes wider, the electron energy spectrum is shifted more from right to left.

In Figure 6.7 we display the leptonic invariant mass spectrum $W^2$. Figure 6.7(a) shows the $W^2$ spectrum with $f_{jp}(x,\mu^2)$ with $m_b^2 = x^2 M_B^2$ and that with $f_{jp}(x)$ from the naive parton model. The evolution of the distribution function makes the leptonic invariant mass spectrum narrower. The dominant effect of the evolution is observed in the small $W^2$ region.

In Figure 6.7 we compare the $W^2$ spectra with $f_{jp}(x,\mu^2)$ and $f_{ptr}(x,\mu^2)$. The two $W^2$ spectra with the two different distribution functions do not much differ from each other, as is the case of the electron energy spectrum, where we observe a difference only in the end point region of the electron energy. We can conclude that the $W^2$ spectrum has less dependence on the model of the distribution function.

In Figure 6.8 we present the $W^2$ spectra with various evolution range. The solid line is the leptonic invariant mass spectrum with the evolution starting point $W^2 = 1\ GeV^2$, which corresponds to $\mu^2 = x^2 M_B^2 - 1\ GeV^2$, and the dot–dashed line with the evolution starting point $W^2 = 20\ GeV^2$, which corresponds

to $\mu^2 = x^2 M_B^2 - 20\ GeV^2$. As the evolution range becomes narrower, the effect of evolution in the small $W^2$ region becomes smaller. We can conclude that perturbative $QCD$ effects dominate in the small $W^2$ region.

We can argue about possible errors in the spectrum with the evolved distribution functions. First, we can think of the errors from the numerical integration, but these are within 2.5 %. The second possible errors are from the normalization condition of the evolved distribution functions. In Table 6.1 and Table 6.2 we have shown the normalization condition of each distribution function. We conclude that the evolved distribution function were well normalized. However, strictly speaking, the values of $S[\, f_{jp}(x, \mu^2)\,]$ and $S[\, f_{ptr}(x, \mu^2)\,]$ are not exactly 1, but they increase slightly as $\mu^2$ becomes large.

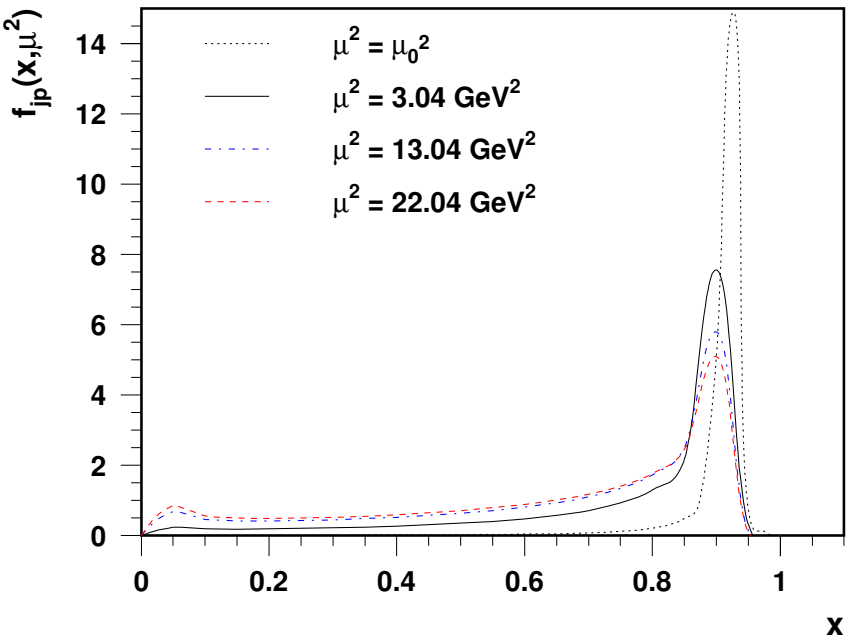


(a)

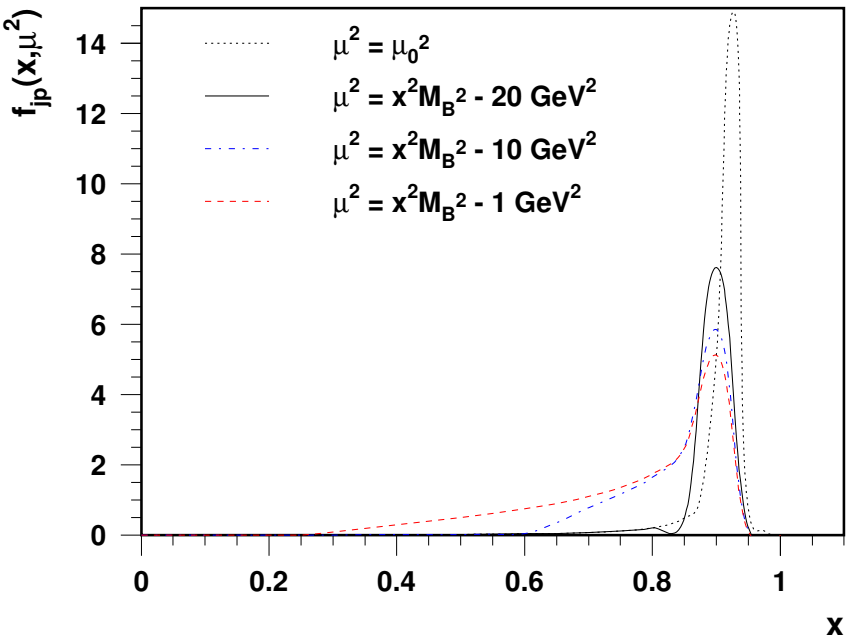


(b)

Figure 6.1: (a) The change of $f_{jp}(x,\mu^2)$ with fixed $m_b^2 = 4.80^2\ GeV^2$. $f_{jp}(x,\mu^2)$ at $\mu^2 = 3.04\ GeV^2$, $13.04\ GeV^2$, $22.04\ GeV^2$. (b) The change of $f_{jp}(x,\mu^2)$ with $\mu^2 = x^2M_B^2 - W^2$. $f_{jp}(x,\mu^2)$ at $\mu^2 = x^2M_B^2 - 20\ GeV^2$, $x^2M_B^2 - 10\ GeV^2$, $x^2M_B^2 - 1\ GeV^2$.

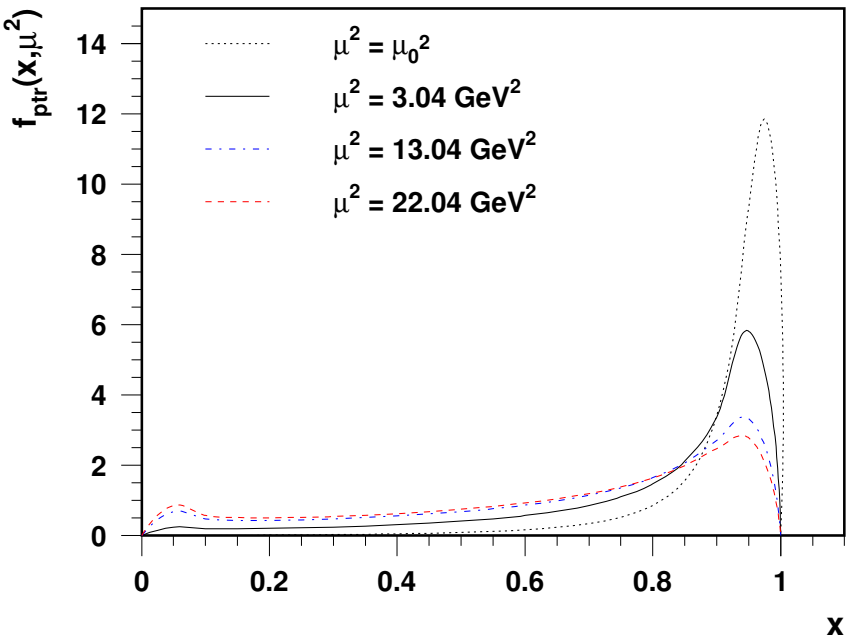


(a)

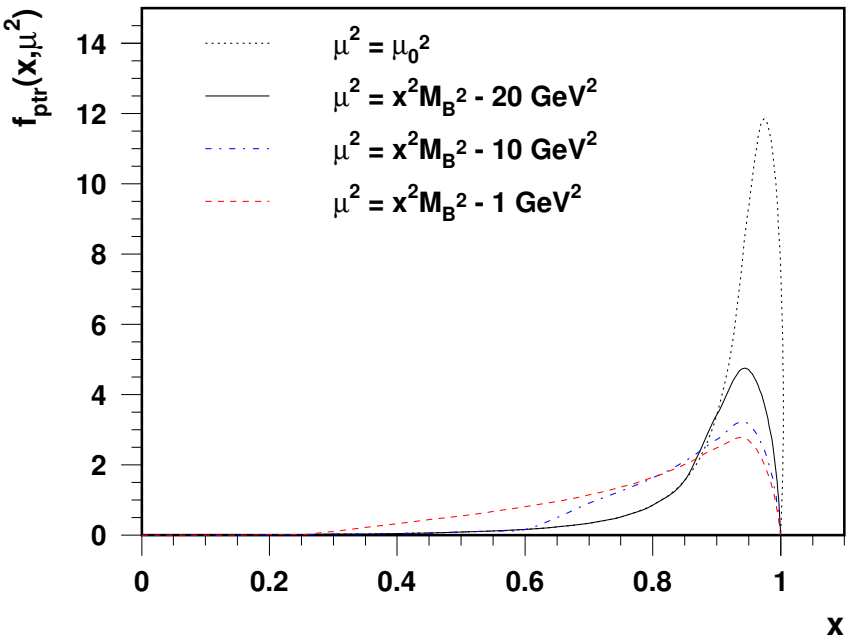


(b)

Figure 6.2: (a) The change of $f_{ptr}(x, \mu^2)$ with fixed $m_b^2 = 4.80^2\ GeV^2$. $f_{ptr}(x, \mu^2)$ at $\mu^2 = 3.04\ GeV^2$, $13.04\ GeV^2$, $22.04\ GeV^2$. (b) The change of $f_{ptr}(x, \mu^2)$ with $\mu^2 = x^2 M_B^2 - W^2$. $f_{ptr}(x, \mu^2)$ at $\mu^2 = x^2 M_B^2 - 20\ GeV^2$, $x^2 M_B^2 - 10\ GeV^2$, $x^2 M_B^2 - 1\ GeV^2$.

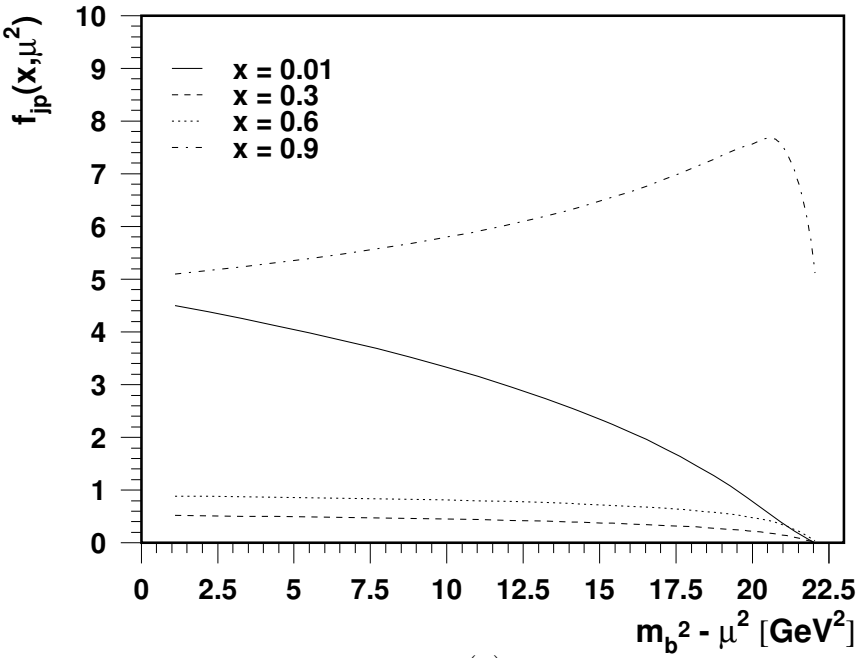


(a)

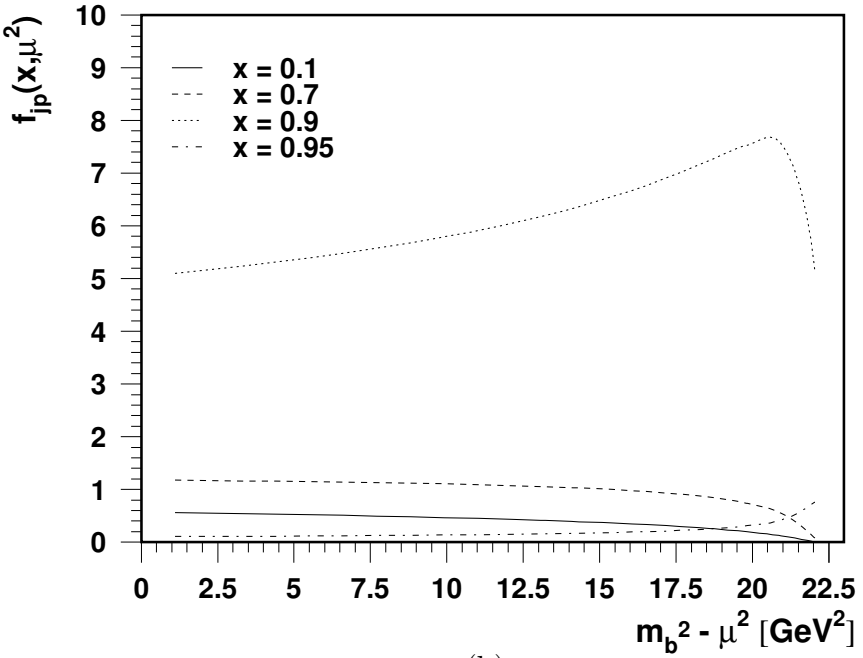


(b)

Figure 6.3: (a) The change of $f_{jp}(x, \mu^2)$ at $x = 0.01$, 0.3, 0.6, 0.9. (b) The change of $f_{jp}(x, \mu^2)$ at $x = 0.1$, 0.7, 0.9, 0.95. For both (a) and (b), $m_b^2 = 4.80^2\ GeV^2$.

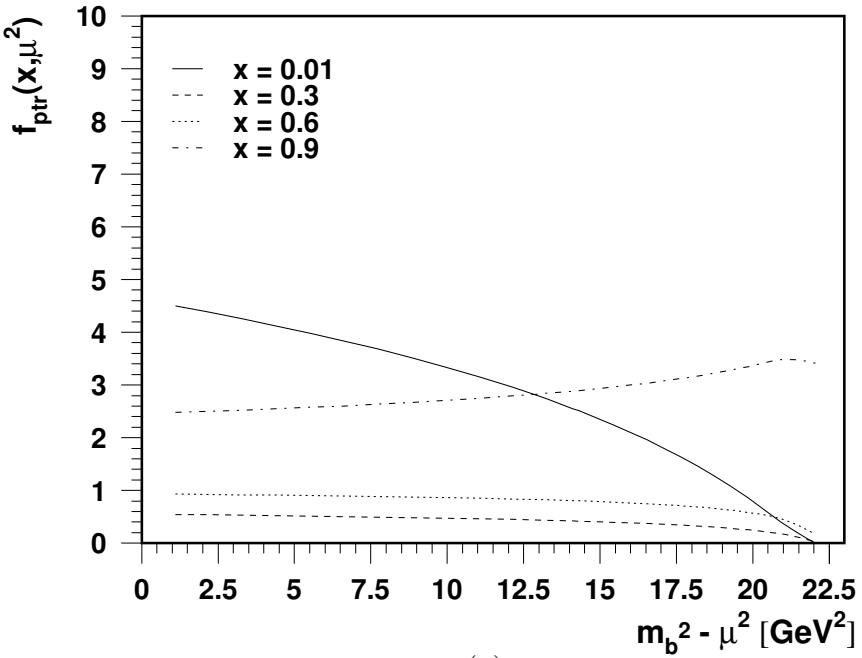


(a)

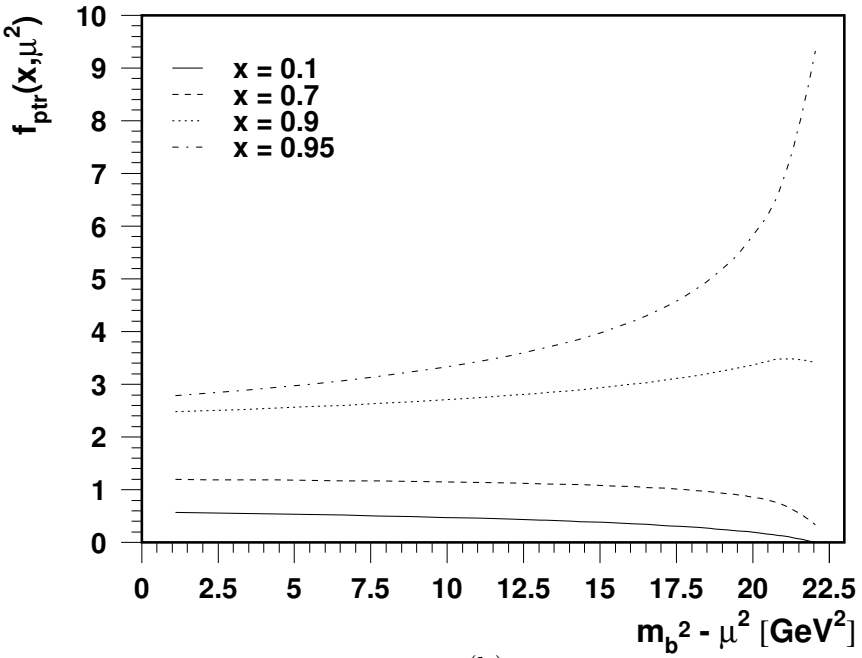


(b)

Figure 6.4: (a) $f_{ptr}(x, \mu^2)$ at $x = 0.01, 0.3, 0.6, 0.9$. (b) $f_{ptr}(x, \mu^2)$ at $x = 0.1, 0.7, 0.9, 0.95$. For both (a) and (b), $m_b^2 = 4.80^2\ GeV^2$.

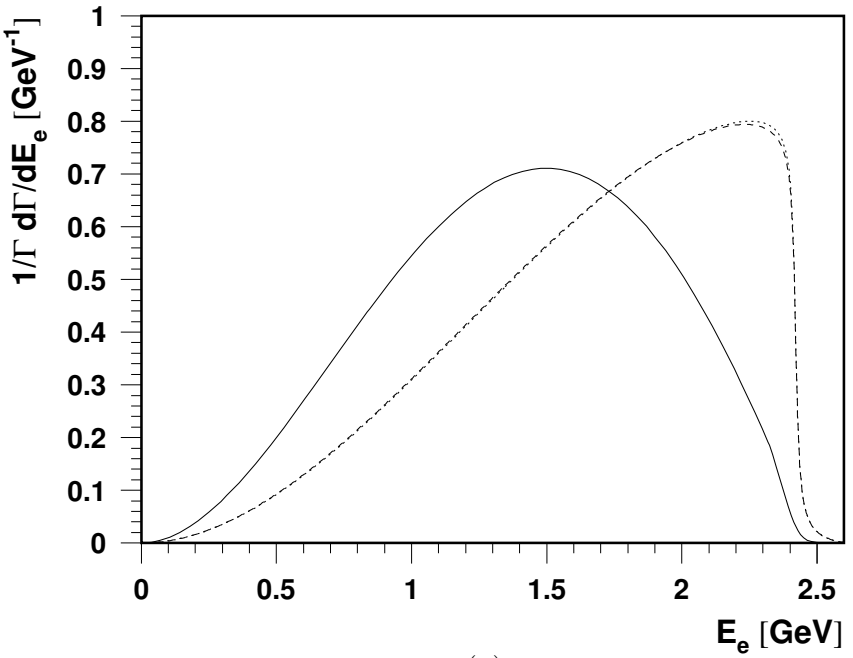


(a)

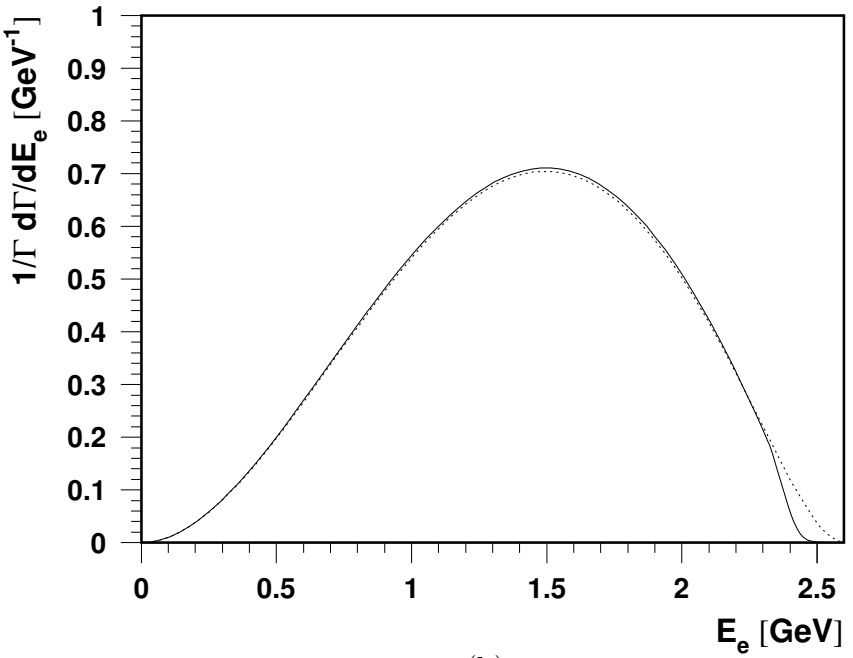


(b)

Figure 6.5: (a) The solid line is the electron energy spectrum from $B$-meson decay using $f_{jp}(x, \mu^2)$. The dotted line is the Born approximation of the spectrum. The dashed line is the spectrum with radiative corrections at $\alpha_s = 0.22$ using the naive parton model with the distribution function $f_{jp}(x)$. (b) The electron energy spectrum with different distribution function models. The solid line is the spectrum using $f_{jp}(x, \mu^2)$, and the dotted line the spectrum using $f_{ptr}(x, \mu^2)$.

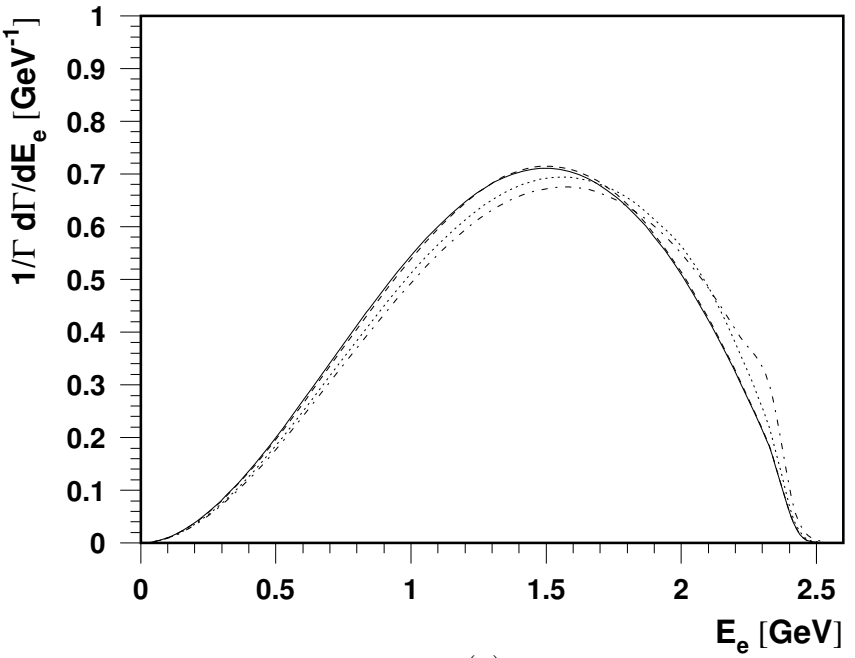


(a)

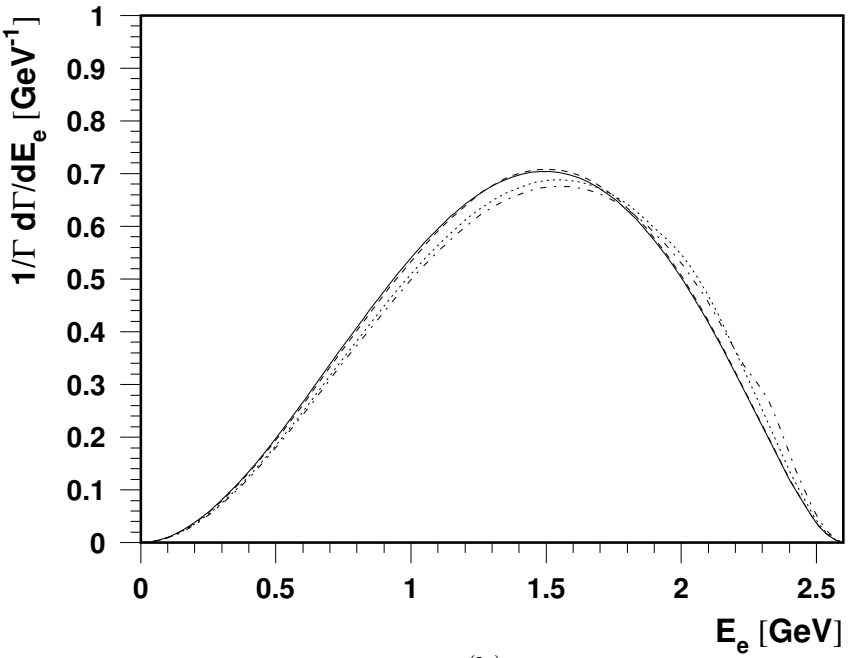


(b)

Figure 6.6: The electron energy spectrum with various evolution ranges. (a) The solid line is the electron energy spectrum, where evolution starts from $\mu^2 = x^2 M_B^2 - 1\ GeV^2$, which corresponds to $W^2 = 1\ GeV^2$. The dashed line has evolution range from $\mu^2 = x^2 M_B^2 - 5\ GeV^2$, the dotted line from $\mu^2 = x^2 M_B^2 - 15\ GeV^2$, and the dot–dashed line from $\mu^2 = x^2 M_B^2 - 20\ GeV^2$. $f_{jp}(x, \mu^2)$ is used for the distribution function. (b) The solid line is the electron energy spectrum, where evolution starts from $\mu^2 = x^2 M_B^2 - 1\ GeV^2$. The dashed line has evolution range from $\mu^2 = x^2 M_B^2 - 5\ GeV^2$, the dotted line from $\mu^2 = x^2 M_B^2 - 15\ GeV^2$, and the dot–dashed line from $\mu^2 = x^2 M_B^2 - 20\ GeV^2$. $f_{ptr}(x, \mu^2)$ is used for the distribution function.

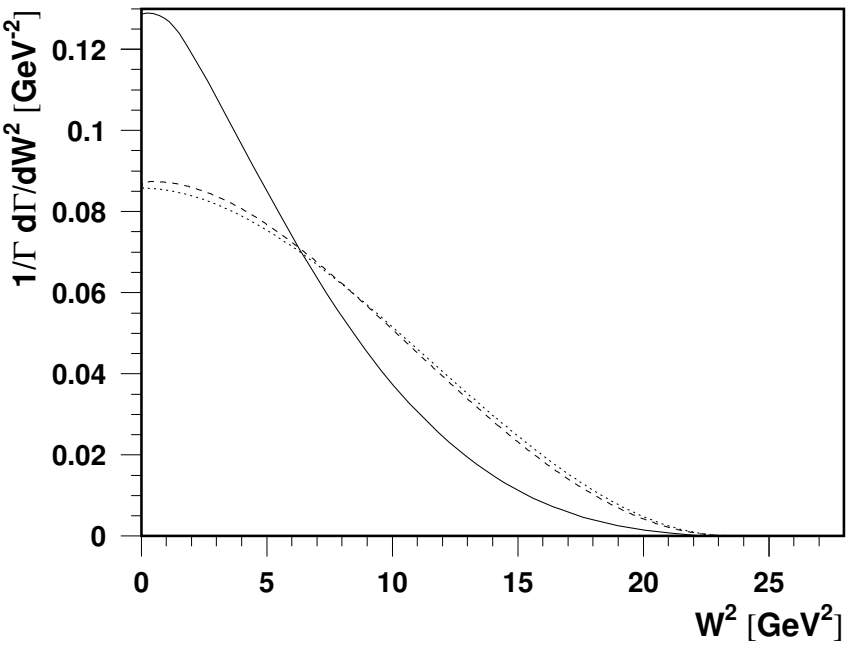


(a)

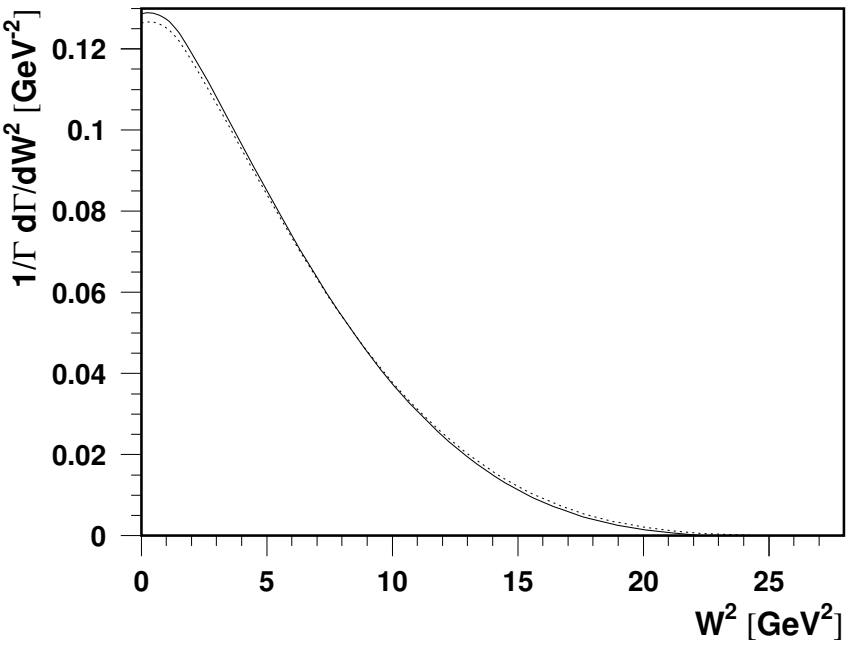


(b)

Figure 6.7: (a) The solid line is the leptonic invariant mass spectrum $W^2$ from $B$-meson decay using $f_{jp}(x, \mu^2)$. The dotted line is the Born approximation of the spectrum. The dashed line is the spectrum with radiative corrections at $\alpha_s = 0.22$ using the naive parton model with the distribution function $f_{jp}(x)$. (b) The leptonic invariant mass spectrum with different distribution function models. The solid line is the spectrum using $f_{jp}(x, \mu^2)$, and the dotted line the spectrum using $f_{ptr}(x, \mu^2)$.

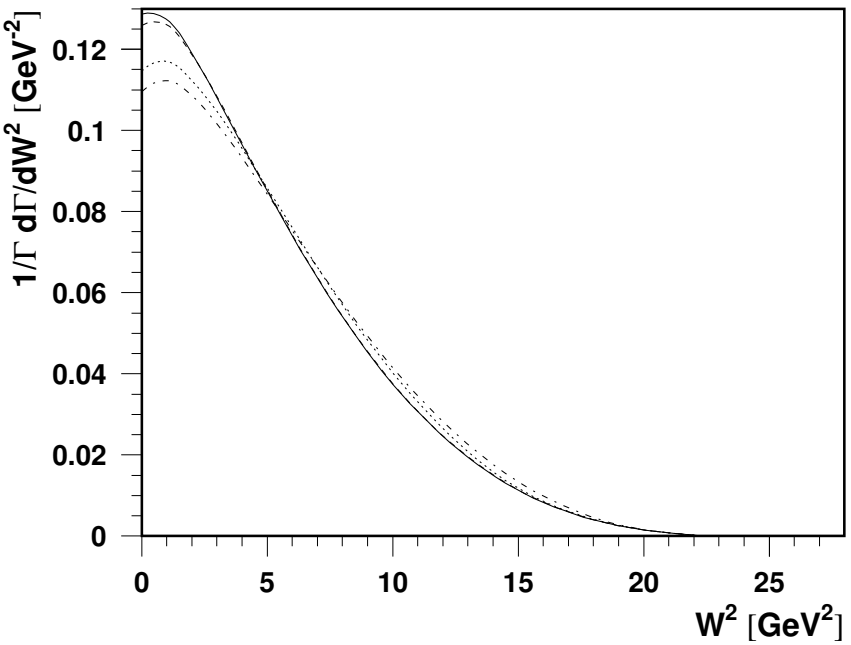


(a)

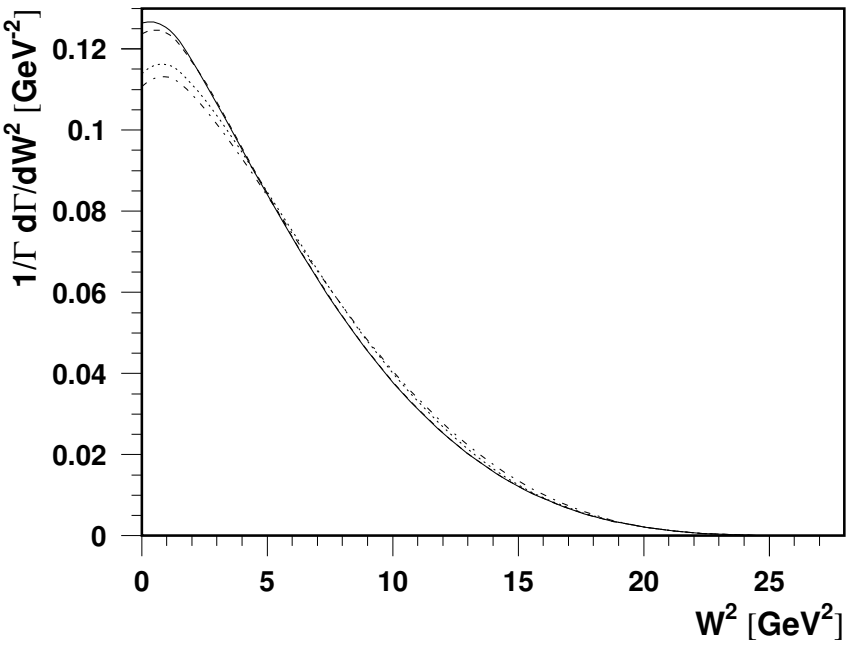


(b)

Figure 6.8: The leptonic invariant mass spectrum with various evolution ranges. (a) The solid line is the leptonic invariant mass spectrum, where evolution starts from $\mu^2 = x^2 M_B^2 - 1\ GeV^2$. The dashed line has evolution range from $\mu^2 = x^2 M_B^2 - 5\ GeV^2$, the dotted line from $\mu^2 = x^2 M_B^2 - 15\ GeV^2$, and the dot–dashed line from $\mu^2 = x^2 M_B^2 - 20\ GeV^2$. $f_{jp}(x, \mu^2)$ is used for the distribution function. (b) The solid line is the leptonic invariant mass spectrum, where evolution starts from $\mu^2 = x^2 M_B^2 - 1\ GeV^2$. The dashed line has evolution range from $\mu^2 = x^2 M_B^2 - 5\ GeV^2$, the dotted line from $\mu^2 = x^2 M_B^2 - 15\ GeV^2$, and the dot–dashed line from $\mu^2 = x^2 M_B^2 - 20\ GeV^2$. $f_{ptr}(x, \mu^2)$ is used for the distribution function.

# Chapter 7

# Conclusions

We showed the explicit calculation and analytical results of $QCD$ corrections to semi-leptonic $b$-quark decay in Chapter 3, using the dimensional regularizaiton scheme. The results are compared with those calculated with the finite gluon mass scheme and have been found to be identical.

We employed the parton model for the non–perturbative $QCD$ region, inspired by the fact that the current commutator between $B$-mesons can be expressed with a single distribution function in the Light–Cone limit. First, we adopted the naive parton–model without including further $QCD$ interactions of the quarks inside of $B$-mesons.

In Chapter 5 we compared the electron energy spectrum, the leptonic invariant mass spectrum, the hadronic energy spectrum, and the hadronic invariant mass spectrum from $B$-meson decay with those from $b$-quark decay, using the naive parton model for the non–perturbative $QCD$ region and observed a significant difference between the spectra. Especially, we could observe obvious differences in the electron energy spectrum and the hadronic invariant mass spectrum. The contribution from non–pertrubative $QCD$ is, therefore, significant and more study is needed for the non–perturbative $QCD$ region.

Further $QCD$ interactions inside the $B$-meson are considered by using Altarelli–Parisi evolution of the distribution function. We factorized the collinear divergences, which appeared in the limit of $m_b \to 0$, using the Leading Logarithmic Approximation, and drove the evolution equation for the distribution function, which was found out to be the same as the Altarelli–Parisi evolution equation. This evolution equation enables us to investigate $QCD$ in the low scale of $W^2$.

We compared the electron energy spectrum and the leptonic invariant mass spectrum with and without the evolution of the distribution function. The evolution of the distribution function clearly changes the electron energy spectrum and the leptonic invariant mass spectrum. We employed two different types of

distribution functions and observed that the change in the spectrum is less sensitive to the shape of the distribution function. In the case of the electron energy spectrum, we observed that the spectrum at the end point of the electron energy depends on the distribution function type. However, the spectrum gets a significant effect from the evolution range. Especially the leptonic invariant mass spectrum in the small $W^2$ region changes depending on the evolution range. From the observation of the change in the spectrum by the evolution of the distribution function, we conclude that the contribution of the further $QCD$ interactions inside the $B$-meson is not trivial and more theoretical and experimental research is needed for non–perturbative $QCD$.

# Appendix A

# Calculation of $\mathcal{I}_i$

The infrared and collinear singularities in the real gluon corrections appear as $\frac{1}{\varepsilon}$ and $\frac{1}{\varepsilon^2}$, and these poles are extracted by calculating $\mathcal{I}_i$ and expanding them with respect to $\varepsilon$.
The $\mathcal{I}_i$ are defined as

$$\mathcal{I}_i \equiv d\mathcal{R}_2^{(n)}(\, P;\, p_u,\, p_g\,)(\, p_b \cdot p_g\,)^i\,. \tag{A.1}$$

We employ the dimensional regularization scheme and therefore, keep the gluons massless and set the dimension $n = 4 + 2\varepsilon$ and $p_b^2 = m_b^2$ and $p_u^2 = 0$.

The phase space integration in general $n$-dimension is

$$\int d^n\,\vec{x} \equiv \int dr r^{n-1} \int_0^{2\pi} d\phi \int_0^{\pi} d\theta_1 \sin\theta_1 \cdots \int_0^{\pi} d\theta_{n-2} \sin^{n-2}\theta_{n-2}\,, \tag{A.2}$$

where $\vec{x} = (r, \phi, \theta_1, \cdots, \theta_2)$ in the $n$-dimensional spherical coordinate system and $|\vec{x}| \equiv r$. The scalar product $(p_b \cdot p_g)$ is dependent on the angle $\theta$ between the two vectors $\vec{p_b}$ and $\vec{p_g}$

$$(p_b \cdot p_g) = p_b^0 p_g^0 - |\vec{p_b}||\vec{p_g}| \cos\theta\,, \tag{A.3}$$

in the massless limit of $p_g$, and the angle $\theta$ is $\theta_{n-2}$ if one fixes one of the two vectors as the $x_n$-axis.

The energy-momentum conservation relation says

$$p_b = P + W\,, \tag{A.4}$$

where $P$ is the quark-gluon system $P = p_u + p_g$, and $W$ is the leptonic system

$W = p_e + p_\nu$. We calculate the $\mathcal{I}_i$ in the $P$ rest frame, i.e. $\vec{P} = 0$. The integrations over $\theta_i$, $i = 1 \cdots n-3$, on which the scalar product is independent, are carried out using the formula

$$\int_0^\pi d\vartheta \sin^m \vartheta = \sqrt{\pi}\, \frac{\Gamma[(m+1)/2]}{\Gamma[(m+2)/2]}\,, \tag{A.5}$$

and for the last angular phase integration we use the hyper-geometric formula

$${}_2F_1[a,\, b;\, c\,;\, \xi] = \frac{\Gamma[c]}{\Gamma[b]\Gamma[c-b]} \int_0^1 dx\, x^{b-1}(1-x)^{c-b-1}(1-x\xi)^{-a}\,. \tag{A.6}$$

The kinematic variables $z$ and $y$ are defined as

$$z \equiv \frac{P^2}{m_b^2}, \quad y \equiv \frac{W^2}{m_b^2}\,, \tag{A.7}$$

and some frequently appearing formula are defined as

$$\mathcal{P}_0(y,z) \equiv \frac{1-y+z}{2}\,, \tag{A.8}$$

$$\mathcal{P}_3(y,z) \equiv \frac{\lambda(1,y,z)}{2}\,, \tag{A.9}$$

where

$$\lambda(1,y,z) = \sqrt{1+y^2+z^2-2y-2z-2yz}\,, \tag{A.10}$$

and in the $P$ rest frame we obtain

$$Q^0 = \frac{m_b}{\sqrt{z}}\mathcal{P}_0(y,z)\,, \tag{A.11}$$

$$|\vec{Q}| = \frac{m_b}{\sqrt{z}}\mathcal{P}_3(y,z)\,, \tag{A.12}$$

$$P^2 = (P^0)^2 = m_b^2 z\,. \tag{A.13}$$

The collinear and infrared singularities appear as $z$ approaches 0. After integrating over the phase spaces and replacing $n$ with $4+2\varepsilon$, we obtain $\mathcal{I}_i$ expressed with Gamma functions and hyper-geometric functions. The hyper-geometric functions which are divergent when $z$ and $\varepsilon$ approach 0 should be analytically resolved and expressed with the hyper-geometric functions which are finite when $z$ and $\varepsilon$ go to 0.

The integration result for $\mathcal{I}_1$ is, for example,

$$\begin{aligned}\mathcal{I}_1 &= \frac{\pi^{1+\varepsilon}}{4}\,\frac{\Gamma[1+\varepsilon]}{\Gamma[2+2\varepsilon]}\,(P^0)^{1+2\varepsilon}(Q^0-|\vec{Q}|)\;\times \\ &\quad {}_2F_1\big[\,-1,\,1+\varepsilon;\,2+2\varepsilon;\,\frac{2|\vec{Q}|}{Q^0-|\vec{Q}|}\big]\,. \end{aligned} \tag{A.14}$$

The hyper-geometric function ${}_2F_1\left[-1\,,\,1+\varepsilon\,;\,2+2\varepsilon\,;\,\frac{2|\vec{Q}|}{Q^0-|\vec{Q}|}\right]$ is divergent when $\big(\frac{2|\vec{Q}|}{Q^0-|\vec{Q}|}\big)$ and $\varepsilon$ approach 0. Using the identities in Appendix B, we get

$$\begin{aligned}&{}_2F_1\big[\,-1,\,1+\varepsilon;\,2+2\varepsilon;\,\frac{2|\vec{Q}|}{Q^0-|\vec{Q}|}\big] = \\ &\quad\frac{1}{2}\left\{\big(\frac{Q^0+|\vec{Q}|}{Q^0-|\vec{Q}|}\big)\,{}_2F_1\big[\,0,\,2+\varepsilon;\,2+2\varepsilon;\,\frac{2|\vec{Q}|}{Q^0+|\vec{Q}|}\,\big]\right. \\ &\qquad\left. +\,{}_2F_1\big[\,0,\,1+\varepsilon;\,2+2\varepsilon;\,\frac{2|\vec{Q}|}{|\vec{Q}|-Q^0}\big]\right\}, \end{aligned} \tag{A.15}$$

and consequently,

$$\lim_{\varepsilon\to 0}\,{}_2F_1\big[\,-1,\,1+\varepsilon;\,2+2\varepsilon;\,\frac{2|\vec{Q}|}{|\vec{Q}|-Q^0}\,\big] = \frac{Q^0}{Q^0-|\vec{Q}|}\,. \tag{A.16}$$

After applying Eqs.(A.11) – (A.13), we obtain

$$\mathcal{I}_{\,1} = \frac{\pi^{1+\varepsilon}}{4}\,\frac{\Gamma[1+\varepsilon]}{\Gamma[2+2\varepsilon]}\,m_b^{2+2\varepsilon}\,\mathcal{P}_0(y,z)\,z^{\varepsilon}\,. \tag{A.17}$$

Other $\mathcal{I}_i$ can be calculated likewise and the results are

$$\mathcal{I}_{\,0} = \frac{\pi^{1+\varepsilon}}{2}\,m_b^{2\varepsilon}\,z^{\varepsilon}\,, \tag{A.18}$$

$$\begin{aligned}\mathcal{I}_{-1} &= \frac{\pi^{1+\varepsilon}}{2}\,m_b^{2\varepsilon-2}z^{\varepsilon}\,\frac{1}{\mathcal{P}_3(y,z)}\;\times \\ &\quad\left\{\frac{\Gamma[\varepsilon]}{\Gamma[1+2\varepsilon]}+\frac{\Gamma[-\varepsilon]\,z^{\varepsilon}}{(\mathcal{P}_0(y,z)+\mathcal{P}_3(y,z))^{2\varepsilon}}\right\}, \end{aligned} \tag{A.19}$$

$$\begin{aligned}\mathcal{I}_{-2} &= \pi^{1+\varepsilon}\,m_b^{2\varepsilon-4}\left\{\frac{\Gamma[\varepsilon-1]}{\Gamma[2\varepsilon]}\,\frac{z^{\varepsilon}}{\mathcal{P}_3(y,z)}\,\frac{1}{(\mathcal{P}_0(y,z)+\mathcal{P}_3(y,z))}\right. \\ &\qquad\left.+\,\Gamma[1-\varepsilon]\,\frac{z^{2\varepsilon-1}}{2^{2\varepsilon-1}}\,\frac{\mathcal{P}_0(y,z)}{\mathcal{P}_3(y,z)^{1+2\varepsilon}}\right\}. \end{aligned} \tag{A.20}$$

When these $\mathcal{I}_i$ are put into the ${}^i\mathcal{S}$, we obtain terms like $z^{\varepsilon-1}$ and $z^{2\varepsilon-1}$ and these terms are expanded in powers of $\varepsilon$ using the formula in [104]

$$(1-x)^{-1-\varepsilon} = \frac{1}{[1-x]_+} - \varepsilon \left[\frac{\ln(1-x)}{1-x}\right]_+ - \frac{1}{\varepsilon}\,\delta(1-x) + \mathcal{O}(\varepsilon^2)\,. \qquad \text{(A.21)}$$

The further explanation on the +-description is found in Appendix F.

The $\frac{1}{\varepsilon}$ and $\frac{1}{\varepsilon^2}$ singularities are obtained when the $\mathcal{I}_i$ are multiplied by $\frac{1}{z}$ except $\mathcal{I}_{-2}$. In the case of $\mathcal{I}_{-2}$ the singularities are obtained directly from $\mathcal{I}_{-2}$. After applying Eq.(A.21) into $\frac{\mathcal{I}_i}{z}$ and $\mathcal{I}_{-2}$ we obtain the explicit formula of $\frac{\mathcal{I}_i}{z}$ and $\mathcal{I}_{-2}$ and they read

$$\frac{\mathcal{I}_{\,1}}{z} = \frac{\pi\, m_b^2}{4}\,\mathcal{P}_0(y,z)\left[\frac{1}{\varepsilon}\delta(z) + \frac{1}{[\ z\ ]_+} + (\gamma_E - 2)\delta(z)\right], \qquad \text{(A.22)}$$

$$\frac{\mathcal{I}_{\,0}}{z} = \frac{\pi}{2}\left[\frac{1}{\varepsilon}\delta(z) + (\gamma_E - 2)\delta(z) + \frac{1}{[\ z\ ]_+}\right], \qquad \text{(A.23)}$$

$$\begin{aligned}\frac{\mathcal{I}_{-1}}{z} = {} & \frac{\pi}{4\, m_b^2}\,\frac{1}{\mathcal{P}_3(y,z)}\ \times \\ & \Bigg[\frac{1}{\varepsilon^2}\delta(z) + \frac{1}{\varepsilon}\delta(z)\big\{\gamma_E + 2\ln(\mathcal{P}_0(y,z)+\mathcal{P}_3(y,z))\big\} + \\ & \quad \delta(z)\big\{\frac{\gamma_E^2}{2} + 2\gamma_E \ln(\mathcal{P}_0(y,z)+\mathcal{P}_3(y,z)) \\ & \qquad -2\ln^2(\mathcal{P}_0(y,z)+\mathcal{P}_3(y,z)) - \frac{7}{12}\pi^2\big\} + \\ & \quad 4\frac{1}{[\ z\ ]_+}\ln(\mathcal{P}_0(y,z)+\mathcal{P}_3(y,z)) - 2\left[\frac{\ln(z)}{z}\right]_+\Bigg],\end{aligned} \qquad \text{(A.24)}$$

$$\begin{aligned}\mathcal{I}_{-2} = {} & \frac{\pi}{m_b^4}\,\frac{1}{\mathcal{P}_3(y,z)}\ \times \\ & \Bigg[-\frac{1}{\varepsilon}\delta(z)\left\{\mathcal{P}_0(y,z) - 2\mathcal{P}_3(y,z)\right\} + \\ & \quad \delta(z)\big\{\gamma_E(2\mathcal{P}_3(y,z) - \mathcal{P}_0(y,z)) + 2\mathcal{P}_3(y,z) \\ & \qquad -2\mathcal{P}_0(y,z) - \ln(\mathcal{P}_3(y,z))\mathcal{P}_0(y,z)\big\} + \\ & \quad 2\mathcal{P}_3(y,z)\frac{1}{[\ z\ ]_+}\Bigg].\end{aligned} \qquad \text{(A.25)}$$

After combining the results in Eqs.(A.22) – (A.25) we obtain the singular terms in the real gluon corrections. The singular terms with $\frac{1}{\varepsilon^2}$ are

$$\mathrm{Pole}[\,\varepsilon^{-2}\,] = \frac{1}{\varepsilon^2}\,(x_e - y)(1 - x_e + y)\delta(z)\,, \tag{A.26}$$

and the singular terms with $\frac{1}{\varepsilon}$ are

$$\begin{aligned}\mathrm{Pole}[\,\varepsilon^{-1}\,] \;=\; \frac{1}{\varepsilon}\,\frac{\delta(z)}{2}\Bigg(&\frac{1}{2}\big\{5x_e^2 - x_e(5+4y) + y(3+y)\big\} + \\ &(1 - x_e + y)(x_e - y)\ln(1-y) + \\ &\gamma_E(x_e - y)(1 - x_e + y)\Bigg)\,.\end{aligned} \tag{A.27}$$

These singular terms are canceled out by the singular terms from the virtual gluon corrections.

# Appendix B

# Hyper Geometric Function

The hyper geometric function ${}_2F_1[\,a\,,\,b\,;\,c\,;\,x\,]$ is defined as

$$ {}_2F_1[\,a\,,\,b\,;\,c\,;\,x\,] \equiv \frac{\Gamma(c)}{\Gamma(a)\Gamma(b)} \sum_{n=0}^{\infty} \frac{\Gamma(a+n)\Gamma(b+n)}{\Gamma(c+n)} \frac{x^n}{n!}\,, \tag{B.1} $$

and the integral form is

$$ {}_2F_1[\,a\,,\,b\,;\,c\,;\,x\,] = \frac{\Gamma(c)}{\Gamma(b)\Gamma(c-b)} \int_0^1 d\xi\, \xi^{b-1}(1-\xi)^{c-b-1}(1-\xi x)^{-a}\,. \tag{B.2} $$

Some identities of hyper geometric functions, which are frequently used, are presented below. For the calculation of $\mathcal{I}_i$ the identities below are helpful.

$$ \begin{aligned} (c-a)\,{}_2F_1[\,a-1\,,\,b\,;\,c\,;\,x\,] &= (c-a-b)\,{}_2F_1[\,a\,,\,b\,;\,c;\,x\,] \\ &\quad + b(1-x)\,{}_2F_1[\,a\,,\,b+1\,;\,c\,;\,x\,]\,, \end{aligned} \tag{B.3} $$

$$ \begin{aligned} {}_2F_1[\,a\,;\,b\,;\,c\,;\,x\,] &= (1-x)^{-a}\,\frac{\Gamma(c)\Gamma(b-a)}{\Gamma(b)\Gamma(c-a)}\,\times \\ &\quad {}_2F_1[\,a\,,\,c-b\,;\,a-b+1\,;\,\frac{1}{1-x}\,]\,+ \\ &\quad (1-x)^{-b}\,\frac{\Gamma(c)\Gamma(a-b)}{\Gamma(a)\Gamma(c-b)}\,\times \\ &\quad {}_2F_1[\,b\,,\,c-a\,;\,b-a+1\,;\,\frac{1}{1-x}\,]\,, \end{aligned} \tag{B.4} $$

$$c\ {}_2F_1[\,a\,,\,b\,;\,c\,;\,x\,] = (c-b)\ {}_2F_1[\,a\,,\,b\,;\,c+1\,;\,x\,] + b\ {}_2F_1[\,a\,,\,b+1\,;\,c+1\,;\,x\,]\,, \tag{B.5}$$

$$c\ {}_2F_1[\,a\,,\,b\,;\,c\,;\,x\,] = a\ (1-x)\ {}_2F_1[\,a+1\,,\,b+1\,;\,c+1\,;\,x\,] + (c-a)\ {}_2F_1[\,a\,,\,b+1\,;\,c+1\,;\,x\,]\,. \tag{B.6}$$

Some hyper geometric functions are expressed with other analytical functions like

$${}_2F_1[1,1;2;x] = -\frac{\ln(1-x)}{x}\,, \tag{B.7}$$

$${}_2F_1[1,2;3;x] = -2\,\frac{\ln(1-x)}{x^2} - \frac{2}{x}\,, \tag{B.8}$$

$${}_2F_1[1,1;3;x] = 2\,\frac{\ln(1-x)}{x} + 2\,\frac{\ln(1-x)}{x^2} + \frac{2}{x}\,. \tag{B.9}$$

# Appendix C

# Phase Space

The $1 \longrightarrow 4$ body decay formula in general $n$–dimension is expressed as

$$\begin{aligned} d\Gamma_4(\mathcal{A} \to a+b+c+d) = \\ & \frac{1}{2\mathcal{A}^0}\frac{d^{n-1}\vec{a}}{(2\pi)^{n-1}2a^0}\,\frac{d^{n-1}\vec{b}}{(2\pi)^{n-1}2b^0}\,\frac{d^{n-1}\vec{c}}{(2\pi)^{n-1}2c^0}\,\frac{d^{n-1}\vec{d}}{(2\pi)^{n-1}2d^0}\;\times \\ & (2\pi)^n\delta^{(n)}(\mathcal{A}-a-b-c-d)\overline{|\mathcal{M}|^2}\,. \end{aligned} \tag{C.1}$$

After an identity $\mathrm{I} = d^nP\delta^{(n)}(P-a-b)$ inserted, the formula is expressed as

$$\begin{aligned} d\Gamma_4(\mathcal{A} \to a+b+c+d) = \\ & \frac{1}{2\mathcal{A}^0}\frac{d^{n-1}\vec{c}}{(2\pi)^{n-1}2c^0}\,\frac{d^{n-1}\vec{d}}{(2\pi)^{n-1}2d^0}\,(2\pi)^n\delta^{(n)}(\mathcal{A}-P-c-d)\;\times \\ & \frac{d^{n-1}\vec{a}}{(2\pi)^{n-1}2a^0}\,\frac{d^{n-1}\vec{b}}{(2\pi)^{n-1}2b^0}\,\frac{d^{n-1}\vec{P}}{(2\pi)^{n-1}2P^0}\,(2\pi)^n\,\delta^{(n)}(P-a-b)\;\times \\ & \frac{1}{2\pi}\,\mathcal{A}^2dz\,\overline{|\mathcal{M}|^2}\,, \end{aligned} \tag{C.2}$$

where $z \equiv \frac{P^2}{\mathcal{A}^2}$. The formula in Eq.(C.2) can be written in a clearer form like

$$\begin{aligned} d\Gamma_4(\mathcal{A} \to a+b+c+d) = \\ & \frac{1}{2\mathcal{A}^0}\frac{d^{n-1}\vec{c}}{(2\pi)^{n-1}2c^0}\,\frac{d^{n-1}\vec{d}}{(2\pi)^{n-1}2d^0}\,\frac{d^{n-1}\vec{P}}{(2\pi)^{n-1}2P^0}\;\times \\ & (2\pi)^n\delta^{(n)}(\mathcal{A}-P-c-d)\;\times \\ & \frac{1}{(2\pi)^{n-1}}\mathcal{A}^2dz\,\frac{d^{n-1}\vec{a}}{2a^0}\,\frac{d^{n-1}\vec{b}}{2b^0}\,\delta^{(n)}(P-a-b)\,\overline{|\mathcal{M}|^2}\,. \end{aligned} \tag{C.3}$$

We define $d\mathcal{R}_m^{(n)}(P\,;\,q_1,q_2,\cdots,q_m)$ as

$$d\mathcal{R}_m^{(n)}(Q\,;\,q_1,q_2,\cdots,q_m) = \frac{d^{n-1}\vec{q}_1}{2\,q_1^0}\,\frac{d^{n-1}\vec{q}_2}{2\,q_2^0}\,\cdots\,\frac{d^{n-1}\vec{q}_m}{2\,q_n^0}\,\delta^{(n)}(Q-q_1-q_2-\,\cdots-q_m)\,. \tag{C.4}$$

Using the definition of $d\mathcal{R}_m^{(n)}(P\,;\,q_1,q_2,\cdots,q_m)$, We express Eq.(C.3) as

$$d\Gamma_4(\mathcal{A}\to a+b+c+d) = \frac{1}{2\mathcal{A}^0}\,\frac{1}{(2\pi)^{2n-3}}\,d\mathcal{R}_3^{(n)}(\mathcal{A};\,c,\,d,\,P)\,\times \frac{1}{(2\pi)^{n-1}}\,\mathcal{A}^2\,dz\,d\mathcal{R}_2^{(n)}(P;\,a,b)\,. \tag{C.5}$$

The $1\longrightarrow 3$ body decay formula has the general form like

$$d\Gamma_3(\mathcal{A}\to a+b+c) = \frac{1}{2\mathcal{A}^0}\,\frac{d^{n-1}\vec{a}}{(2\pi)^{n-1}2a^0}\,\frac{d^{n-1}\vec{b}}{(2\pi)^{n-1}2b^0}\,\frac{d^{n-1}\vec{c}}{(2\pi)^{n-1}2c^0}\,\times (2\pi)^n\delta^{(n)}(\mathcal{A}-a-b-c)\,\overline{|\mathcal{M}|^2}\,. \tag{C.6}$$

This $1\longrightarrow 3$ body decay formula can be expressed with a Lorentz invariant variable $z\equiv\frac{P^2}{\mathcal{A}^2}$ by inserting identities $\mathrm{I}=d^nP\,\delta^{(n)}(P-a-k)$ and $\mathrm{I}=d^nk\,\delta^{(n)}(k)$ and it reads

$$d\Gamma_3(\mathcal{A}\to a+b+c) = \frac{1}{2\mathcal{A}^0}\,\frac{1}{(2\pi)^{2n-3}}\,\frac{d^{n-1}\vec{b}}{2b^0}\,\frac{d^{n-1}\vec{c}}{2c^0}\,\frac{d^{n-1}\vec{P}}{2P^0}\,\times \delta^{(n)}(\mathcal{A}-P-b-c)\;\times dz\,\delta(z)\,\overline{|\mathcal{M}|^2}\,, \tag{C.7}$$

and using Eq.(C.4), we express Eq.(C.7) as

$$d\Gamma_3(\mathcal{A}\to a+b+c) = \frac{1}{2\mathcal{A}^0}\,\frac{1}{(2\pi)^{2n-3}}\,d\mathcal{R}_3^{(n)}(\mathcal{A};\,P,\,b,\,c)\,dz\,\delta(z)\,\overline{|\mathcal{M}|^2}\,. \tag{C.8}$$

# Appendix D

# $\gamma_5$ in $n$–dimension: Breitenlohner–Maison rules

The $\gamma_5$ is defined as $\gamma_5 = i\gamma^0\gamma^1\gamma^2\gamma^3$ in 4–dimension and satisfies the anti–commutation relation

$$\{\,\gamma^\mu,\,\gamma_5\,\} = 0\,, \tag{D.1}$$

and $\gamma_5^2 = 1$.
In 4 dimensions, it is given that $\mathrm{Tr}[\,\gamma_5\gamma^\mu\gamma^\nu\gamma^\alpha\gamma^\beta\,] = 4i\varepsilon^{\mu\nu\alpha\beta}$, where $\varepsilon^{\mu\nu\alpha\beta}$ is the anti–symmetric tensor. However, $\mathrm{Tr}[\gamma_5\gamma^\mu\gamma^\nu\gamma^\alpha\gamma^\beta]$ is not well defined in general $n$ dimensions, for we have more $\gamma$ matrices and cannot define the anti–symmetric tensor $\varepsilon^{\mu\,\nu\,\alpha\,\beta}$. The ill-definition of $\gamma_5$ in general $n$ dimensions raises ambiguous computational results.

The $\gamma$–Algebra in $n$ dimensions is well described in [101]. We have $n$ $\gamma^\mu$, $\mu = 0, \cdots, n-1$ matrices and $\gamma_5$. The $\gamma$ matrices verify the anti–commutation relations,

$$\{\,\gamma^\mu,\,\gamma^\nu\,\} = 2g^{\mu\nu}\,, \quad \gamma_5^2 = 1\,, \tag{D.2}$$

and the metric tensor $g^{\mu\nu} = g_{\mu\nu}$ has the property

$$\begin{aligned} g^{\mu\nu} &= 0\,, && \text{if } \mu \neq \nu\,, \\ g^{00} &= 1\,,\ g^{ii} = -1 && \text{for } i = 1, \cdots, n-1\,, \end{aligned} \tag{D.3}$$

and $g^{\mu\nu}g_{\mu\nu} = n$. Some useful relations derived from these properties are

$$\begin{aligned} \gamma^\mu\gamma_\mu &= n\,, \\ \gamma_\alpha\gamma^\mu\gamma^\alpha &= (2-n)\gamma^\mu\,, \\ \gamma^\alpha\gamma^\mu\gamma^\nu\gamma_\alpha &= 4g^{\mu\,\nu} + (n-4)\gamma^\mu\gamma^\nu\,, \\ \gamma^\alpha\gamma^\mu\gamma^\nu\gamma^\sigma\gamma_\alpha &= -2\,\gamma^\sigma\gamma^\nu\gamma^\mu + (4-n)\gamma^\mu\gamma^\nu\gamma^\sigma\,. \end{aligned} \tag{D.4}$$

Unlike in 4 dimensions, the anti–commutation relation of $\gamma_5$ cannot be used without any supposition in general $n$–dimension. For example, we consider $\mathrm{Tr}[\,\gamma_5\gamma^\alpha\gamma^\mu\gamma^\nu\gamma^\rho\gamma_\alpha\gamma^\sigma\,]$. If we allow $\{\,\gamma_\mu,\gamma_5\,\}=0$, we obtain two different results in $n$ dimensions.
After applying $\gamma^\alpha\gamma^\mu\gamma^\nu\gamma^\rho\gamma_\alpha = -2\,\gamma^\rho\gamma^\nu\gamma^\mu + (4-n)\gamma^\mu\gamma^\nu\gamma^\rho$, we obtain

$$\mathrm{Tr}[\gamma_5\gamma^\alpha\gamma^\mu\gamma^\nu\gamma^\rho\gamma_\alpha\gamma^\sigma] \;=\; (6-n)\mathrm{Tr}[\gamma_5\gamma^\mu\gamma^\nu\gamma^\rho\gamma^\sigma]\,, \tag{D.5}$$

but after letting $\gamma_5$ anti–commute with $\gamma^\alpha$, we get,

$$\mathrm{Tr}[\gamma_5\gamma^\alpha\gamma^\mu\gamma^\nu\gamma^\rho\gamma_\alpha\gamma^\sigma] \;=\; (n-2)\mathrm{Tr}[\gamma_5\gamma^\mu\gamma^\nu\gamma^\rho\gamma^\sigma]\,. \tag{D.6}$$

From Eq.(D.5) and Eq.(D.6), we obtain such a relation

$$(4-n)\,\mathrm{Tr}[\gamma_5\gamma^\mu\gamma^\nu\gamma^\rho\gamma^\sigma] = 0\,. \tag{D.7}$$

and it requests $\mathrm{Tr}[\gamma_5\gamma^\mu\gamma^\nu\gamma^\rho\gamma^\sigma] = 0$ in $n$-dimension, which is not acceptable. Therefore more careful attention should be paid when one handles $\gamma_5$ in $n$ dimensions.

A similar contradictory result is seen when we consider the trace

$$\mathrm{Tr}[\gamma_5\gamma_\alpha\gamma_{\mu_1}\gamma_{\mu_2}\gamma_{\mu_3}\gamma_{\mu_4}\gamma_{\mu_5}]\,. \tag{D.8}$$

After anti–commuting $\gamma_\alpha$ in Eq.(D.8) once around the trace, We obtain the identity as in [102, 103]

$$\varepsilon_{\mu_1\,\mu_2\,\mu_3\,\mu_4}\,g_{\mu_5\,\alpha} + cycl.(\mu_1\,\cdots\,\mu_5) = 0\,, \tag{D.9}$$

where the totally antisymmetric $\varepsilon$-tensor is introduced via

$$\mathrm{Tr}[\gamma_5\gamma_\alpha\gamma_\beta\gamma_\rho\gamma_\sigma] = 4i\varepsilon_{\alpha\,\beta\,\rho\,\sigma}\,. \tag{D.10}$$

After contraction Eq.(D.9) with $g^{\alpha\mu_5}$, we obtain

$$\left[\varepsilon_{\mu_1\,\mu_2\,\mu_3\,\mu_4}\,g_{\mu_5\,\alpha} + cycl.(\mu_1\,\cdots\,\mu_5)\right] g^{\alpha\mu_5} = (n-4)\varepsilon_{\mu_1\,\mu_2\,\mu_3\,\mu_4} = 0\,, \tag{D.11}$$

which is the same result in Eq.(D.7). This shows that anti–commutation relation $\{\gamma^\mu,\,\gamma_5\} = 0$ does not allow the analytical continuation of $\varepsilon_{\alpha\,\beta\,\rho\,\sigma}$ from 4 dimensions to a general $n$ dimensions, where $n \neq 4$.

There are several prescriptions on $\gamma_5$ to amend this problem. We use in this work the Breitenlohner–Maison scheme (BM–scheme) [59], which is worked consistently from the scheme suggested by 't Hooft and Veltman [57]. The works in [102, 103] are done in BM-scheme and provide explicit explanation. In BM–scheme, we separate an $n$–dimensional $\gamma$ matrix into its 4–dimensional part $\ddot{\gamma}$ and the remaining part $\dot{\gamma}$ and thus, $\gamma = \ddot{\gamma} + \dot{\gamma}$ . The postulations

$$\ddot{\gamma}_\mu\,\gamma_5 + \gamma_5\,\ddot{\gamma}_\mu \;=\; 0\,, \tag{D.12}$$

$$\dot{\gamma}_\mu\,\gamma_5 - \gamma_5\,\dot{\gamma}_\mu \;=\; 0\,, \tag{D.13}$$

drive a consistent $\gamma_5$ rules. Consider the trace $\mathrm{Tr}[\gamma_5\ddot{\gamma}_\alpha\gamma_{\mu_1}\gamma_{\mu_2}\gamma_{\mu_3}\gamma_{\mu_4}\gamma_{\mu_5}]$.
After letting $\ddot{\gamma}_\alpha$ anti–commute once around the trace using $\ddot{\gamma}_\mu\gamma_\nu + \gamma_\nu\ddot{\gamma}_\mu = 2\,\ddot{g}_{\mu\nu}$, where $\ddot{g}_{\mu\nu}$ is the 4–dimensional metric tensor with $\ddot{g}^{\mu\nu}\,\ddot{g}_{\mu\nu} = 4$,

$$\varepsilon_{\mu_1\mu_2\mu_3\mu_4}\,\ddot{g}_{\mu_5\alpha} + cycl.(\mu_1, \cdots, \mu_5) = 0\,, \tag{D.14}$$

which is called the Schouten identity. The contraction of Eq.(D.14) with $\ddot{g}^{\mu_5\alpha}$ is 0 and thus, does not request the contradictory condition $\varepsilon_{\alpha\beta\gamma\sigma} = 0$ in $n \neq 4$–dimension.

One proper representation of $\gamma_5$ to meet this request is [59]

$$\gamma_5 = \frac{i}{4!}\,\varepsilon_{\alpha\beta\gamma\sigma}\,\gamma^\alpha\gamma^\beta\gamma^\gamma\gamma^\sigma\,. \tag{D.15}$$

From the identity

$$\varepsilon_{\mu_1\mu_2\mu_3\mu_4}\varepsilon^{\nu_1\nu_2\nu_3\nu_4} = -\det(\ddot{g}_{\alpha\beta})\,, \quad \alpha = \mu_1, \cdots, \mu_4, \quad \beta = \nu_1, \cdots, \nu_4\,, \tag{D.16}$$

one can derive [102, 103]

$$\varepsilon_{\alpha\beta\gamma\sigma}\,\dot{g}^{\sigma\eta} = 0\,, \tag{D.17}$$

$$g^\beta_\alpha\,\ddot{g}_{\beta\sigma} = \ddot{g}_{\alpha\sigma}\,. \tag{D.18}$$

Therefore, $\varepsilon_{\alpha\beta\gamma\sigma}\,g^{\sigma\eta} = \varepsilon_{\alpha\beta\gamma\sigma}\,\ddot{g}^{\sigma\eta}$ and this shows that the $\varepsilon$–tensor projects out the 4–dimensional parts from any $n$–dimensional tensor.

# Appendix E

# Hadronic Tensor $h^{j}{}_{i}{}^{\mu\nu}$

The hadronic tensors $h^{j}{}_{i}{}^{\mu\nu}$ are defined with the redefined leptonic tensor $\ell^{\mu\nu} \equiv p_e^{\mu}\, p_{\nu}^{\nu}$ as

$$\mathcal{D}^{j}{}_{i} = h^{j}{}_{i}{}^{\mu\nu}\, \ell_{\mu\nu}\,. \tag{E.1}$$

The explicit forms of $h^{i}{}_{i}{}^{\mu\nu}$ read

$$h^{0}_{-2}{}^{\mu\nu} = m_b^2 \left( p_u^{\mu} p_g^{\nu} - p_u^{\mu} p_b^{\nu} \right), \tag{E.2}$$

$$\begin{aligned} h^{0}_{-1}{}^{\mu\nu} = \frac{1}{(p_u \cdot p_g)} \Big( & (p_b \cdot p_u) p_g^{\mu} p_b^{\nu} + 2 (p_b \cdot p_u) p_u^{\mu} p_b^{\nu} \\ & - (p_b \cdot p_u) p_u^{\mu} p_g^{\nu} - (p_u \cdot p_g) p_b^{\mu} p_g^{\nu} \\ & - (p_u \cdot p_g) p_u^{\mu} p_b^{\nu} + (p_u \cdot p_g) p_u^{\mu} p_g^{\nu} \Big), \end{aligned} \tag{E.3}$$

$$h^{0}_{0}{}^{\mu\nu} = p_g^{\mu} p_b^{\nu} + p_u^{\mu} p_b^{\nu} + p_u^{\mu} p_u^{\nu}\,, \tag{E.4}$$

$$h^{0}_{1}{}^{\mu\nu} = 0\,. \tag{E.5}$$

$$\begin{aligned} h^{1}_{-2}{}^{\mu\nu} = {} & m_b^2 \big( (p_u \cdot p_g) - (p_b \cdot p_u) \big) g^{\mu\nu} + 3 m_b^2 \big( p_u^{\mu} p_g^{\nu} - p_u^{\mu} p_b^{\nu} \big) \\ & + 3 m_b^2 \big( p_b^{\mu} p_u^{\nu} - p_g^{\mu} p_u^{\nu} \big)\,, \end{aligned} \tag{E.6}$$

$$
\begin{aligned}
h^{1}{}_{-1}{}^{\mu\nu} &= \big((p_u\cdot p_g) - 2(p_b\cdot p_u) - m_b^2\big)g^{\mu\nu} \;-\; p_g^\mu p_b^\nu - 3p_u^\mu p_b^\nu \\
&\quad +5p_u^\mu p_g^\nu \;-\; p_b^\mu p_g^\nu + 3p_b^\mu p_u^\nu - 3p_g^\mu p_u^\nu \\
&\quad + \frac{1}{(p_u\cdot p_g)}\Bigg(2(p_b\cdot p_u)^2 g^{\mu\nu} + 3(p_b\cdot p_u)p_g^\mu p_b^\nu \\
&\qquad\qquad + 6(p_b\cdot p_u)p_u^\mu p_b^\nu - 3(p_b\cdot p_u)p_u^\mu p_g^\nu \\
&\qquad\qquad - 3(p_b\cdot p_u)p_b^\mu p_g^\nu \;-\; 6(p_b\cdot p_u)p_b^\mu p_u^\nu \\
&\qquad\qquad + 2(p_b\cdot p_u)p_g^\mu p_g^\nu \;+\; 3(p_b\cdot p_u)p_g^\mu p_u^\nu\Bigg)\,, \qquad \text{(E.7)}
\end{aligned}
$$

$$
\begin{aligned}
h^{1}{}_{0}{}^{\mu\nu} &= \frac{1}{(p_u\cdot p_g)}\Bigg(2(p_b\cdot p_u)g^{\mu\nu} \;+\; 5p_g^\mu p_b^\nu \;+\; 3p_u^\mu p_b^\nu \;-\; p_b^\nu p_g^\nu \\
&\qquad\qquad - p_u^\mu p_g^\nu \;-\; 3p_b^\mu p_u^\nu \;-\; p_g^\mu p_u^\nu\Bigg)\,, \qquad \text{(E.8)}
\end{aligned}
$$

$$
h^{1}{}_{1}{}^{\mu\nu} = \frac{1}{(p_u\cdot p_g)}\,g^{\mu\nu}\,, \qquad \text{(E.9)}
$$

$$
h^{2}{}_{-2}{}^{\mu\nu} = 2m_b^2\big(p_u^\mu p_g^\nu \;-\; p_u^\mu p_b^\nu \;+\; p_b^\mu p_u^\nu \;-\; p_g^\mu p_u^\nu\big)\,, \qquad \text{(E.10)}
$$

$$
\begin{aligned}
h^{2}{}_{-1}{}^{\mu\nu} &= \frac{1}{(p_u\cdot p_g)}\Bigg((p_u\cdot p_g)^2 g^{\mu\nu} \;+\; 5(p_u\cdot p_g)p_u^\mu p_g^\nu \;-\; 5(p_u\cdot p_g)p_g^\mu p_u^\nu \\
&\qquad\qquad - 2(p_b\cdot p_u)p_u^\mu p_g^\nu \;+\; 2(p_b\cdot p_u)p_g^\mu p_u^\nu \\
&\qquad\qquad + \big(2(p_b\cdot p_u) \;-\; (p_u\cdot p_g)\big)\big(p_g^\mu p_b^\nu \;+\; 2p_u^\mu p_b^\nu\big) \\
&\qquad\qquad - \big(2(p_b\cdot p_u) \;-\; (p_u\cdot p_g)\big)\big(p_b^\mu p_g^\nu \;+\; p_b^\mu p_u^\nu\big)\Bigg)\,, \qquad \text{(E.11)}
\end{aligned}
$$

$$
\begin{aligned}
h^{2}{}_{0}{}^{\mu\nu} &= \frac{1}{(p_u\cdot p_g)}\Bigg(5p_g^\mu p_b^\nu \;+\; 2p_u^\mu p_b^\nu \;-\; p_u^\mu p_g^\nu \;-\; 2(p_u\cdot p_g)g^{\mu\nu} \\
&\qquad\qquad + p_g^\mu p_u^\nu \;-\; 5p_b^\mu p_g^\nu \;-\; 2p_b^\mu p_u^\nu\Bigg)\,, \qquad \text{(E.12)}
\end{aligned}
$$

$$
h^{2}{}_{1}{}^{\mu\nu} = \frac{1}{(p_u\cdot p_g)}\,g^{\mu\nu}\,. \qquad \text{(E.13)}
$$

# Appendix F

# +-description $[f(x)]_+$

The +-description of a function $f(x)$, which is singular at $x = 1$, is expressed by $[f(x)]_+$ and the definition of $[f(x)]_+$ is

$$\int_0^1 dx\, g(x)\, [f(x)]_+ = \int_0^1 dx\, f(x)\, [g(x) - g(1)]\,, \tag{F.1}$$

and consequently,

$$\int_0^1 dx\, [f(x)]_+ = 0\,. \tag{F.2}$$

For examples of $[f(x)]_+$, we can take

$$\frac{1}{[1-x]_+} \quad \text{and} \quad \Big[\frac{\ln(1-x)}{1-x}\Big]_+, \tag{F.3}$$

and according to Eq.(F.1),

$$\int_0^1 dx\, \frac{1}{[1-x]_+}\, g(x) \;=\; \int_0^1 dx\, \frac{[\, g(x) - g(1)\,]}{1-x}\,, \tag{F.4}$$

$$\int_0^1 dx\, \Big[\frac{\ln(1-x)}{1-x}\Big]_+ g(x) \;=\; \int_0^1 dx\, \frac{\ln(1-x)}{1-x}\, [\, g(x) - g(1)\,]\,. \tag{F.5}$$

We write the analytic form of the +-description as

$$[f(x)]_+ = \lim_{\beta\to 0}\left[\int_0^1 dx\, f(x)\,\theta(1\,-\,\beta)\,+\,\delta(1\,-\,x\,-\,\beta)\int_0^\beta dy\, f(y)\right]. \quad \text{(F.6)}$$

The +-description which appear during the calculation of the real gluon corrections are

$$\frac{1}{[\ x\ ]_+} \quad \text{and} \quad \left[\frac{\ln(x)}{x}\right]_+, \quad \text{(F.7)}$$

which have singularities at $x = 0$. After some manipulation of Eq.(F.1) and Eq.(F.6) we obtain

$$\int_0^1 dx\, g(x)\,\frac{1}{[\ x\ ]_+} = \int_0^1 dx\,\frac{[g(x)-g(0)]}{x}\,, \quad \text{(F.8)}$$

and

$$\int_0^1 dx\, g(x)\left[\frac{\ln(x)}{x}\right]_+ = \int_0^1 dx\,[g(x)\,-\,g(0)]\,\frac{\ln(x)}{x}\,. \quad \text{(F.9)}$$

Sometimes, we encounter the integration range which is not from 0 to 1 but from an arbitrary $A < 1$ to 1. We introduce a more general +-description $[f(x)]_A$ and it satisfies

$$\int_A^1 dx\,[f(x)]_A\, g(x) = \int_A^1 dx\, f(x)\,\{g(x)-g(1)\}\,, \quad \text{(F.10)}$$

and

$$\int_A^1 dx\,[f(x)]_A = 0\,. \quad \text{(F.11)}$$

Now we need to find out the relation between $[f(x)]_+$ and $[f(x)]_A$. Setting

$$[f(x)]_+ = [f(x)]_A + \mathcal{C}\,\delta(1-x)\,, \quad \text{(F.12)}$$

and keeping the principle integration formula Eq.(F.1), we can find out the relevant $\mathcal{C}$. After some calculation we obtain a general formula for the coefficient $\mathcal{C}$ for a $[f(x)]_A$

$$\mathcal{C} = -\int_0^A dy\, f(y)\,. \tag{F.13}$$

For special examples, we consider

$$\frac{1}{[1-x]_A} \quad \text{and} \quad \Big[\frac{\ln(1-x)}{1-x}\Big]_A\,. \tag{F.14}$$

Applying Eq.(F.12) and Eq.(F.13) or calculating the coefficient $\mathcal{C}$ directly keeping the principle integration Eq.(F.1), we obtain the following formula which is the same as in [104]

$$\frac{1}{[1-x]_+} = \frac{1}{[1-x]_A} + \ln(1-A)\,\delta(1-x)\,, \tag{F.15}$$

$$\Big[\frac{\ln(1-x)}{1-x}\Big]_+ = \Big[\frac{\ln(1-x)}{1-x}\Big]_A + \frac{1}{2}\,\ln^2(1-A)\,\delta(1-x)\,. \tag{F.16}$$

# Bibliography


[1] T. Gottschalk, *Phys. Rev.* D**23**, 56 (1981).

[2] B. Guberina, R.D. Peccei, and R. Rückl, *Nucl. Phys.* B**171**, 333 (1980).

[3] M. Jeżabek and J.H. Kühn, *Nucl. Phys.* B**320**, 20 (1989).

[4] F. De Fazio and M. Neubert, *JHEP* **9906**, 017 (1999).

[5] A. Ali and E. Pietarinen, *Nucl. Phys.* B**154**, 519 (1979).

[6] N. Cabibbo, G. Corbo, and L. Maiani, *Nucl. Phys.* B**155**, 93 (1979).

[7] G. Altarelli, N. Cabbibo, G. Corbo, L. Maiani, and G. Martinelli, *Nucl. Phys.* B**208**, 365 (1982).

[8] G. Corbo, *Nucl. Phys.* B**212**, 99 (1983).

[9] M. Gremm and I. Stewart, *Phys. Rev.* D**55**, 1226 (1997).

[10] A. Czarnecki and K. Melnikov, *Phys. Rev. Lett.* **88**, 131801 (2002).

[11] Jik Lee and Ian Shipsey, hep-ex/0203015.

[12] M. Neubert, *Phys. Rev.* D**49**, 4623 (1994).

[13] M. Neubert, *Phys. Report* **245**, 259 (1994).

[14] C.W. Bauer, M. Luke, and T. Mannel, hep-ph/0102089.

[15] A.K. Leibovich and I.Z. Rothstein, *Phys. Rev.* D**61**, 074006 (2000).

[16] A.K. Leibovich, I. Low, and I.Z. Rothstein, *Phys. Lett.* B**513**, 83 (2001).

[17] M. Neubert, *Phys. Lett.* B**513**, 88 (2001).

[18] H. Albrecht *et al.*, Argus Collaboration, *Phys. Lett.* B**255**, 297 (1991).

[19] C.W. Bauer, Z. Ligeti, and M.E. Luke, *Phys. Lett.* B**479**, 395 (2000); C.W. Bauer, Z. Ligeti, and M.E. Luke, hep-ph/0007054.

[20] C.W. Bauer, Z. Ligeti, and M.E. Luke, *Phys. Rev.* D**64**, 113004 (2001).

[21] C. Greub and S.J. Rey, *Phys. Rev.* D**56**, 4250 (1997).

[22] V.D. Barger, C.S. Kim, and R.J.N. Phillips, *Phys. Lett.* B**251**, 629 (1990).

[23] A.F. Falk, Z. Ligeti, and M.B. Wise, *Phys. Lett.* B**406**, 225 (1997).

[24] R.D. Dikeman and N.G. Uraltsev, *Nucl. Phys.* B**509**, 378 (1998).

[25] I. Bigi, R.D. Dikeman, and N.G. Uraltsev, *Eur. Phys. J.* C**4**, 453 (1998).

[26] K.K. Jeong, C.S. Kim, and Yeong Gyun Kim, *Phys. Rev.* D**63**, 014005 (2001).

[27] K. Hagiwara *et al*, *Phys. Rev.* D**66**, 010001 (2002).

[28] I. Shipsey, hep-ex/0207091.

[29] Aida X. El-Khadra *et al.*, hep–ph/0101023.

[30] A. Bareiss and E.A. Paschos, *Nucl. Phys.* B**327**, 353 (1989).

[31] A. Bareiss, *Z. Phys.* C**53**, 311 (1992).

[32] C.H. Jin, W.F. Palmer, and E.A. Paschos, *Phys. Lett.* B**329**, 364 (1994).

[33] C.H. Jin and E.A. Paschos, *Eur.Phys.J.* C**1**, 523 (1998).

[34] C.S. Kim, Yeong Gyun Kim, and Kang Young Lee, *Phys. Rev.* D**57**, 4002 (1998).

[35] A.V. Manohar and M.B. Wise, *Phys. Rev.* D**49**, 1310 (1994).

[36] T. Mannel, *Nucl. Phys.* B**413**, 396 (1994).

[37] N. Uraltsev, *Int. J. Mod. Phys.* A**14**, 4641 (1999).

[38] A.H. Hoang, Z. Ligeti and A.V. Manohar, *Phys. Rev.* D**59**, 074017 (1999).

[39] A.H. Hoang, Z. Ligeti and A.V. Manohar, *Phys. Rev. Lett.* **82**, 277 (1999).

[40] D.E. Groom *et al.*, *Eur. Phys. J.* C**15**, 1 (2000).

[41] ALEPH Collaboration, CDF Collaboration, DELPHI Collaboration, L3 Collaboration, OPAL Collaboration and SLD Collaborations, D. Abbaneo *et al.*, *Combined results on B hadron production rates, lifetimes, oscillations and semi-leptonic decays*, SLAC-PUB-8492, CERN-EP-2000-096 (2000).

[42] G. Abbiendi *et al.*, OPAL Collaboration, *Eur. Phys. J.* C**21**, 399 (2001).

[43] CLEO, J. Bartelt *et al.*, *Phys. Rev. Lett.* **71**, 4111 (1993).

[44] J.P. Alexander *et al.*, *Phys. Rev. Lett.* **77**, 5000 (1996).

[45] B.H. Behrens *et al.*, *Phys. Rev.* D**61**, 052001 (2000).

[46] P.F. Harrison and H.R. Quinn, Editors, *The BABAR Physics Book*, SLAC Report 504, (1998).

[47] *BABAR* Collaboration, B. Aubert *et al.*, *Nucl. Instrum. Meth.* A**479**, 1 (2002).

[48] KEKB B Factory Design Report, KEK Report 95-7, (1995).

[49] Y. Funakoshi *et al.*, *Proc. 2000 European Particle Accelerator Conference*, Vienna (2000).

[50] B.A. Shwartz and Belle Collaboration, *Nucl. Phys. Proc. Suppl.* **93**, 332 (2001).

[51] S. Mori *et al*, *Nucl. Instrum. Meth.* A**479**, 117 (2002).

[52] S.W. Herb *et al.*, *Phys. Rev. Lett.* **39**, 252 (1977).

[53] F. Abe *et al.* (CDF Collaboration), *The CDF detector: An overview*, *Nucl. Instr. and Meth.*, A**271**, 387 (1988).

[54] Y. Karyotakis, *talk at ICHEP02*, http://www.ichep02.nl.

[55] M. Yamauchi, *talk at ICHEP02*, http://www.ichep02.nl.

[56] W. Pauli and F. Villars, *Rev. mod. Phys.* **21**, 434 (1949).

[57] G. 't Hooft and M. Veltman, *Nucl. Phys.* B**44** 189 (1972).

[58] M. Chanowitz, M. Furman, and I. Hinchliffe, *Nucl. Phys.* B**159** 225 (1979).

[59] P. Breitenlohner and D. Maison, *Commu. Math. Phys.* **52** 11 (1977).

[60] G.P. Lepage, CLNS-80/447 (1980).

[61] M. Luke, *Phys. Lett.* B**252**, 447 (1990).

[62] A.F. Falk and M. Neubert, *Phys. Rev.* D**47**, 2965 (1993).

[63] A.F. Falk, M. Luke, and M. Savage,*Phys. Rev.* D**53**, 2491 (1996).

[64] R.P. Feynman, *Photon-hadron interactions*, Benjamin, New York (1972).

[65] J.D. Bjorken and E.A. Paschos, *Phys. Rev.* **185**, 1975 (1969).

[66] T.P. Cheng and L.F. Li, *Gauge theory of elementary particle physics*, Oxford (1984).

[67] C. Jin, *Phys. Rev.* D**56**, 7267 (1997).

[68] C. Jin, *Phys. Rev.* D**57**, 6851 (1998).

[69] C. Jin, *Eur. Phys. J.* c**11**, 335 (1999).

[70] J. Chay, H. Georgi, and B. Grinstein, *Phys. Lett.* B**247**, 399 (1990).

[71] I.I. Bigi, N.G. Uraltsev, and A.I. Vainshtein, *Phys. Lett.* B**293**, 430 (1992); *Errt. ibid.* B**297**, 477 (1993).

[72] I.I. Bigi, M.A. Shifman, N.G. Uraltsev, and A.I. Vainshtein, *Phys. Rev. Lett.* **71**, 496 (1993).

[73] I.I. Bigi, M.A. Shifman, N.G. Uraltsev, and A.I. Vainshtein, *Int. J. Mod. Phys.* A**9**, 2467 (1994).

[74] B. Blok, L. Koyrakh, M.A. Shifman, and A.I. Vainshtein, *Phys. Rev.* D**49**, 3356 (1994); *Errt. ibid.* B**50**, 3572 (1994).

[75] A.F. Falk, M. Luke, and M.J. Savage, *Phys. Rev.* D**49**, 3367 (1994).

[76] A.F. Falk, Z. Ligeti, M. Neubert, and Y. Nir, *Phys. Lett.* B**326**, 145 (1994).

[77] M. Luke and M.J. Savage, *Phys. Lett.* B**321**, 88 (1994).

[78] C. Peterson, D. Schlatter, J. Schmitt and P.M. Zerwas, *Phys. Rev.* D**27**, 105 (1983).

[79] CLEO Collaboration (R.A. Briere *et al.*). CLEO–CONF–02–10, Jul 2002, hep–ex/0209024.

[80] J.H. Kühn and M. Steinhauser, *Nucl. Phys.* B**619**, 588 (2001); *Erratum-ibid* B**640**, 415 (2002).

[81] J.H. Kühn, A.A. Penin, and A.A. Pivovarov, *Nucl. Phys.* B**534**, 356 (1998).

[82] A.A. Penin and A.A. Pivovarov, *Phys. Lett.* B**435**, 413 (1998).

[83] A.A. Penin and A.A. Pivovarov, *Nucl. Phys.* B**549**, 217 (1999).

[84] A.A. Penin and M. Steinhauser, *Phys. Lett.* B**538**, 335 (2002).

[85] K. Melnikov and A. Yelkhovsky, *Phys. Rev.* D**59**, 114009 (1999).

[86] M. Beneke and A. Signer, *Phys. Lett.* B**471**, 233 (1999).

[87] A.H. Hoang, hep-ph/0008102.

[88] A. Pineda, *JHEP* **0106**, 022 (2001).

[89] N. Gray, D.J. Broadhurst, W. Grafe, and K. Schilcher, *Z. Phys.* C**48**, 673 (1990).

[90] K.G. Chetyrkin and M. Steinhauser, *Phys. Rev. Lett.* **83**, 4001 (1999).

[91] K.G. Chetyrkin and M. Steinhauser, *Nucl. Phys.* B**573**, 617 (2000).

[92] K. Melnikov and T. van Ritbergen, *Phys. Lett.* B**482**, 99 (2000).

[93] R.P. Feynman, *Phys. Rev. Lett.* **23**, 1415 (1969).

[94] G. Altarelli and G. Parisi, *Nucl. Phys.* B**126**, 298 (1977).

[95] G. Altarelli, *Phys. Report* **81**, No.1, 1 (1982).

[96] H. Georgi and H.D. Politzer, *Phys. Rev.* D**9**, 416 (1974).

[97] D.J. Gross and F. Wilczek, *Phys. Rev* D**9**, 980 (1974).

[98] K.Y. Lee and J.K. Kim, *Phys. Lett.* B**377**, 153 (1996).

[99] J. Binnewies, B.A. Kniehl, and G. Kramer, *Z. Phys.* C**76**, 677 (1997).

[100] K.Y. Lee and S. Baek, hep-ph/9809316.

[101] F.J. Ynduràin, *The Theory of Quark and Gluon Interactions*, Springer-Verlag, New York (1993).

[102] J.G. Körner, G. Schuler, G. Kramer, and B. Lampe, *Phys. Lett.* B**164** 136 (1985).

[103] J.G. Körner, G. Schuler, G. Kramer, and B. Lampe, *Z. Phys.* C**32** 181 (1986).

[104] R.K. Ellis, M.A. Furman, H.E. Haber, and I. Hinchliffe, *Nucl. Phys.* B**173**, 397 (1980).

# Acknowledgment

First, I would like to express my gratefulness to Prof. G. Kramer for his instruction and supervision. Through the collaboration with him, I have learned a lot. Whenever I had questions, he always made effort to make me understood. Apart from physics, I enjoyed his stories about Physics, German culture, and Germany during lunch times. More over, I respect his attitude as a scholar.

I thank Prof. B.A. Kniehl for reading the manuscript carefully and advising my work. His enthusiastic attitude toward Physics is enough to persuade to work hard. From time to time, he suggested colloquiums held at the university, and they were very interesting and informative.

I appreciate DAAD for the financial support and the kindness to help the scholarship students. DAAD gave me an opportunity to learn about Germany, and to come to know Germany and to get familiar with different cultures were a nice experience in my life.

I would also like to thank many people from whom I have learned and been helped during my doctoral work. I thank Dr. S. Nam for his kind information and explanation about the experiments and Dr. Jik Lee for providing Figures in Chapter 1. Dr. S. Baek, Dr. S. Dittmaier, Dr. A. Brandenburg, Dr. k. Golec–Biernat, and Dr. M. Klasen gave me advice for my work and I am very grateful to them.

I cannot miss the colleagues with whom I shared good times. I thank Ezequiel, Luigi, Stephan, David de Costa, David Rainwater, Nabil, and Huitzu, who are willing to discuss with me over Physics and outside Physics also. Especially, I thank Nabil for helping me to work with Fortran and David Rainwater for reading my manuscript and correcting my English. I also thank all other people who are not listed here and from whom I got help during my doctoral work.

Most of all, I am very grateful to my parents for supporting me mentally and financially. Whenever I felt uneasy, their advice and encouragement refreshed me. My sister and brothers have always been a big help and I thank them. I would like to close my acknowledgment by expressing my gratitude to my super particle Dominik Donald Duck for encouraging me when I tried to quit and advising me for writing my dissertation.